

1 A scaling law of periodic radial geometry organises 2 eukaryotic chromosomes

3 Wolf Henning Gebhardt^{1,*}

4 ¹Independent Researcher, Bad Homburg, Germany

5 *Correspondence: w.gebhardt@protonmail.com

6 Chromatin alternates between active (A) and inactive (B) compartments along every eukaryotic chromosome¹⁻⁴,
7 but whether this alternation itself carries a higher-order spatial organisation has not been examined. Here we
8 identify a conserved periodic supra-compartment fold, with a wavelength approximately four times the mean
9 A/B compartment domain-pair period (so that one supra-compartment cycle spans roughly four A/B pairs
10 along the chromosome), by applying a continuous wavelet transform to the coordinate-free sequence of consec-
11 utive chromatin accessibility peaks in human, mouse, chicken and *Drosophila* chromosomes. Three signatures
12 separate this fold from compartment identity. First, its wavelength scales geometrically with chromosome length
13 as $T \propto L^{0.83}$ across 71 chromosomes in four phyla, whereas compartment domain sizes do not; cross-cell-type
14 validation across 74 ENCODE human cell types spanning pluripotent, immune, neural, epithelial, and can-
15 cer lineages confirms universality (74/74 with 95% CI overlapping [0.52, 1.14]; pooled $\hat{b} = 0.91$ [0.83, 0.98]).
16 Second, wavelet phase predicts radial nuclear position between speckles and lamina by TSA-seq in K562 cells
17 ($R^2 = 0.90$)¹²⁻¹⁴, realising a three-dimensional radial-accordion fold confirmed in 14/14 GM12878 single-cell
18 Dip-C structures, reproduced by orthogonal seqFISH+ in mouse embryonic stem cells¹⁷, and preserved at
19 single-cell resolution in 240/240 mouse cortical neurons and 16/16 human lymphoblastoid cells^{15,16}. Third,
20 mitotic compartment dissolution in the DT40 CDK1-as time course³³ collapses the signal ~ 426 -fold, and RIF1
21 loss abolishes interchromosomal coherence without shifting the wavelength¹⁸, evidence that the fold is both
22 compartment-coupled and protein-maintained. Strong enhancers (H3K27ac) preferentially cluster at speckle-
23 proximal wave crests (3.96-fold OR), placing the wave on the same spatial coordinate as transcription factors,
24 mutations, and translocation breakpoints. Chromosomes of unequal size therefore achieve proportional access
25 to nuclear environments through a conserved geometric scaling law: each chromosome traces approximately
26 five radial excursions between speckles and lamina, regardless of length. The scaling law operates self-similarly
27 across at least two orders of magnitude in length, with the same exponent organising sub-domain wavelengths
28 within individual compartments as it does wavelengths across chromosomes (within-compartment $\hat{b} = 0.77$ [0.63,
29 0.91]; 95% CI overlaps the cross-chromosome value; Supplementary Fig. 38).

30 The three-dimensional organisation of the eukaryotic nucleus is well-characterised at the scales of loops,
 31 topologically associating domains (TADs), and A/B compartments^{1–4}. Compartment identity correlates with
 32 radial nuclear position: A-compartment domains face nuclear speckles, whereas B-compartment domains as-
 33 sociate with the lamina and the nucleolus^{12–14}. Here we describe a structural level above compartments: a
 34 conserved periodic radial fold spanning multiple compartment domains (Extended Data Fig. 1) that has not
 35 been measurable because standard coordinate-based analyses of Hi-C or accessibility tracks are dominated by
 36 the autocorrelation of the compartment alternation itself, which blurs any supra-compartment structure into
 37 the low-frequency continuum of the spectrum. Prior wavelet approaches have been applied to genomic-sequence
 38 periodicity^{5,6,8,9} and to hierarchical Hi-C architecture¹⁰, but not to compartment alternation at scales above the
 39 compartment itself. We therefore transform the problem: instead of analysing compartment identity on genomic
 40 coordinates, we apply a continuous wavelet transform (CWT, complex Paul $m = 2$) to the *consecutive* sequence
 41 of chromatin accessibility peaks ordered by chromosomal position with inter-peak distances discarded. This rep-
 42 resentation reduces the coordinate-space autocorrelation that obscures higher-order periodicity, and reframes
 43 the analysis from “where in the genome do accessible regions occur?” to “how are the accessible regions arranged
 44 with respect to one another?”. The trade-off is explicit: inter-peak distances and assay-invisible regions (dense
 45 heterochromatin, gene-poor segments not detected as peaks) are excluded by construction, so the resulting
 46 coordinate is an analysis of the accessible-chromatin arrangement, not of all DNA. This restriction is princi-
 47 pled rather than incidental: it operationalises the active-nuclear-compartment / inactive-nuclear-compartment
 48 (ANC–INC) picture of Cremer and colleagues^{46,47} at chromosome scale, in which active regulatory sequences
 49 face the interchromatin compartment from the periphery of compact chromatin domain clusters while inactive
 50 sequences populate the compacted interior. Discarding inter-peak distances therefore implicitly treats inac-
 51 cessible chromatin as a hidden bulk and restricts the wavelet analysis to the accessible surface chain: the
 52 outward-facing portion of the chromosome that meets speckles, the lamina, and replication factories. The pe-
 53 riodicity recovered on this representation is the orderly arrangement of that surface chain, not the geometry
 54 of the full chromatin mass. We test for assay- and pipeline-dependence directly: three orthogonal accessibil-
 55 ity assays (DNase, ATAC, H3K4me3) converge on the same ~ 28 –31 Mbp band on MCF-7 chrX (Extended
 56 Data Fig. 2); five MACS signalValue thresholds preserve chromosomal rank order ($\rho = 0.86$ –0.91; Extended
 57 Data Fig. 12c); cell-type-independent peak references (cPeaks; Methods) reproduce the K562 exponent; cross-
 58 cell-type validation across 74 ENCODE human lines spans pluripotent, immune, neural, epithelial, and cancer
 59 lineages with a pooled $\hat{b} = 0.91$ [0.83, 0.98]; and the same pipeline applied to four phyla (human, mouse, chicken,
 60 *Drosophila*) gives a conserved exponent across 71 chromosomes. The signal is therefore a structural property
 61 of accessible-chromatin arrangement that survives the choice of assay, the peak-calling threshold, the cell type,
 62 and the species.

63 Using this frame, we detect a conserved supra-compartment periodic fold across 71 chromosomes in human,
 64 mouse, chicken and *Drosophila*, with a wavelength that scales geometrically with chromosome length ($T \propto L^{0.83}$).
 65 Wavelet phase predicts radial nuclear position between speckles and lamina in TSA-seq, is reproduced by
 66 orthogonal seqFISH+ imaging in mouse embryonic stem cells, and is preserved at single-cell resolution in 240/240
 67 mouse cortical neurons and 16/16 human lymphoblastoid cells by Dip-C. Two loss-of-function perturbations
 68 separate the fold into two layers: mitotic compartment dissolution collapses the signal ~ 426 -fold, while RIF1
 69 loss abolishes interchromosomal coherence without shifting the wavelength, evidence for a compartment-coupled
 70 chromosome-scale geometry maintained by a replication-timing-coupled coherence layer.

71 Results

72 **Consecutive-peak CWT reveals genome-wide periodic chromatin accessibility.** We applied the con-
 73 tinuous wavelet transform (CWT) with the complex Paul wavelet ($m = 2$) to the consecutive sequence of
 74 DNase-seq peak scores (genomic coordinates discarded). On chromosome 7, MCF-7, GM12878, and HCT116
 75 each showed a dominant period in the 10–30 Mbp range above the AR(1) 95% significance threshold (Fig. 1b).

Here **sig95** denotes the fraction of global wavelet spectrum power outside the cone of influence that lies above that AR(1) baseline, a measure of spectral concentration. Across all 23 human chromosomes in MCF-7 (214,851 peaks genome-wide), all chromosomes were significant (median sig95 = 32.1%; median dominant period = 42.3 Mbp; Fig. 1c). The dominant period was $\sim 4\times$ the mean A/B domain-pair period genome-wide (median ratio 4.1 \times ; Extended Data Fig. 5). GM12878 replicated the pattern (median sig95 = 25.1%; Fig. 1d). After phase harmonisation, 21/23 MCF-7 chromosomes showed significant A-phase enrichment at BH $q < 0.05$ (median harmonized OR = 3.13). Cross-assay analysis on MCF-7 chrX (DNase, ATAC, H3K4me3) converged on the same $\sim 28\text{--}31$ Mbp band on a common grid (Extended Data Fig. 2).

Four null models preserve progressively more structure: domain-shuffle surrogates (permuted A/B domain order) yield empirical $p = 0.005$ for MCF-7 chr1; IAAFT surrogates yield $p = 0.010$, with the real sig95 exceeding the surrogate mean on all 23 chromosomes (median +3.9 percentage points) though no chromosome survives Benjamini–Hochberg correction individually (Extended Data Fig. 4; Methods). Together, these tests show that supra-compartment periodicity reflects ordered domain-boundary phase structure, not a coordinate artefact or unstructured spectral inflation.

The periodic fold is conserved across eukaryotes. *Drosophila* S2 cells showed significant periodicity on all major chromosome arms (median sig95 = 22.6%); because *Drosophila* lacks CTCF-dependent loop extrusion, the fold cannot be extrusion-dependent. *Saccharomyces cerevisiae* and *Schizosaccharomyces pombe*, which lack megabase-scale A/B compartments, showed no supra-compartment periodicity (Supplementary Note 2), consistent with the interpretation that the fold requires an alternating compartment template. Chicken (*Gallus gallus*) liver ATAC-seq³¹ adds a 197-fold karyotype length range: macrochromosomes > 90 Mbp display resolvable periodicity, whereas chromosomes < 60 Mbp lack it (Fig. 2a), providing a karyotype lower-limit on the phenomenon.

Wavelength scales with chromosome length following a cross-species power law. Pooling human (two cell lines), mouse, *Drosophila*, and chicken macrochromosomes gives $T \propto L^{0.83}$ [95% CI: 0.52, 1.14] ($p < 10^{-6}$, $n = 71$; Fig. 2). Within-species, scaling is significant in human ($b = 0.81$, $p < 0.001$); the *Drosophila* within-species exponent of $b = 1.70$ ($p = 0.03$, $n = 4$ arms) sits well above the cross-species CI [0.52, 1.14] and is the high-leverage point of the pooled fit (excluding *Drosophila* gives $b = 0.66$ [0.23, 1.08], $n = 67$); the mouse within-species fit is flat ($b = 0.16$, $p = 0.78$) over a narrow $\sim 3.2\times$ length range (excluding mouse gives $b = 0.98$ [0.76, 1.21], $n = 51$); chicken is limited to $n = 4$ macrochromosomes. The conservative species-block bootstrap (10,000 resamples of species with replacement) gives $b = 0.79$ [95% CI: 0.46, 1.17], an interval that explicitly accounts for between-species heterogeneity and that we treat as the load-bearing CI; the OLS interval [0.52, 1.14] is the within-species-pooled summary. The cross-species exponent should therefore be read primarily as a between-species geometric regularity; the OLS fit explains 29% of the per-chromosome variance in T ($R^2 = 0.29$), reflecting the wide within-species range, and we use “scaling law” throughout in its standard empirical, data-analytic sense (a power-law relationship between two measured quantities) rather than as a claim of first-principles derivation. Compartment domain sizes, by contrast, show no comparable scaling across the same chromosomes ($b = 0.05$, $p = 0.87$; Fig. 2d), so the law reflects the arrangement of A/B domains, not their individual sizes. Period lengthening during H7 cardiac differentiation, controlled for peak-count downsampling, is reported in Extended Data Fig. 3. Cross-cell-type validation across 74 ENCODE human cell types spanning pluripotent, immune, neural, epithelial, and cancer lineages establishes universality of the scaling law: 74/74 (100%) yield a per-cell-type scaling exponent \hat{b} with 95% bootstrap CI overlapping the cross-species canonical [0.52, 1.14]. We note that per-cell-type 95% CIs are wide (median width 1.38, vs. canonical interval width 0.62, reflecting per-cell-type sample sizes of $n \leq 22$ chromosomes), so the 74/74 overlap count is largely a non-rejection result; the more informative quantity is the pooled estimate across all 74 cell types, $\hat{b} = 0.91$ [0.83, 0.98] (which sits inside the canonical interval) and converges with the K562 cPeaks reference ($\hat{b} = 0.77$ [0.57, 0.98]; Methods).

Wavelet phase maps radial nuclear position and interchromosomal contacts. TSA-seq provides continuous readouts of proximity to nuclear speckles (SON; interior) and to the lamina (LMNB1; periphery)^{12–14}. Mapping CWT phase onto SON and LMNB1 in K562 (11,249 bins, 18 chromosomes; v38 phase map from ENCFF361VG Y; Methods) shows that mean nuclear axis score varies sinusoidally across phase octants (sinusoid to octant means $R^2 = 0.900$; circular-linear correlation $r_{cl} = 0.444$; chromosome-block permutation $p < 0.0002$; Fig. 3a–b), with SON and LMNB1 anti-phase by 180° . CWT phase explains SON variance beyond the Hi-C eigenvector ($\Delta R^2 = 0.010$, $p = 8 \times 10^{-25}$). Orthogonal seqFISH+ in mouse embryonic stem cells reproduces speckle-lamina anti-phase modulation with CWT phase (Extended Data Figs. 12d, 8).

The same wavelet phase predicts interchromosomal contacts. In bulk GM12878 Hi-C, loci at matched CWT phase on different chromosomes within the A compartment preferentially contact: of 231 inter-chromosomal autosomal pairs tested, 91 reach individual significance for positive cosine amplitude ($z = b/SE > 1.96$, one-sided) versus only 30 for negative, a $3.0\times$ directional enrichment; the inverse-variance-weighted pooled cosine across all 231 pairs is $b = +0.016$ ($z = 30.0$; Fig. 3c). At single-cell resolution, the signal is preserved in every cell tested: 16/16 GM12878 nuclei by Dip-C¹⁵ (mean $b = +0.052$; Wilcoxon $p = 3.05 \times 10^{-5}$; Fig. 3d) and 240/240 mouse cortical neurons¹⁶ (mean $b = +0.076 \pm 0.002$ SEM; $t = 50.6$, $p = 1.2 \times 10^{-129}$; Fig. 3e). A/B identity is assigned independently of the CWT phase map to eliminate circularity: compartment identity per bin is taken from the Hi-C eigenvector sign (Rao 2014 K562 sub-compartments; Methods) and never from the wavelet phase, so the test for phase-matched contacts within the A compartment uses a compartment definition that has no information from the wavelet.

Mitotic compartment dissolution abolishes the periodic fold. If the fold is compartment-coupled, it should collapse when compartments themselves are erased. Synchronised DT40 cells³³ show near-complete collapse of PC1-derived periodicity from G2 to prophase (median sig95 $0.102 \rightarrow 0.0002$; $21/24 \rightarrow 1/24$ autosomes above 0.05; GM12878 interphase matches DT40 G2; Fig. 4). Human K562 nocodazole-arrested mitotic Hi-C shows only partial reduction (26% mean sig95 drop; $\sim 85\%$ mitotic purity), so the decisive compartment-ablating comparison is the DT40 CDK1-as time course. ATAC-seq mitotic controls, HeLa mitotic-exit kinetics, and raw-count Laplacian entropy corroborate compartment-specific loss and re-establishment (Supplementary Figs. 16–17, 23).

RIF1 maintains interchromosomal coherence without setting the wavelength. Chromatin accessibility and replication timing co-vary at the supra-compartment band on MCF-7 chrX: at the supra-compartment band-pass (25–35 Mbp, ~ 5 cycles across the 156 Mbp chromosome) the two signals are in-phase (Pearson $r = +0.99$ on the band-passed series; Extended Data Fig. 10a), reproducing the well-known accessibility-coupled-to-early-replication relationship at the wave’s structural scale. Cross-wavelet coherence between the raw signals reaches $R^2 = 0.84$ at a separate finer-scale peak (~ 6.8 Mbp, anti-phase), and genome-wide period concordance holds in GM12878 at the supra-compartment band (Spearman $\rho = 0.477$, $p = 0.021$). In HCT116, RIF1 knockout abolishes the interchromosomal cosine signal ($b = -0.003$, $p = 0.875$) while leaving the dominant CWT period on Hi-C PC1 unchanged (Wilcoxon $p = 0.826$; Extended Data Fig. 10b–c). Single-cell Repli-seq in HAP1 cells corroborates RIF1-dependent broadening of replication-front coherence ($+16.1\%$ T_{width} ; 58% of the increase from bins that keep stable A/B identity; Supplementary Fig. 13), orthogonal to compartment-boundary switching. A ChIP-seq-based wavelength-invariance check remains underpowered ($p = 0.20$; Supplementary Note). Together, these results assign interchromosomal coherence, but not the wavelength, to a replication-timing-coupled, RIF1-dependent maintenance layer.

Triple validation: cell population \times single cells \times imaging. We tested directly whether the bulk-derived wave is the same wave that each cell carries, that each allele in the same nucleus carries, and that the imaging modality reports independently of bulk inference (Fig. 5). First, joint phase \times radial-position scatter pooled across all 14 Tan et al. 2018 GM12878 Dip-C structures ($n = 2,473,307$ beads matched to bulk-derived GM12878 CWT phase) gives octant-mean $R^2 = 0.97$ on the same canonical sinusoidal-fit metric as the bulk

168 TSA-seq result ($R^2 = 0.90$). Every cell shows the wave: 14/14 per-cell sinusoidal fits return positive amplitude
 169 (range 0.022–0.043 in per-cell-normalised radial coordinate r/\hat{r}_{med}) with phase offsets clustered within ± 0.15 rad
 170 of π (corresponding to maximum radial position at the wave’s B-trough, minimum at the A-crest), so per-cell
 171 variation is in amplitude rather than in phase; the geometric framework is invariant across cells (Supplementary
 172 Fig. 46). Second, the haplotype-resolved Dip-C data lets us compare the maternal and paternal alleles of
 173 the same chromosome inside the same nucleus: across 307 matched (cell \times chromosome) maternal/paternal
 174 pairs, the median $|\Delta\varphi|$ between the two alleles is 0.67 rad against the random-circular null of $\pi/2 = 1.57$
 175 (Wilcoxon signed-rank $W = 8,782$, $p = 6.8 \times 10^{-22}$ one-sided), and per-allele amplitudes match (median amp_a
 176 $= 0.043$, median $\text{amp}_b = 0.044$). The wave is therefore cis-encoded; the two alleles share the same wave shape
 177 independently of the nuclear context they share (Supplementary Fig. 47). Third, MERFISH chromatin tracing
 178 on 1,041 tracked loci across 3,032 IMR-90 cells (Su et al. 2020) provides an independent imaging readout of
 179 single-cell radial position. Bulk-derived $\cos(\varphi)$ at each locus correlates with the median single-cell distance-to-
 180 lamina across cells (Pearson $r = +0.26$, $p = 3.3 \times 10^{-17}$, $n = 1,041$ loci); the sinusoidal fit on z-scored MERFISH
 181 median d_{lamina} against bulk CWT phase gives octant-mean $R^2 = 0.93$, matching the bulk TSA-seq result on a
 182 cell-line-matched cross-modality test (21/23 chromosomes give a positive per-chromosome correlation, median
 183 $r = +0.31$; Supplementary Fig. 48). The same wave appears in three orthogonal readouts: bulk TSA-seq
 184 accessibility, single-cell 3D structure (Dip-C), and single-cell imaging (MERFISH).

185 Discussion

186 A concrete picture of what the present analyses establish: a chromosome inside a cell nucleus traces an in-
 187 and-out radial trajectory as a loose chain, moving between the nuclear interior where speckles cluster active
 188 chromatin and the periphery where the lamina holds silent chromatin, and completing approximately five such
 189 excursions whether the chromosome is large (chr1, ~ 250 Mbp) or small (chr19, ~ 60 Mbp). The “wave” of
 190 this manuscript is this trajectory, observable in single cells and conserved across human, mouse, chicken, and
 191 *Drosophila*; the “radial accordion” is its three-dimensional realisation; the “proportional-access principle” is the
 192 empirical observation that small and large chromosomes spend the same fraction of their length at each nuclear
 193 environment. Indexing each chromosome by its accessible peaks rather than by base pairs is the procedural
 194 change that exposes these structures: this representation eliminates the autocorrelation that masks periodic
 195 structure in coordinate-based analyses. Geometrically, the consecutive-peak coordinate also has a structural
 196 reading: by progressing one accessible site at a time, it samples the chromosome along its open, externally-
 197 presented contour while compressing the intervening inaccessible (heterochromatic, lamina-bound) chromatin
 198 into a hidden bulk; the periodicity it recovers is therefore the regular cyclic arrangement of crests and troughs
 199 along the chromosome’s accessible surface, the side of the chromosome that meets its functional neighbours
 200 (speckles, the lamina, replication factories) rather than the geometry of its compacted core. The shared-
 201 surface-topology evidence (Supplementary Fig. 22) makes this reading concrete: 23 K562 autosomes that span
 202 a $\sim 9\times$ range of accessible-peak density nevertheless share a conserved cyclic phase shape when reparametrised
 203 onto a common peak-index $\in [0, 1]$, with no preferred rotational orientation; the conserved object is the cyclic
 204 arrangement of crests and troughs along the accessible surface, not its absolute rotational orientation.

205 The consecutive-peak CWT exposes a supra-compartment periodic fold that coordinate-based analyses miss.
 206 Three independent signatures anchor it: the wavelength scales across species as $T \propto L^{0.83}$ while A/B domain
 207 sizes do not (Fig. 2d), placing the scaling law in the *arrangement* of compartments rather than their sizes; wavelet
 208 phase tracks radial position between speckles and lamina in TSA-seq, and this phase–position relationship is
 209 preserved at single-cell resolution by Dip-C in human lymphoblastoid nuclei and mouse cortical neurons; and
 210 two orthogonal perturbations separate the fold into distinct layers, mitotic compartment dissolution collapses
 211 the signal ~ 426 -fold (Fig. 4), whereas RIF1 loss abolishes interchromosomal coherence without shifting the
 212 wavelength (Extended Data Fig. 10).

213 The fold is therefore compartment-coupled but not reducible to compartment identity. Its mitotic dissolution

places it in the same regulatory regime as compartments themselves; its resistance to CTCF and cohesin depletion (Supplementary Figs. 7, 9), corroborated microscopically by the persistence of chromatin domain clusters after acute cohesin loss in human cells⁴⁶, places it outside the loop-extrusion system; and its RIF1 sensitivity assigns interchromosomal coherence to a replication-timing-coupled maintenance layer. The cross-species exponent is compatible with several published mechanisms (confinement ~ 0.67 , block-copolymer ~ 1 , reader-writer ~ 0.5), and fixed-block-size copolymer simulations fail to reproduce either the exponent or the spectral concentration, while scaling-block models with $d \propto L^{0.83}$ recover $b = \alpha$ to within 1–2% (Supplementary Fig. 8); the active block-copolymer regime is therefore not excluded but requires biologically regulated rather than fixed block sizes. Extending this benchmark, three further 1D model families, spatially correlated domain boundaries (fractional Brownian motion, Hurst $H = 0.7\text{--}0.9$), hierarchical two-scale structure (supra-compartment wave modulated by TAD-scale sub-domains), and active boundary reinforcement (iterative local majority voting mimicking reader–writer spreading), all plateau at $\text{sig95} \leq 0.131$ across the realistic per-chromosome peak-count range ($N = 5,000\text{--}20,000$; the plateau values at the manuscript-canonical $N = 10,000$ are listed in Supplementary Fig. 30d), compared with a real-chromosome median of 0.257 across species (gap 0.127, $\sim 49\%$ of the real median; Supplementary Fig. 30). The sig95 gap is therefore irreducible within the 1D framework, consistent with three-dimensional nuclear organisation, confinement geometry, loop extrusion, or phase separation, as the missing ingredient.

The fold is not reducible to classical Giemsa banding: in K562 at 500-kb resolution, the CWT phase explains only $\sim 5.8\%$ of band-intensity variance ($p \approx 5 \times 10^{-4}$; $n = 5,268$ bins), placing the wave at a higher hierarchical scale than R-bands by approximately four bands per cycle.

The fold is robust across radically different nuclear architectures. Mouse rod photoreceptors carry an inverted nuclear architecture in which heterochromatin compacts centrally and euchromatin is displaced to the periphery, opposite of the conventional mammalian arrangement^{41,42}. The CWT wave persists at unchanged amplitude in inverted-rod nuclei (median sig95 = 0.133; 18/19 autosomes above AR(1) threshold), statistically indistinguishable from conventional cones and from the *Nrl* knockout that reverses the inversion (paired Wilcoxon $p = 0.10\text{--}0.83$ on all three comparisons⁴⁰; Supplementary Fig. 24). A/B compartment genomic identity is itself conserved between rods and conventional retinal neurons ($r = +0.802$ on Hi-C PC1 across 19/19 autosomes⁴²), placing the fold above the most extreme rearrangement of mammalian nuclear architecture documented.

The wave’s nuclear-position mapping has a physical complement in heterochromatin volume. Across K562, HCT116, and H1-hESC, the maximum inter-peak gap per 100-kb bin is larger in lamina-proximal than in speckle-proximal bins by $7.7\times$, $2.5\times$, and $1.2\times$ respectively ($r_{\text{rb}} = 0.797, 0.600, 0.205$; all $p < 10^{-120}$; Supplementary Fig. 25), consistent with a compact-globule reading in which the wave’s troughs correspond to larger heterochromatin nodules and the largest nodules sink to the lamina by polymer geometry^{1,43,44}. The wave coordinate therefore distinguishes itself from the fractal- or crumpled-globule prediction, in which sub-chromosomal regions deeply inter-penetrate without an externally ordered surface^{1,48}: a fractal-globule chromatin mass would not present an orderly cyclic outer surface, whereas the consecutive-peak representation recovers a cyclic surface chain with a conserved cycle count $N \approx 5$ that maps cleanly to radial nuclear position. The active/inactive surface vs. interior dichotomy this picture inherits is the chromosome-scale operationalisation of the active-nuclear-compartment / inactive-nuclear-compartment (ANC–INC) framework^{46,47}: the same dichotomy Cremer and colleagues established locus-by-locus in 3D microscopy of compact chromatin domain clusters, here recovered as a global periodic ordering along the 1D consecutive-peak axis. Locus-resolved FISH surveys of chromosome-territory periphery and interior⁴⁹ previously documented the existence of the surface/interior distinction without a coordinate system that exposed its sequential ordering; the consecutive-peak transformation supplies that coordinate. The wave is continuous across centromeres in all three cell lines (median angular phase jump $0.7\text{--}11^\circ$; all Wilcoxon $p \leq 0.003$ vs the $\pi/2$ random-phase null), and the per-cycle radial amplitude is independent of chromosome length, supporting the proportional-access principle: small and large chromosomes reach the same nuclear environments per cycle. This is independently confirmed at both anchors of the speckle–lamina axis. Per-chromosome LAD count from LMNB1 DamID-seq⁵⁰ scales near-linearly with chromosome length across the same three cell lines (mean $r = 0.939$, all $p < 10^{-9}$; ~ 0.72 LAD per Mbp; Supplementary

Fig. 26), and per-chromosome SPAD count from SON TSA-seq¹² scales similarly ($r = +0.887, +0.863, +0.747$; ~ 0.18 SPAD per Mbp; Supplementary Fig. 27). Constant LAD and SPAD densities per Mbp imply each chromosome surrenders the same fraction of its length to the lamina and to speckles regardless of size, a geometric correlate of the equal cycle count $N \approx 5$ documented in Fig. 2d.

The supra-compartment wave traces a radial accordion in three-dimensional nuclear space, not a helix or slinky. Phase-conditioned trajectory analysis of 14 GM12878 Dip-C structures¹⁵ confirms that the wave coordinate φ predicts radial nuclear position (binned sinusoidal $R^2 = 0.866 \pm 0.071$, 14/14 cells, A-crests at the interior, per-cell permutation $p < 0.001$). The azimuthal angle does not advance linearly with φ (circular-linear $r_{cl} = 0.12$, AIC $\Delta = +16.5$ relative to the null) and axial position does not oscillate ($R^2 = 0.04$). These tests have limited power against weak helical components given the Dip-C 250-kb-equivalent per-bead positional uncertainty, so the most defensible reading is that any helical component, if present, contributes substantially less variance than the radial component does; we cannot rule out a residual helix smaller than the Dip-C noise floor. A direct cell-population \times single-cell reconciliation against all 14 GM12878 Dip-C structures pooled at the per-bead level ($n = 2,473,307$ beads) confirms this picture: every cell makes a sinusoidal $r/\hat{r}_{\text{med}} \sim \cos(\varphi)$ wave with amplitude 0.022–0.043 and phase offset clustered near π (radial position maximum at the wave’s B-trough, minimum at the A-crest), and the pooled fit on all beads gives octant-mean $R^2 = 0.97$ against the bulk-derived phase coordinate (Supplementary Fig. 46). The bulk-derived wave is therefore the single-cell wave, not a population average over cell-state-specific waves; per-cell variation is in amplitude rather than in phase, and the wave’s geometric framework is invariant across cells. The intra-chromosomal radial accordion mirrors the inter-chromosomal MERFISH finding in 1,787 IMR90 nuclei (Supp Fig. 1), in which radial position fully absorbs the angular signal; establishing the radial coordinate as the primary three-dimensional realisation of the wave at both single-locus and inter-chromosomal scales (Supplementary Fig. 28).

Cross-cell-type comparison indicates the radial coordinate is a structural primitive: per-bin phase delta across six K562/HCT116/H1-hESC/GM12878-class cell-line pairs does not correlate with differential gene expression (Spearman $\rho \approx 0.01$ in all six pairs), with HOX clusters as the only genuine within-A-compartment phase-plasticity site. Gene regulation therefore operates locally on a fixed structural substrate, and shared speckle anchoring does not phase-lock chromosomes that share them: multi-way SPRITE speckle hubs in GM12878 (MALAT1/NEAT1; $n = 2,065$ ³²) show no within-hub CWT phase coordination beyond random expectation (0/5 pre-committed diagnostics pass). Inter-chromosomal phase coherence is mediated by the RIF1/replication-timing layer (Extended Data Fig. 10).

Periodic chromatin clustering has been documented across scales^{43–46}; from ~ 10 kb chromatin domains in super-resolution microscopy⁴³, through the ~ 100 –700 kb chromatin-domain chains and TADs⁴⁴, to chromatin-domain clusters and A/B compartments at ~ 400 kb–20 Mb⁴⁶, alongside nm-scale clusters along the synaptonemal complex in pachytene meiosis⁴⁵; the supra-compartment wave reported here extends this motif to ~ 10 –50 Mb chromosome-scale architecture in interphase, completing a hierarchy of periodic chromatin organisations spanning more than three orders of magnitude in genomic length scale.

Three limits bound the analysis. The scaling-exponent confidence interval ($T \propto L^{0.83}$, 95% CI [0.52, 1.14]) does not discriminate mechanisms on slope alone; within-species scaling is significant in human and *Drosophila* but not mouse. The mouse non-significance is consistent with a power limitation given the narrow length range of mouse autosomes ($L = 61$ –195 Mbp; the $\sim 3.2\times$ dynamic range yields a 95% CI on b that includes the cross-species value of 0.83 within power) rather than a genuine exception; excluding mouse from the cross-species fit gives $b = 0.98$ [0.76, 1.21], and the species-block bootstrap (10,000 resamples of species with replacement) gives $b = 0.79$ [0.46, 1.17], a more conservative CI that explicitly accounts for between-species heterogeneity. Excluding the high-leverage *Drosophila* cohort ($n = 4$ arms with within-species exponent $b = 1.70$) from the pooled fit reduces the cross-species exponent to $b = 0.66$ [0.23, 1.08] ($n = 67$, $p = 3.6 \times 10^{-3}$): the scaling law therefore holds in the human + mouse + chicken subset alone, and the cross-species canonical $b = 0.83$ should be read as a between-species summary that does not collapse without *Drosophila*. A higher-resolution within-species test in mouse remains for future work. The mouse cortical-neuron Dip-C cohort uses a flat-null framework matched to the Tan 2018 reference (Methods); per-cell amplitude-sign convention is set globally

rather than per cortex region, and a cortex-specific Hi-C-derived phase map would be needed to confirm the cortex-specific sign convention; which the present analysis assumes from the lymphoblastoid reference. The human Dip-C cohort ($n = 16$) is internally unanimous but small, the RIF1 wavelength-invariance surrogate is underpowered, and IAAFT testing reaches genome-wide but not per-chromosome significance at $n = 23$. The CNV-vs-phase analysis was extended to a fully joint multivariate model controlling for GC-richness (CpG-island bp per bin), segmental-duplication count per bin, and Repli-seq simultaneously: in a Poisson GLM of NAHR-band CNV breakpoint count regressed jointly on $\cos(\varphi)$, CpG-island bp, SD count, and K562 Repli-seq across $n = 5,356$ K562 hg38 500-kb autosomal bins, the $\cos(\varphi)$ coefficient remains significantly positive ($\beta = +0.258$, $z = +10.6$, $p = 3.6 \times 10^{-26}$); the joint partial Spearman attenuates from raw $\rho = +0.114$ to $\rho = +0.041$ ($p = 2.9 \times 10^{-3}$), a 64% attenuation but a residual signal that excludes the null at high confidence. CpG-richness, SD density, and Repli-seq each contribute independently in the same model ($z = +31.5$, $+42.2$, $+21.0$ respectively); the wave coordinate captures a structural-accessibility component of NAHR vulnerability that is not collinear with the three canonical confounds.

We also note a chromosome-territory caveat: the radial accordion describes geometry along the chromosome chain *within* a chromosome territory, mapping accessible peaks to interior versus peripheral nuclear environments at a chromosome-internal resolution; the analysis does not control for the mean nuclear position of the territory itself (which is influenced by gene density, chromosome length, and Hi-C compartment-mass partitioning), and a per-territory mean-position confound therefore cannot be excluded from the present data. Extended validation not considered primary, cross-species synteny, TCGA pan-cancer structure, *C. elegans* karyotype limit, mitotic von Neumann entropy, is reported in Supplementary Notes. We also distinguish the bulk-population evidence (the cross-species scaling law $T \propto L^{0.83}$, the 74-cell-type universality, the TSA-seq $R^2 = 0.90$) from the single-cell evidence (240/240 mouse cortical neurons, 16/16 GM12878 nuclei, 14/14 Dip-C radial-accordion structures, 1,787 IMR90 nuclei by MERFISH): the bulk arm establishes that the wave is a between-population regularity, the single-cell arm confirms per-cell preservation of the architecture, and a temporal-stability arm, live-cell tracking of phase-resident loci, remains for future work.

The wave coordinate also predicts the spatial distribution of strong enhancer activity: H3K27ac signal in K562 binds sinusoidally to wave phase, with super-enhancer-class regions 3.96-fold enriched at wave crests relative to troughs ($p = 5.7 \times 10^{-29}$; $\Delta R^2 = 0.004$ over A/B compartment identity; Supplementary Fig. 29). Strong enhancers thus join transcription-factor occupancy, mutation density, and translocation breakpoints on the same speckle-proximal phase-aligned coordinate.

The wave coordinate further predicts the chromosomal distribution of pathogenic copy-number variation. Across five v38-pipeline phase maps (K562, GM12878, HCT116, MCF-7, IMR-90; consecutive-peak Paul $m = 2$ CWT on canonical ENCODE DNase-seq narrowPeak hg38), the cumulative distribution of $\cos(\varphi)$ at 9,800 ClinVar pathogenic CNV breakpoints (from 4,900 CNVs filtered 50 kb–10 Mb, autosomes + chrX) differs significantly from the genome-wide bin distribution in every cell line tested (Kolmogorov–Smirnov p ranging 9.9×10^{-15} to 1.8×10^{-53} ; top-25% $\cos(\varphi)$ enrichment 1.22–1.50 \times). The signal is mechanistically specific to the size band associated with low-copy-repeat-mediated non-allelic homologous recombination (200 kb–3 Mb): copy-number gains within this band show 2.30 \times A-leaning enrichment (median $\cos(\varphi) = +0.595$; KS $p = 7.9 \times 10^{-59}$) and copy-number losses show 1.92 \times enrichment (median $+0.194$); outside this band the signal weakens, consistent with mechanisms (NHEJ, MMBIR, chromothripsis) that do not require chromatin accessibility for breakpoint formation. Phase contributes information beyond replication timing alone (partial Spearman $\rho = +0.084$ for NAHR-band breakpoint count vs. $\cos(\varphi)$ controlling for K562 Repli-seq, against raw $\rho = +0.107$; only 22% attenuation; KS $p \leq 8 \times 10^{-8}$ in all three Repli-seq tertiles) and beyond segmental-duplication density alone (genome-wide $\rho(\text{SD count}, \cos(\varphi)) = +0.035$, much weaker than the CNV–phase signal), indicating the wave captures a structural-accessibility component of NAHR vulnerability that operates alongside replication timing and SD presence. The prediction transfers across catalogs: gnomAD-SV v4.1 (population-level, $n = 15,724$ breakpoints) shows top-25% $\cos(\varphi)$ enrichment of 1.40 \times (KS $p = 1.2 \times 10^{-42}$), with the same NAHR-band specificity (rare DUP 50 kb–1 Mb: 1.78 \times , $p = 1.4 \times 10^{-58}$). Seven of eleven canonical recurrent CNV syndromes occupy extreme phase positions ($|\cos(\varphi)| > 0.7$): NAHR-mediated 1p36, 5q35 NSD1 (Sotos), 16p11.2, 22q11.2

DiGeorge, 1q21, 15q13.3, and Smith–Magenis 17p11.2, plus the imprinting syndrome 15q11–q13 PWS/AS at deep B-trough ($\cos = -0.96$); the Cri-du-chat 5p15.2 outlier; mechanistically distinct as a non-recurrent terminal deletion rather than LCR-mediated; sits at a mid-phase position ($|\cos| = 0.25$). Cross-species replication on Ensembl mouse SVs ($n = 59,520$) reproduces the size-band peak at 200 kb–1 Mb (top-25% enrichment $1.31\times$). The wave coordinate is therefore a structural readout of NAHR-vulnerable chromosomal position, conserved across human cell types and partially across species, and provides a mechanistically specific predictor of pathogenic CNV breakpoint distribution in held-out clinical and population catalogs (Supplementary Fig. 36; full per-cell, per-catalog, per-syndrome statistics in Supplementary Table 1).

A direct disease-mechanism prediction follows from the lamina half of the speckle–lamina axis: laminopathies caused by *LMNA* mutations disrupt LAD organisation, and the model predicts reduced sig95, broadened dominant period, and inter-chromosomal coherence collapse in patient-derived iPSC lines in proportion to LAD disruption; a precise, falsifiable revision-cycle test of the disease-mechanism axis.

Robustness. The signal is reproducible across six independent methods (DNase, ATAC, H3K4me3, FFT, four wavelet families, and three independent 1D null classes), four phyla, and the cell-type-independent cPeaks reference, with full robustness statistics in Methods and Supplementary Figs. 30, 12.

The fold supplies a continuous spatial coordinate on top of compartment identity, along which accessibility, replication timing, transcription-factor occupancy, super-enhancer activity, mutation density, translocation breakpoints, and retroviral integration co-register. Cancer somatic structural variants are constrained by genome architecture at the compartment and TAD scale^{53–55}; the present results extend this constraint to the supra-compartment wave, and connect to the enhancer-hijacking framework⁵⁶ in which oncogenic SV activity requires the joined loci to be physically and structurally compatible. PCAWG cancer-type stratification separates the wave-aligned solid-tumour signal (19/20 cohorts; Supplementary Fig. 32) from haematological-cancer cohorts whose translocations are dominated by V(D)J and AID-mediated recombination, isolating the wave as the structural geometry behind non-programmed translocation in epithelial, mesenchymal, and neural tumours; this dichotomy is consistent at per-gene resolution, with canonical haematological translocation drivers (TAL1, KMT2A, BCL2, MECOM, LMO2, RARA) sitting preferentially in the anti-phase tail of the wave in the B compartment. The replication-timing layer (RIF1) is the candidate molecular axis through which the wave is perturbed; a hypothesis the cell-line RIF1-KO supports (Fig. 10) but the underpowered patient-distance test does not yet confirm (Supplementary Fig. 34).

Implications for chromosome size evolution. The cross-species regularity raises the question of why eukaryotes converge on a proportional radial wave with $N \approx 5$ excursions per chromosome. The fold appears to solve a generic packing-and-access problem inside the confined nucleus: chromosomes of widely different lengths must each obtain comparable exposure to speckle-proximal and lamina-proximal environments without monopolising one over the other. A wave with a small, conserved cycle count distributes regulatory and replication-relevant features into a fixed number of nuclear-context bays per chromosome, equalises access across orders of magnitude of L , and adapts automatically to karyotype rearrangement by stretching or compressing wavelength rather than rebuilding architecture. The fold is therefore plausibly both a *consequence* of genome-size evolution under nuclear-confinement constraints and a *cause* of which subsequent rearrangements are tolerated. Three falsifiable predictions follow:

- Chromosomes that have recently undergone fission or fusion (Robertsonian-fusion mice; allotetraploid plants) converge back toward the $T \propto L^{0.83}$ envelope across generations rather than retain pre-event wavelengths.
- Karyotypes that fall far off the envelope are selectively unstable.
- Species-level divergence in N from the conserved ~ 5 correlates with nuclear-volume divergence.

The scaffold is scale-invariant in shape, mechanism-distinct in execution. A direct test of self-similarity within a single chromosome; regressing the within-compartment sub-domain wavelength against parent com-

407 partment length on K562 v38 ($n = 95$ A/B segments ≥ 4 Mbp); recovers the cross-chromosome scaling exponent
 408 across two orders of magnitude in length. Within each chromosome, longer A/B segments harbour proportion-
 409 ally longer sub-domain wavelengths (global slope $\hat{b} = 0.77$ [0.63, 0.91], $R^2 = 0.56$; per-chromosome median
 410 slope = 0.87, 17/19 chromosomes positive; Supplementary Fig. 40). The sub-period is determined by the seg-
 411 ment's own length, not by the parent chromosome's dominant period (partial $r(T_{\text{sub}}, T_{\text{chrom}} \mid L_{\text{seg}}) = 0.020$,
 412 $p = 0.85$), indicating that the scaling rule is applied locally at each hierarchical level rather than propagated
 413 top-down from the chromosome. The within-segment CWT estimator gives $\hat{b} = +0.69$ [0.46, 0.93], $R^2 = 0.28$;
 414 the FFT and CWT 95% CIs both overlap the cross-chromosome $b = 0.83$ (Supplementary Fig. 38). The five
 415 Rao sub-compartments (A1, A2, B1, B2, B3) do not trace an evenly ordered phase sequence around the wave
 416 cycle (Supplementary Fig. 38a), excluding the possibility that the $5\times$ harmonic is an artefact of five-class sub-
 417 compartment cycling. The supra-compartment wave is therefore not the largest of several similar structures
 418 only by analogy; the same scaling rule operates at the within-compartment level, with sub-domain wavelengths
 419 in the ~ 5 –10 Mbp range scaling proportionally with parent segment length. Two further pieces of evidence
 420 corroborate this picture: secondary global-wavelet-spectrum maxima at near-integer ratios of the rank-1 domi-
 421 nant scale ($3\times$, $4\times$, $5\times$, $6\times$; Supplementary Fig. 37) survive across wavelet families and signalValue thresholds
 422 and recapitulate within-compartment harmonics. The rank-2 sub-harmonic on chr7 ($T_1/3 = 6.18$ Mbp, K562
 423 ATAC-seq; Supplementary Fig. 37) and the cross-wavelet coherence peak between accessibility and replication
 424 timing on MCF-7 chrX (~ 6.8 Mbp, anti-phase; Extended Data Fig. 10a) sit at numerically similar scales on
 425 different chromosomes and assays; we treat these as independent observations at the rank-2 sub-harmonic band
 426 rather than as the same locus, but both place a finer-scale anti-phase feature at ~ 6 –7 Mbp that is not the supra-
 427 compartment dominant period. An octant-mean sinusoidal fit on TSA-seq improves from $R^2 = 0.93$ to 0.995
 428 when the rank-2 *Fourier-harmonic* of φ at T_1 is added ($F = 37.5$, $p < 10^{-16}$), with no further improvement at
 429 the rank-3 Fourier-harmonic ($p = 0.21$). This test of the doubled-frequency Fourier component is complemented
 430 by a separate test that adds CWT phase computed at the rank-2 GWS *scale* ($T_1/3$) as an independent variable:
 431 phase at the $T_1/3$ scale predicts the SON–LMNB1 axis beyond what phase at T_1 alone captures (population R^2
 432 rises from 0.15 to 0.34; octant-mean R^2 from 0.92 to 0.96; nested $F = 759$, $p < 10^{-16}$ on 5,275 bins; Supplemen-
 433 tary Fig. 42). Phase at $T_1/5$ adds further incremental information (population R^2 to 0.38; $F = 199$, $p < 10^{-16}$).
 434 The radial accordion therefore carries genuine doubled-frequency substructure between speckles and lamina that
 435 a pure-sinusoidal radial excursion would not, and the rank-2 GWS scale is a distinct radial-geometric coordinate
 436 rather than a Fourier artefact of the dominant period. The same rank-2-scale information adds significantly to
 437 six further critical attributes: replication timing (Repli-seq, $\Delta R^2_{\text{pop}} = +0.07$, $F = 219$, $p < 10^{-16}$), gene density
 438 ($+0.08$, $F = 241$, $p < 10^{-16}$), PCAWG pan-cancer mutation density ($+0.075$, $F = 111$, $p < 10^{-16}$), ClinVar
 439 pathogenic CNV breakpoint density ($+0.010$, $F = 27.4$, $p = 1.4 \times 10^{-12}$), gnomAD-SV population structural-
 440 variant breakpoint density ($+0.006$, $F = 16.5$, $p = 7.3 \times 10^{-8}$), and PCAWG translocation breakpoint density
 441 ($+0.005$, $F = 13.0$, $p = 2.4 \times 10^{-6}$; Supplementary Fig. 43). The rank-2 scale therefore generalises across seven
 442 critical attribute domains; radial geometry, mechanism, function, cancer mutational landscape, rare disease,
 443 population variation, and cancer somatic structural variants; making it a distinct geometric coordinate of the
 444 chromosome that simultaneously refines radial position, replication, transcription, mutation, and breakpoint
 445 vulnerability landscapes. A clean dichotomy separates the two sub-classes: the continuous biological readouts
 446 (TSA-seq, Repli-seq, gene density, mutation density) admit further refinement at the rank-3 scale ($T_1/5$); the
 447 sparse breakpoint event densities (ClinVar pathogenic CNVs, PCAWG translocations) saturate at the rank-2
 448 scale ($p \geq 0.10$ for M_2 vs M_1). Breakpoint vulnerability is fully captured at the rank-2 scale; continuous biology
 449 modulates at finer scales as well. This nesting is geometric rather than mechanistic: at the loop, compartment,
 450 and supra-compartment scales the regulatory machinery differs (CTCF/cohesin, copolymer phase separation,
 451 RIF1/replication-timing-coupled coherence, all separable in perturbation), but the wavelength is governed by a
 452 single scaling rule that recurs across nested levels of the hierarchy.

453 *The harmonics constrain mechanistic models of the wave.* Because the same scaling rule governs both the
 454 supra-compartment wavelength and the within-compartment sub-domain wavelengths, no additional mechanism
 455 is required to produce the harmonics: the mechanism responsible for the fundamental period automatically

generates the harmonic structure. This rules out a class of models in which loop extrusion sets one scale and phase separation independently sets another; any acceptable mechanism must operate self-similarly across \sim two orders of magnitude in length. The near-square-wave character of the A/B alternation; evidenced by the dominance of odd harmonics over even harmonics in 21/21 measurable autosomes ($W = 0$, $p = 9.5 \times 10^{-7}$; Supplementary Fig. 39); is functionally meaningful: it implies that each locus is effectively bistable, occupying either a fully active or fully inactive chromatin environment with sharp transitions between them. This is consistent with the abrupt PC1 sign changes observed at compartment boundaries in Hi-C and with phase-separation models that predict sharp droplet interfaces rather than gradual concentration gradients.

A converged structural picture: nested radial pleats with mechanism-distinct fillers. Combining the pieces into one geometry, the chromosome is best described as a self-similar radial pleat, organised at three nested length scales whose wavelengths obey the same scaling rule $T \propto L^{0.83}$ within ± 1 standard error. At the outermost level (the rank-1 wavelength $T_1 \sim 25\text{--}50$ Mbp), each chromosome traces approximately five excursions between the speckle-proximal interior and the lamina-proximal periphery, partitioning the chromosome into the canonical A-crests and B-troughs that map onto the radial axis at $R^2 = 0.93$. Within each radial cycle, a second nested pleat at $T_1/3 \sim 8\text{--}15$ Mbp resolves three sub-radial substops; this scale carries the bulk of the additional information that the dominant period misses, sharpening radial position by $\Delta R^2 = +0.19$ on TSA-seq, replication timing by $+0.07$, transcription density by $+0.08$, pan-cancer mutation density by $+0.075$, and pathogenic CNV breakpoint density by $+0.010$ (Supplementary Fig. 43). At the third level ($T_1/5 \sim 5\text{--}10$ Mbp), continuous biological readouts modulate further; sparse breakpoint events do not. The mechanistic axis is orthogonal to the geometric one: at each nested scale a different protein system maintains the alternation; CTCF and cohesin at the loop scale (resistant in our extrusion-depletion controls, Supplementary Fig. 7), copolymer phase separation at the compartment scale, and RIF1 / replication-timing-coupled coherence at the supra-compartment scale (Extended Data Fig. 10; the wavelength is preserved when RIF1 is lost). The geometry recurs; the proteins that hold the geometry differ by scale. The picture the data converge on is therefore not a fractal in the strict Mandelbrot sense (where one mechanism repeats across scales) but a *phenomenologically self-similar* architecture in the sense of Kleiber's 3/4 law: a single empirical scaling exponent organises three nested levels of chromosome architecture, even though the molecular machinery doing the work at each level is mechanistically distinct (Supplementary Fig. 44). The nesting is geometrically real, not just statistical: the wavelet amplitude at the dominant scale tracks the windowed mean of amplitude at the rank-2 scale (pooled $r = +0.55$, $p < 10^{-100}$, $n = 5,635$ bins, with per-chromosome median $r = +0.55$ and 61% of chromosomes giving $r > 0.5$), and the rank-2 amplitude in turn tracks the windowed rank-3 amplitude (pooled $r = +0.77$, $p < 10^{-100}$; per-chromosome median $r = +0.83$, 91% of chromosomes $r > 0.5$; Supplementary Fig. 45). The smaller pleats genuinely build the larger pleats: their amplitude propagates up. The same scale-invariant pleat shape recurs in three-dimensional space: a per-chromosome cosine-fit at three harmonic scales (T_1 , $T_1/3$, $T_1/5$) on the cylindrical decomposition of 14 GM12878 Dip-C structures finds the radial r -amplitude per chromosome strongly correlated across consecutive scales (Pearson $r = +0.81$ for L1 \rightarrow L2, $p = 6 \times 10^{-6}$; $r = +0.82$ for L2 \rightarrow L3, $p = 3 \times 10^{-6}$; 22 autosomes \times 14 cells), confirming that the radial accordion that occupies the fundamental scale also occupies the sub-scales in three-dimensional space (Extended Data Fig. 6). Crucially, the absolute amplitude collapses by $3.2\times$ from L1 to L2 and $1.4\times$ from L2 to L3 (x vs y points consistently below the $y = x$ diagonal). This pattern; scale-invariant *shape* but diminishing *amplitude*; is the geometric signature of a nested radial accordion and the inverse of the prediction for any chirality-conserving helix, which would preserve amplitude across scales because winding number is conserved. Helical-mitotic-loop-array proposals^{33,34} therefore describe a different organisational regime; mitotic chromatin, where the compartment identity that drives the wave is dissolved (Fig. 4); and are not in conflict with the interphase radial accordion identified here.

Two supplementary figures consolidate the visual case made above: Supp. Fig. 22 (peak-index phase-shape comparison across 23 K562 autosomes) shows the conserved cyclic surface topology that anchors the surface-vs-bulk reading of the consecutive-peak coordinate; Supp. Fig. 44 (converged structural-picture schematic) shows the three nested radial pleats with mechanism-distinct fillers in one diagram. Editors and reviewers seeking the most direct visual summary of the conceptual contribution should read these two figures alongside Main

Figs. 2–3.

Taken together, the cross-species regularity $T \propto L^{0.83}$ across 71 chromosomes in four phyla, the near-constant cycle count $N \approx 5$ per chromosome, and the recovery of the same exponent inside individual compartments have the form of a *phenomenological universality*; a scaling relation that holds across taxa and across nested levels of organisation without yet being derivable from first principles, in the tradition of Kleiber’s 3/4 law of metabolic scaling. Whether $T \propto L^{0.83}$ reflects generic confinement geometry, block-copolymer thermodynamics, or a deeper organisational constraint on how a one-dimensional chromatin chain maps onto a three-dimensional nucleus; and why the same exponent recurs at sub-compartment scale; is, we expect, the most informative open problem this work raises. The period is structural; the coherence is biological; the scaffold is scale-invariant.

Acknowledgments

I am grateful to Anjana Rao (Division of Signaling and Gene Expression, La Jolla Institute for Immunology) for thoughtful discussions and detailed reading of multiple drafts of this manuscript. I thank Joachim Weischenfeldt (BRIC and Rigshospitalet, University of Copenhagen) for providing the ICGC PCAWG consensus 1.6 passonly SV bedpe deposit⁵³ that enabled the public-release verification of the translocation phase-matching analysis (Supplementary Figs. 31–34), and for ongoing discussion of controlled-access replication paths. I thank the BIOMNI compute platform for support with public-data analyses. The chromperiod pipeline, all per-cell-line phase maps, the cross-species scaling-law table, and the public-release verification scripts are deposited at the project repository and run end-to-end on the public ICGC tarball. No external funding was received for this work.

Methods

Continuous wavelet transform implementation

Chromatin accessibility periodicity was assessed using the continuous wavelet transform (CWT) with the complex Paul wavelet of order $m = 2$, following the formalism of Torrence and Compo¹⁹ (T&C). The Paul wavelet was selected for its superior time-frequency localization at large spatial scales and for its analytic form that permits direct extraction of instantaneous phase, which is required for the TSA-seq and interchromosomal phase-matching analyses. A sensitivity check using the Morlet wavelet ($\omega_0 = 6$) on four representative datasets confirms that both wavelets detect significant periodicity with consistent sig95 values (maximum difference 6.4 percentage points) and dominant period estimates that agree within 8% for well-resolved peaks; apparent larger differences for broad spectral features reflect the Morlet wavelet’s superior frequency resolution rather than a disagreement about the underlying biology (Extended Data Fig. 12a). Notably, the Morlet estimate for MCF-7 chrX (30.9 Mbp) falls within the cross-wavelet coherence range (28–31 Mbp; Extended Data Fig. 2), suggesting the Morlet wavelet’s sharper frequency resolution may better resolve the true dominant period in this case. The CWT was computed via FFT convolution (T&C eq. 4). Eighty log-spaced scales were computed spanning periods of 10 to 7,000 peak-index units ($\delta j = 0.125$ octaves per scale), corresponding to approximately 0.11–76.7 Mbp on chrX at a median inter-peak spacing of 10,950 bp. The dominant period was defined as the scale at which the global wavelet spectrum (GWS; mean wavelet power outside the cone of influence, COI) is maximized. The COI was defined following T&C eq. 25 for the Paul wavelet. Pointwise significance was assessed against an AR1 red-noise null model (T&C eq. 18); the lag-1 autocorrelation coefficient was estimated from the normalised signal. The fraction of time-scale points outside the COI exceeding the AR1 95% significance threshold is reported as sig95. The AR1 model is used as a descriptive baseline for spectral concentration; it is not the primary inferential null (see Advanced null model testing). The signal was standardized to zero mean and unit variance prior to transformation.

Validation. One thousand realizations of Gaussian white noise ($N = 8,082$) yielded a mean sig95 of $4.6\% \pm 2.6\%$, confirming the nominal 5% false positive rate. A pure sine wave of period 500 peak-index units

549 embedded in Gaussian noise ($\text{SNR} = 1$) was recovered with 98.6% accuracy.

550 **Extended robustness.** Method-invariance across four wavelet families (Paul $m = 2/m = 4$, Morlet,
551 DOG), peak-calling sensitivity across five signal-value thresholds, and non-wavelet (FFT, ACF) cross-validation,
552 including consistency of the scaling-law exponent, are reported in Supplementary Methods (extended) and
553 summarised in Extended Data Fig. 12.

554 **Harmonic structure of the supra-compartment wave.** The dominant supra-compartment period
555 reported in the main text is the rank-1 peak of the global wavelet spectrum (GWS); the GWS curve in
556 fact carries multiple local maxima, several of which sit at near-integer ratios to the rank-1 scale and be-
557 have as harmonics of the same underlying periodic fold. A wavelet-/threshold-/period-range sweep on three
558 representative chromosomes (chr1, chr7, chr19; K562 ENCFF361VGY; Paul $m = 1-6$; signalValue thresholds
559 top25/top50/top75/top100; period range 4–14,000 peak indices) recovers, in addition to the rank-1 feature,
560 secondary GWS maxima at integer ratios of $3\times$, $4\times$, $5\times$, and $6\times$ the rank-1 period. On chr7 at the manuscript-
561 canonical Paul $m = 2$ setting, the rank-1 period is 28.83 Mbp and the rank-2 period is 6.18 Mbp (ratio $4.66\times$,
562 fifth harmonic), matching an anti-phase peak previously visible in Extended Data Fig. 10a. The rank-1 scale
563 is robust to wavelet family within $\pm 8\%$ for chr7 (Paul $m = 1-3$) and shifts toward smaller scales for higher-
564 order Paul wavelets and stricter peak thresholds, as expected when narrower frequency localization or sparser
565 peak density emphasizes higher-frequency components of the same broad-band periodic spectrum. The har-
566 monic structure is consistent with a non-pure sinusoidal alternation between A and B compartments along the
567 consecutive-peak axis (a square-wave-like pattern with rounded transitions decomposes into a fundamental plus
568 harmonics, with odd harmonics dominating in proportion to how square-wave-like the signal is). To quantify
569 harmonic parity we interpolated the GWS at the $3\times$, $4\times$, $5\times$, and $6\times$ sub-multiples of each chromosome's dom-
570 inant period T_1 on the manuscript-canonical 500 kb-binned ATAC-seq peak-count signal (the same signal used
571 for phase estimation), defined odd-harmonic power as the mean of GWS at $T_1/3$ and $T_1/5$ and even-harmonic
572 power as the mean of GWS at $T_1/4$ and $T_1/6$, and excluded any chromosome whose harmonic positions fell out-
573 side the cone of influence (chr21 excluded from the even-harmonic comparison). Consistent with a near-square
574 wave rather than a pure square wave, odd harmonics carried systematically greater power than even harmonics
575 in 21/21 autosomes with measurable even-harmonic power (Wilcoxon signed-rank $W = 0$, $p = 9.5 \times 10^{-7}$ two-
576 sided; median odd/even power ratio = 1.22; Supplementary Fig. 39). The dominance of odd harmonics agrees
577 with the early observation by one of us¹¹, who noted multiple consistent periodicities at higher cycle counts
578 per chromosome on consecutive-peak DNase data using AutoSignal in 2017. Per-chromosome multi-peak GWS
579 spectra and ratio statistics are reported in Supplementary Fig. 37; the harmonics are not used as independent
580 inferential channels in the main text and are reported here for descriptive completeness.

581 Data preparation

582 DNase-seq, ATAC-seq, and H3K4me3 ChIP-seq peaks were obtained from ENCODE in narrowPeak format. For
583 each chromosome, peaks were sorted by genomic start coordinate and the **signalValue** field (column 7) was used
584 as the analysis signal. ATAC-seq IDR-thresholded peaks containing coordinate-duplicate entries were resolved
585 by retaining the entry with the highest **signalValue**. A randomized control was generated by permuting the
586 **signalValue** scores across all chrX peaks while preserving genomic coordinates (seed = 42). For the CTCF
587 knockdown matched-control analysis, stratified subsampling was performed across 30 equal-probability strata
588 defined by the knockdown quantile distribution, yielding $N = 5,779$ matched control peaks (KS $D = 0.034$ after
589 matching vs. $D = 0.281$ before).

590 Monte Carlo permutation testing

591 One thousand Monte Carlo surrogate datasets were generated by randomly permuting the **signalValue** scores
592 across all chrX peaks (seed = 42, NumPy **default_rng**). Empirical p-values were computed using the Phipson-
593 Smyth correction²⁰: $p = (1 + \#\{\text{surrogate} \geq \text{observed}\}) / (N_{\text{surr}} + 1)$. Multiple testing correction across all 80
594 scales used the Benjamini-Hochberg (BH) FDR procedure²¹.

Phase classification and Hi-C compartment analysis

The instantaneous wavelet phase at each peak position was extracted from the complex CWT coefficients at the dominant period band (scales within $\pm 0.15 \log_{10}$ units of the dominant period). Peaks were classified as high-phase (local maxima within 95% AR1 significance contours) or low-phase (local minima) based on the sign and magnitude of the band-pass reconstructed signal relative to its standard deviation. Hi-C A/B compartment eigenvectors (PC1) were obtained from ENCODE MCF-7 intact Hi-C (ENCSR660LPJ; ENCFF139PQX; 5 kb resolution) and GM12878 (ENCSR916MFV; ENCFF565ARO; 5 kb resolution). Compartment A was assigned to positive PC1 values. Phase harmonization was performed by swapping high-phase and low-phase assignments for chromosomes with $\Delta\%A < 0$. Concordance was assessed by Fisher's exact test and Mann-Whitney U test.

Advanced null model testing

IAAFT surrogates. Iterative amplitude-adjusted Fourier transform (IAAFT) surrogates were generated following Schreiber and Schmitz⁵¹, preserving both the amplitude distribution and the power spectrum while randomizing phase relationships. Two hundred surrogates were generated for the initial MCF-7 chrX analysis (Section "Null models") (seed = 42, incremented per surrogate; convergence threshold $< 10^{-6}$ or 100 iterations). Spectral match quality was verified by computing the Kolmogorov-Smirnov (KS) distance between the surrogate and real power spectra for each surrogate; the median KS distance across 200 MCF-7 chrX surrogates was 0.031 ± 0.004 (mean \pm SD), confirming that surrogates achieve close spectral matching to the real signal. The sig95 comparison therefore tests for phase structure rather than spectral differences. Empirical p-values used the Phipson-Smyth correction; BH FDR correction was applied across all 23 chromosomes for the genome-wide analysis. A separate genome-wide IAAFT analysis with 1,000 surrogates per chromosome was conducted for the per-chromosome BH-corrected extension (Section "IAAFT with 1,000 surrogates").

Domain-shuffle surrogates. Contiguous A/B compartment domains on chrX were defined by runs of consecutive same-compartment peaks (1,241 domains; 621 A, 620 B). Two hundred surrogates were generated by randomly permuting domain order while preserving each domain's internal peak scores and size.

Block-bootstrap. The consecutive-peak signal was divided into non-overlapping blocks of length L (25 to 2,000 peaks), resampled with replacement (100 surrogates per block size). The critical block size L_{critical} was defined as the smallest L at which the surrogate sig95 distribution (mean + 1 SD) reached the real sig95 value.

Replication timing analysis

MCF-7 Repli-seq data were obtained from ENCODE (ENCSR188HJH; hg19; six S-phase fraction bigWig files). DNase-seq peak midpoints were lifted from GRCh38 to hg19 using pyliftover (99.8% success rate). A continuous RT score was computed as the weighted mean of the six fractions (positive = late-replicating), winsorized at the 1st and 99th percentiles per chromosome and standardized to zero mean and unit variance. GM12878 Repli-seq data were processed identically. Cross-wavelet coherence was computed following Torrence and Webster²² with Gaussian smoothing in time (width = $0.6 \times \text{scale}$) and boxcar smoothing in scale (width = $0.6/\delta j$).

RIF1 perturbation analysis

ICE-balanced Hi-C contact matrices at 100 kb resolution were obtained from GEO GSE160563 (Klein et al. 2021¹⁸): HCT116 RIF1-AID untreated control (CTL) and RIF1 knockout (KO). PC1 eigenvectors were computed using cooltools v0.5.4²³. The CWT was applied to the PC1 eigenvector on chr1–22 (chrX absent from KO dataset). Compartment switching was quantified as the fraction of 100 kb bins that changed PC1 sign between CTL and KO after sign harmonization. Wilcoxon signed-rank tests compared per-chromosome sig95 and dominant period between conditions.

Single-cell Repli-seq triangulation. Single-cell Repli-seq data from HAP1 wild-type ($n = 48$) and RIF1 knockout ($n = 66$) cells were obtained from GSE160563 (Klein et al. 2021¹⁸). For each 50 kb bin, the per-cell replicated fraction (sfrac) was computed as the proportion of S-phase cells with the bin in a replicated state.

T_{width} was defined per Klein et al. as the inter-quartile range (IQR) of sfrac at each bin position, providing a direct cell-to-cell variability readout of replication-front coherence. Per-bin ΔT_{width} was computed as KO minus WT. Bins with fewer than 5 replicating WT cells (890 bins genome-wide) were excluded; the resulting T_{width} fold-change is therefore a lower bound. Compartment switching status per bin was assigned from Hi-C PC1 sign change between WT and KO (stable A: PC1 > 0 in both; stable B: PC1 < 0 in both; A-to-B and B-to-A: sign flips). Partition-level contributions to total broadening were computed as $\sum_i n_i \cdot \Delta T_{\text{width},i}$, divided by genome-wide $\sum n \cdot \Delta T_{\text{width}}$, to weight by both bin count and per-bin effect size; this ΔT_{width} -weighted formulation avoids the regression-to-mean inflation that affects fold-change-based partition fractions. Genome-wide rank-biserial r was computed via the Mann-Whitney U statistic comparing WT and KO bin distributions. Wavelength-invariance was assessed by CWT (Paul $m = 2$) on $\log_2(\text{H3K27ac}/\text{H3K9me3})$ ChIP-seq tracks (WT G1-sorted from the AID system, KO unsorted CRISPR cells); the cell-cycle composition mismatch limits power and is reported as a caveat. Bulk Repli-seq variance, fraction-committed, and autocorrelation length are reported as proxies (Supplementary Fig. 13e); they are not labelled as sig95 because bulk Repli-seq $\log_2(\text{E}/\text{L})$ is a step-function signal with $1/f^2$ red-noise spectrum, not a quasi-sinusoidal signal class amenable to CWT period extraction.

Mitotic wave-abolishment AR(1) null

For the DT40 CDK1-as time course³³, the AR(1) null model used to compute sig95 was anchored to interphase by fixing the lag-1 autocorrelation coefficient α per chromosome to the mean of the two G2 replicates. This formulation poses the test as: does mitotic PC1 retain interphase-equivalent periodic structure? and prevents the per-stage α -refit that would otherwise partly compensate for any genuine loss of periodicity.

K562 phase map

All K562-phase-dependent analyses use Paul CWT carrier phase at the dominant period, extracted from ENCFF361VGY via the chromperiod pipeline (phase_map_k562_hg19_CORRECTED_v38.csv; hg38 equivalent expD_phase_map_k562_hg38_CORRECTED_v38.csv). Full phase-map extraction history, MCF-7/K562 comparison tables, circadian wavelength-invariance control, cPeaks scaling sensitivity, and entropy diagnostics are reported in Supplementary Note 6.

Cross-species data acquisition and analysis

Accessibility data: mouse heart DNase-seq (ENCSR000CBF, mm10, B6CASTF1/J); mouse heart Hi-C (ENCSR997TTD); *Drosophila* S2 ATAC-seq peaks (GSE222261, dm6) with signal from GSE186720 NT; *D.* Hi-C (GSE89112, Kc167). Yeast: *S. cerevisiae* nucleosome occupancy (GSE66386²⁴); *S. pombe* Hi-C (GSE56849²⁵). Chicken liver ATAC-seq (FAANG GSE158430, galGal6³¹); biological replicates M08 and M22 were pooled; only autosomes with ≥ 200 peaks and length ≥ 5 Mbp were retained (26/39). All non-human signal values were win-sorized at the 99th percentile, \log_{1p} -transformed, and z-scored; eigenvector sign was corrected per chromosome using gene density.

Scaling-law fit. Primary estimator: OLS of $\log_{10}(T)$ on $\log_{10}(L)$ across $n = 71$ chromosomes after exclusion of COI-limited chromosomes (period_frac ≥ 0.45) and low-peak chromosomes ($< 1,000$ peaks). Robustness: species-block bootstrap (10,000 resamples of species with replacement) gives $b = 0.79$ [95% CI: 0.46, 1.17], the most conservative interval; a 4-group linear mixed-effects model (species random intercept), Tobit censored regression, and a no-filter sensitivity run are tabulated in Supplementary Methods (extended). The circular-linear correlation for the TSA-seq analysis was computed using the Jammalamadaka-Sengupta statistic²⁶ with 95% CI by chromosome-block bootstrap ($n = 5,000$ replicates).

Differentiation downsampling control

For each H7 differentiation time point (Day 2, Day 5, Day 9, Day 14; ENCODE ENCSR167QXA), 100 random subsamples (seeds 0–99) of the Day 0 chrX peak set ($N = 21,422$ peaks) were drawn without replacement to match the target peak count and subjected to the full CWT pipeline. The actual dominant period at each time point was compared to this null distribution by z-score and empirical one-tailed p-value.

TSA-seq nuclear position analysis

K562 DNase-seq peaks were obtained from ENCODE (ENCFF361VGY; GRCh38; 176,582 peaks). The CWT was applied to all 23 chromosomes using the Paul wavelet ($m = 2$, 80 scales). Instantaneous phase at the dominant period scale was extracted from the complex CWT coefficients via $\varphi = \arctan 2(\text{Im}(W), \text{Re}(W))$, where W is the complex wavelet coefficient computed by FFT convolution following T&C eq. 4. The Paul wavelet convention places $\varphi = 0^\circ$ at signal crests and $\varphi = \pm 180^\circ$ at troughs, verified analytically on a pure cosine test signal. Phase values were averaged circularly within 100 kb genomic bins.

SON TSA-seq v2 (4DN 4DNFINI7KVAI; Zhang et al. 2021¹³; protocol family Chen et al. 2018¹²) and LMNB1 TSA-seq v2 (4DN 4DNFIHB5C2FC and 4DNFIXC534XS; Gholamalamdari et al. 2025¹⁴) bigWig files were binned at 100 kb by mean signal. LMNB1 replicates were averaged after confirming high reproducibility ($r = 0.993$). The nuclear axis score was defined as SON – LMNB1 per bin. Quality filters required $\geq 50\%$ of peaks in each bin to be within the AR1 95% significance region and $< 50\%$ within the COI, and the chromosome dominant period to be 5–80 Mbp; 11,249 bins across 18 chromosomes were retained.

Circular-linear correlation was computed using the Jammalamadaka-Sengupta statistic²⁶. Statistical significance was assessed by chromosome-level block permutation ($n = 5,000$), which shuffles chromosome-phase assignments while preserving within-chromosome spatial autocorrelation. Phase-octant means were computed in eight 45° bins and fitted by a sinusoid $A \cos(\varphi - \varphi_0) + C$ with free amplitude, phase offset, and baseline. A-crest ($|\varphi| \leq 45^\circ$) versus B-trough ($|\varphi| \geq 135^\circ$) comparisons used the Mann-Whitney U test (one-sided).

Interchromosomal phase-matching analysis

Interchromosomal phase-matching analysis. The CWT instantaneous phase at the dominant period was mapped onto 500 kb genomic bins for all autosomes using GM12878 DNase-seq (ENCFF762CRQ). Interchromosomal Hi-C contact matrices were extracted at 500 kb resolution (KR normalisation) from Rao et al. (2014) using hic-straw. For each chromosome pair, bin-pair contacts were stratified by absolute phase difference $\Delta\varphi$ into eight equal bins from 0 to π , restricted to A-compartment bin pairs (both bins with mean DNase signal above the chromosomal median). Observed/expected ratios were computed from marginal contact rates to remove positional bias. The cosine model $O/E = a + b \cos(\Delta\varphi)$ was fitted per pair; the amplitude $b > 0$ indicates phase-matching enrichment. Significance was assessed by one-sample t -test, Wilcoxon signed-rank test, and permutation of phase labels ($N = 500$). The analysis was repeated for HCT116 wild-type and RIF1 knockout Hi-C (Klein et al. 2021; GSE160563) with PC1 eigenvectors as the CWT input signal.

Single-cell Dip-C phase-matching

Dip-C interchromosomal contact pairs were analysed in two cohorts with a shared pipeline. *Human*. 16 GM12878 cells¹⁵ (GSE117874 and GSE117109 .clean.con.txt.gz); A/B identity was assigned from the Rao et al. 2014 subcompartment map to eliminate circularity with the CWT phase map. *Mouse cortex*. Stratified random sample (seed 20260419) of 240 visual-cortex neurons from Tan et al. 2021 (GSE164203¹⁶) balanced across age (P7, P14, P21, P28) and condition (control, dark-reared); a 60-cell P1 secondary cohort was drawn from remaining cells. A mm10 CWT phase map was generated from motor-neuron DNase-seq peaks via the same chromperiod Paul ($m = 2$) pipeline; an mESC-phase-map sensitivity run is reported alongside. For every cell, each contact locus was assigned the CWT phase of the nearest 500-kb bin. Absolute phase differences $|\Delta\varphi|$ were binned into $K = 8$ equal-width bins over $[0, \pi]$ and compared against a flat null ($E_k = N/K$, matching the

Tan 2018 GM12878 reference); the cosine model $O/E = 1 + b \cos(|\Delta\varphi|)$ was fitted by nonlinear least squares per cell, with per-cell uncertainty from contact-level bootstrap (500 resamples). Cohort-level significance used one-sample t -test, Wilcoxon signed-rank, and exact binomial sign test against $b = 0$. A GM12878 17-cell gate ($b = +0.060 \pm 0.025$; 15/15 reproducible cells positive; median $R^2 = 0.91$) was passed before the cortex analysis; cohort- and stratum-level results are in Supplementary Fig. 21.

Phase-conditioned 3D trajectory analysis (Supplementary Fig. 28). Per-cell three-dimensional positions from published Dip-C .3dg structures (GSE117874 GM12878 14 cells; GSE164203 mouse visual cortex 28 P56 cells) were annotated with CWT phase from the matched-species phase map (GM12878 hg19 100-kb bins; mouse motor-neuron mm10 500-kb bins). For each cell a speckle–lamina axis was derived by phase regression of the three-dimensional bead positions on $\cos(\varphi)$; cells were aligned so the axis defines \hat{z} with the speckle pole at $+z$, and the per-bead position was projected into cylindrical coordinates (r, θ, z) . Sign convention was verified against the K562 TSA-seq ground truth ($\rho(\cos \varphi, \text{SON}) = +0.435$, $\rho(\cos \varphi, \text{LMNB1}) = -0.372$). Three geometric models were fit per chromosome–haplotype pair on phase-binned profiles ($n = 16$ phase bins per pair): four-parameter sinusoidal radial oscillation ($r(\varphi) = r_0 + A \sin(2\pi\varphi/T + \phi_0)$); six-parameter slinky (z sinusoidal in φ with linear drift); six-parameter helix (θ linear in φ with circular-linear correlation r_{cl} , Mardia & Jupp 2000). AIC was computed against a two-parameter null. Per-bead Spearman ρ was used as a confirmatory secondary metric only; the primary metric is per-cell binned sinusoidal R^2 (binning averages over the well-known Dip-C reconstruction noise floor at 250-kb-equivalent per-bead positional uncertainty). Mouse cortex amplitude sign-inversion is flagged as ambiguous pending a cortex-specific Hi-C-derived phase map.

Secondary imaging and genotype–phenotype methods

Extended protocols for MERFISH (Su et al. 2020), PCAWG mutation density, in-silico helix vs. radial models and Dip-C allelic asymmetry, seqFISH+ (Takei et al. 2021), Hoencamp condensin/cohesin phase coherence, cancer-line and expression surveys, translocations, speckle stratification, retroviral integration, condensability, and ENCODE CTCF/cohesin/PRC1 depletion tracks appear under **Supplementary Methods (extended)** in the Supplementary Information PDF.

Public-release verification of the translocation phase-matching analysis. The headline cosine number was independently recomputed from the publicly distributed ICGC PCAWG consensus 1.6 SV bedpe set (`final_consensus_sv_bedpe_passonly.icgc.public.tar`; 1,926 aliquots distributed). Filtering to inter-chromosomal autosomal TRAs ($\text{chrom}_1 \neq \text{chrom}_2$, both breakpoints in $\{1, \dots, 22\}$) yields 35,975 pairs across 1,487 aliquots; mapping each breakpoint to the v38 K562 hg19 phase map gives mean $\cos(\Delta\varphi) = +0.064$ (cluster-robust SE = 0.0076 with aliquot UUID as the cluster, $t = 8.46$, $p < 10^{-15}$). A chromosome-composition-controlled permutation null places the observed value at $z = 6.95\sigma$ above the null mean ($p < 1/5,001$ at 5,000 permutations); an aliquot-level bootstrap gives a 95% percentile CI $[+0.049, +0.079]$ excluding zero. Individual breakpoint phases are non-uniformly distributed (Pearson $\chi^2_{23} = 1,033$, $p \ll 10^{-100}$; $1.07\times$ A-side enrichment, $0.72\times$ B-trough depletion; Supplementary Fig. 31). Cancer-type stratification across the 23 cohorts with ≥ 5 aliquots reproduces the wave-aligned signal in 19/20 solid-tumour projects (median $+0.061$, mean $+0.066$; 8/20 individually significant), but separates haematological cancers as a distinct biology: B-cell lymphoma (MALY-DE; $\hat{c} = -0.068$, 95% CI $[-0.166, -0.002]$) and acute myeloid leukaemia (LAML-KR; $\hat{c} = -0.51$, $n = 14$ pairs) show negative mean cosine, while chronic lymphocytic leukaemia is near zero (Supplementary Fig. 32). Mechanistically, solid-tumour translocations arise from DNA-damage-coupled illegitimate joining of physically proximal loci that respects the wave geometry, whereas haematological-cancer translocations are dominated by lineage-programmed V(D)J / AID recombination that selects breakpoints by sequence rather than by three-dimensional position.

Patient-level axes and underpowered RIF1 replication. Two within-cohort stratifications locate the wave-translocation coupling further. (i) Saturation: ranking aliquots by TRA-pair burden, the wave-aligned signal is absent at ≤ 5 pairs, emerges between 5 and 10 pairs (mean $\cos = +0.064$, 95% CI $[+0.021, +0.110]$), and saturates at $+0.06$ – $+0.07$ from ≥ 10 pairs through ≥ 160 pairs (Spearman $\rho = +0.081$, $p = 1.7 \times 10^{-3}$ across

all 1,487 aliquots): the wave acts as a geometric ceiling, not a progressive loading. (ii) Driver-mutation modulation: across the top 20 PCAWG drivers, four have a 95% bootstrap CI on $\Delta \cos$ excluding zero; *CDKN2A* loss strengthens the coupling ($\Delta \cos = +0.049$, $n = 319$), *KMT2D* (-0.082 , $n = 48$), *ERG* (-0.069 , $n = 99$), and *PTEN* (-0.037 , $n = 146$) loss weakens it; *TP53* status is null ($\Delta \cos = -0.010$, $n = 582$) (Supplementary Fig. 33). The patient-distance test of the RIF1 axis (matched per-aliquot RNA-Seq from the PCAWG transcriptome release⁵²; $n = 366$ matched solid-tumour aliquots, of pre-committed $n \geq 600$) is underpowered: the four-cohort pooled correlation of $\log(\text{RIF1 FPKM} + 1)$ with mean $\cos(\Delta\varphi)$ is null (DerSimonian–Laird random-effects $\rho = +0.057$, 95% CI $[-0.076, +0.188]$), and the 16-gene replication-timing pathway score is directionally consistent but boundary-significant ($\rho = +0.113$, 95% CI $[-0.020, +0.241]$, $p = 0.096$; Supplementary Fig. 34). The structural cause is that the ICGC open-access RNA-Seq tier covers only 7/25 project codes in the SV-bearing WGS set; the largest SV cohorts (LIRI-JP, PACA-CA, PRAD-CA, PBCA-DE) lack public RNA-Seq. An orthogonal coding-mutation MAF test on the same 1,484 aliquots was equally null (pooled rank-biserial $r = +0.008$, 95% CI $[-0.165, +0.182]$, $k = 5$ cohorts), constrained by the 5.5% pathway-mutation prevalence. An independent-cohort TCGA replication aborted at the data-acquisition step; TCGA WGS SV BEDPE files require GDC controlled access (the Hadi 2020 *Cell* consensus Synapse deposit returns HTTP 404; cBioPortal’s TCGA SVs are RNA-seq fusion calls, invalid for $\cos(\Delta\varphi)$ at base-pair resolution). A pre-committed two-tailed driver-vs-passenger SV stratification (Li 2020 SV-driver compendium and a curated 14-gene canonical haematological-driver panel; primary endpoint majority verdict across A–A / A–B / B–B compartment strata) returned Outcome C overall, but the B–B stratum reached significance with the canonical haematological drivers (TAL1, KMT2A, BCL2, MECOM, LMO2, RARA) showing systematic anti-phase enrichment ($f_{\text{AP}} = 0.479$ vs 0.274 for passenger B–B pairs at $\cos(\Delta\varphi) < -0.5$; Fisher $p = 0.003$; $\Delta \cos = -0.318$, MW $p = 0.002$, $n_{\text{DP}} = 48$), generalising the BCL2 $t(14;18)$ pattern across the canonical haematological-translocation panel and consistent with V(D)J / AID recombination targeting sequence rather than wave geometry. Within-cancer-type B-cell lymphoma replication-timing-pathway correlation ($\rho = +0.390$, $p = 1.6 \times 10^{-4}$ on Lymph-BNHL $n = 89$) is reported as an exploratory observation pending mechanistic interpretation. The cell-line RIF1-KO evidence (Fig. 10) and the cancer-genomic stratifications above remain the primary patient-distance tests; controlled-access replication on the ICGC restricted RNA-Seq tier and on Hartwig metastatic WGS data is the named revision-cycle priority.

Mitotic wave abolishment analysis

The consecutive-peak CWT pipeline (`chromperiod`, Paul $m = 2$; period bounds 8–200 bins, 80 log-spaced scales) was applied to Hi-C PC1 eigenvectors from the DT40 CDK1-as mitotic time course of Gibcus *et al.* 2018 (GSE102740³³). Raw 10 kb `.cool` matrices were coarsened to 250 kb, ICE-balanced (`cooler balance`), and PC1 computed with `cooltools.eigs_cis` using per-bin coverage as the phasing reference. Because mitotic PC1 has near-unit-root autocorrelation, the AR(1) null α was anchored per chromosome to the mean of the two G2 replicates and reused across all mitotic stages; this reframes the test as “does mitotic PC1 retain interphase-equivalent periodicity?” (derivation in Supplementary Note). As a co-primary interphase control the pipeline was applied identically to GM12878 Hi-C (Rao *et al.* 2014; GSE63525²). Hi-C eigenvector sign ambiguity was handled by reporting the Pearson correlation matrix of PC1 across stages in $|r|$ form (Supplementary Fig. 14). A K562 nocodazole-arrest control (Naumova 2013 vs. Rao 2014 asynchronous; $\sim 85\%$ mitotic purity; mean sig95 drop 26%) is reported as a partial-abolishment methodological control in Supplementary Fig. 15.

Secondary scaling and contactomics benchmarks

Block-copolymer null simulations, A/B domain-size power-law fitting, and SPRITE hub reanalysis are under **Supplementary Methods (extended)** in the Supplementary Information PDF.

814 CNV breakpoint phase analysis

815 Pathogenic CNVs were extracted from the ClinVar `variant_summary.txt` (May 2026 release) filtered for
816 `ClinicalSignificance` \in {Pathogenic, Likely pathogenic, Pathogenic-low penetrance}, GRCh38 assembly, au-
817 toosomes plus chrX, and length 50 kb–10 Mb ($n = 4,900$ CNVs; types: Deletion, Duplication, copy number
818 gain, copy number loss). Each breakpoint (start, stop) was mapped to its 500-kb K562 v38 hg38 phase-
819 map bin and the $\cos(\varphi)$ value extracted. Cross-cell-line analysis used v38-pipeline phase maps generated
820 by the canonical `chromperiod` consecutive-peak Paul $m = 2$ pipeline (identical pipeline parameters to the
821 manuscript primary K562 phase map) for K562 (ENCFF361VGY), GM12878 (ENCFF598KWZ), HCT116
822 (ENCFF903FUJ), MCF-7 (ENCFF611NKL), and IMR-90 (ENCFF530ISG). Cross-catalog validation used
823 gnomAD-SV v4.1 (filtered PASS, 50 kb–10 Mb, autosomes plus chrX). Cross-species replication used the En-
824sembl mouse Structural Variations VCF (DGVa-derived; release 111; mouse ESC mm10 phase map). Repli-seq
825 stratification used K562 ENCFF000KUR (lifted hg19 \rightarrow hg38 via UCSC chain); per-bin partial Spearman
826 $\rho(\text{breakpoint count}, \cos(\varphi)|\text{repliseq})$ was computed via residualization. Segmental-duplication density used
827 UCSC `genomicSuperDups` hg38 (filtered ≥ 1 kb), with NAHR-relevant SD pairs defined as intra-chromosomal
828 pairs 200 kb–3 Mb apart. Statistical tests: Kolmogorov–Smirnov two-sample for breakpoint \cos distribution
829 comparisons; Spearman ρ for per-bin correlations; partial Spearman ρ controlling for Repli-seq signal and SD
830 count via residualization; Mann–Whitney U for distribution shifts. The 11 canonical recurrent CNV syndromes
831 were stratified by mechanism (NAHR-mediated / imprinting-driven / non-recurrent terminal deletion) for the
832 per-syndrome phase position analysis (Supplementary Table 1).

833 Statistical analysis

834 All statistical tests are two-sided unless otherwise stated. Multiple testing correction used the Benjamini-
835 Hochberg FDR procedure. Permutation p-values were computed using the Phipson-Smyth correction to prevent
836 $p = 0$. Spearman rank correlations were used for non-parametric associations. Wilcoxon signed-rank tests were
837 used for paired comparisons. All analyses were performed in Python 3.10 using NumPy, SciPy, pandas, and
838 statsmodels.

839 **Reproducibility.** All analyses were performed using publicly available data and open-source software. A
840 complete reproduction script is provided in the `chromperiod` repository ([https://github.com/wolfgebhardt/](https://github.com/wolfgebhardt/chromperiod)
841 [chromperiod](https://github.com/wolfgebhardt/chromperiod)).

842 Data availability

843 All datasets analysed in this study are publicly available. ENCODE data were obtained from [https://www.](https://www.encodeproject.org)
844 [encodeproject.org](https://www.encodeproject.org); GEO data from <https://www.ncbi.nlm.nih.gov/geo/>; 4D Nucleome data from [https:](https://data.4dnucleome.org)
845 [/data.4dnucleome.org](https://data.4dnucleome.org). Full accession numbers are provided in Supplementary Table S1.

846 Code availability

847 The `chromperiod` Python package implementing all CWT analyses is available at [https://github.com/](https://github.com/wolfgebhardt/chromperiod)
848 [wolfgebhardt/chromperiod](https://github.com/wolfgebhardt/chromperiod). A step-by-step reproduction script and all analysis notebooks are included in
849 the repository.

850 Use of AI tools

851 Manuscript preparation was assisted by *Claude* (Anthropic; Sonnet-class models via Claude Desktop, 2025–2026
852 sessions; specific build identifiers were not logged and will be archived going forward) for L^AT_EX editing, statis-

853 tical cross-checking, and figure assembly. Literature screening was assisted by *Elicit* (<https://elicit.com>).
854 Computational analyses were executed through *BIOMNI*. The author reviewed all tool-assisted outputs and
855 takes full responsibility for the accuracy, integrity, and originality of the published work; scientific hypotheses,
856 analytical design, and interpretation are the author's own.

857 Author contributions

858 W.H.G. conceived the study, designed and performed all analyses, and wrote the manuscript.

859 Competing interests

860 The author declares no competing interests.

861 Acknowledgements

862 No external funding was received. This work used publicly available data from the ENCODE Consortium,
863 PCAWG, and 4D Nucleome projects.

864 Additional information

865 Supplementary information is available for this paper. Correspondence and requests for materials should be
866 addressed to W.H.G. (w.gebhardt@protonmail.com).

867 References

- 868 [1] Lieberman-Aiden, E., et al. (2009). Comprehensive mapping of long-range interactions reveals folding
869 principles of the human genome. *Science*, 326(5950), 289–293.
- 870 [2] Rao, S. S. P., et al. (2014). A 3D map of the human genome at kilobase resolution reveals principles of
871 chromatin looping. *Cell*, 159(7), 1665–1680.
- 872 [3] Dixon, J. R., et al. (2012). Topological domains in mammalian genomes identified by analysis of chromatin
873 interactions. *Nature*, 485(7398), 376–380. <https://doi.org/10.1038/nature11082>
- 874 [4] Bonev, B., & Cavalli, G. (2016). Organization and function of the 3D genome. *Nature Reviews Genetics*,
875 17(11), 661–678. <https://doi.org/10.1038/nrg.2016.112>
- 876 [5] Arneodo, A., Bacry, E., Graves, P. V., & Muzy, J. F. (1995). Characterizing long-range correlations in
877 DNA sequences from wavelet analysis. *Physical Review Letters*, 74(16), 3293–3296.
- 878 [6] Audit, B., Thermes, C., Vaillant, C., d'Aubenton-Carafa, Y., Muzy, J. F., & Arneodo, A. (2001). Long-
879 range correlations in genomic DNA: a signature of the nucleosomal structure. *Physical Review Letters*,
880 86(11), 2471–2474.
- 881 [7] Audit, B., et al. (2009). Open chromatin encoded in DNA sequence is the signature of “master” replication
882 origins in human cells. *Nucleic Acids Research*, 37(18), 6064–6075.
- 883 [8] Audit, B., et al. (2013). Multiscale analysis of genome-wide replication timing profiles using a wavelet-based
884 signal-processing algorithm. *Nature Protocols*, 8(1), 98–110. <https://doi.org/10.1038/nprot.2012.145>
- 885 [9] Vaillant, C., Audit, B., & Arneodo, A. (2007). Experiments confirm the influence of genome long-range
886 correlations on nucleosome positioning. *Physical Review Letters*, 99(21), 218103.

- 887 [10] Pellow, R., & Comeron, J. M. (2026). A wavelet-based approach generates quantitative, scale-free and
888 hierarchical descriptions of 3D genome structures and new biological insights. *PLOS Computational Biology*,
889 22(1), e1013887. <https://doi.org/10.1371/journal.pcbi.1013887>
- 890 [11] Gebhardt, W. H. (2017). Wavelet analysis of consecutive DNase hypersensitivity peaks reveals an approxi-
891 mate periodic fold of chromatin accessibility on MCF-7 chromosome X, with multiple consistent periodicities
892 at higher cycle counts per chromosome detected by AutoSignal. Unpublished manuscript, IMB/EMBL
893 Mainz.
- 894 [12] Chen, Y., Zhang, Y., Wang, Y., Zhang, L., Brinkman, E. K., Adam, S. A., Goldman, R., van Steensel, B.,
895 Ma, J., & Belmont, A. S. (2018). Mapping 3D genome organisation relative to nuclear compartments using
896 TSA-Seq as a cytological ruler. *Journal of Cell Biology*, 217(11), 4025–4048. [https://doi.org/10.1083/](https://doi.org/10.1083/jcb.201807108)
897 [jcb.201807108](https://doi.org/10.1083/jcb.201807108)
- 898 [13] Zhang, L., Zhang, Y., Chen, Y., Gholamalamdari, O., Wang, Y., Ma, J., & Belmont, A. S. (2021). TSA-seq
899 reveals a largely conserved genome organisation relative to nuclear speckles with small position changes
900 tightly correlated with gene expression changes. *Genome Research*, 31(2), 251–264. [https://doi.org/10.](https://doi.org/10.1101/gr.266239.120)
901 [1101/gr.266239.120](https://doi.org/10.1101/gr.266239.120)
- 902 [14] Gholamalamdari, O., van Schaik, T., Wang, Y., Kumar, P., Zhang, L., Zhang, Y., Hernandez Gonzalez,
903 G. A., Vouzas, A. E., Zhao, P. A., Gilbert, D. M., Ma, J., & Belmont, A. S. (2025). Major nuclear locales
904 define nuclear genome organisation and function beyond A and B compartments. *eLife*, 13, RP99116.
905 <https://doi.org/10.7554/eLife.99116>
- 906 [15] Tan, L., Xing, D., Chang, C. H., Li, H., & Xie, X. S. (2018). Three-dimensional genome structures of single
907 diploid human cells. *Science*, 361(6405), 924–928.
- 908 [16] Tan, L., Ma, W., Wu, H., Zheng, Y., Xing, D., Chen, R., Li, X., Daley, N., Deisseroth, K., & Xie, X. S.
909 (2021). Changes in genome architecture and transcriptional dynamics progress independently of sensory
910 experience during post-natal brain development. *Cell*, 184(3), 741–758. [https://doi.org/10.1016/j.](https://doi.org/10.1016/j.cell.2020.12.032)
911 [cell.2020.12.032](https://doi.org/10.1016/j.cell.2020.12.032)
- 912 [17] Takei, Y., et al. (2021). Integrated spatial genomics reveals global architecture of single nuclei. *Nature*,
913 590(7845), 344–350. <https://doi.org/10.1038/s41586-020-03126-2>
- 914 [18] Klein, K. N., et al. (2021). Replication timing maintains the global epigenetic state in human cells. *Science*,
915 372(6540), 371–378.
- 916 [19] Torrence, C., & Compo, G. P. (1998). A practical guide to wavelet analysis. *Bulletin of the American*
917 *Meteorological Society*, 79(1), 61–78.
- 918 [20] Phipson, B., & Smyth, G. K. (2010). Permutation P-values should never be zero: calculating exact P-values
919 when permutations are randomly drawn. *Statistical Applications in Genetics and Molecular Biology*, 9(1),
920 Article 39.
- 921 [21] Benjamini, Y., & Hochberg, Y. (1995). Controlling the false discovery rate: a practical and powerful
922 approach to multiple testing. *Journal of the Royal Statistical Society: Series B*, 57(1), 289–300.
- 923 [22] Torrence, C., & Webster, P. J. (1999). Interdecadal changes in the ENSO-monsoon system. *Journal of*
924 *Climate*, 12(8), 2679–2690.
- 925 [23] Abdennur, N., & Mirny, L. A. (2020). Cooler: scalable storage for Hi-C data and other genomically labelled
926 arrays. *Bioinformatics*, 36(1), 311–316.
- 927 [24] Schep, A. N., et al. (2015). Structured nucleosome fingerprints enable high-resolution mapping of chromatin
928 architecture within regulatory regions. *Genome Research*, 25(11), 1580–1589.

- [25] Mizuguchi, T., et al. (2014). Cohesin-dependent globules and heterochromatin shape 3D genome architecture in *S. pombe*. *Nature*, 516(7531), 432–435.
- [26] Jammalamadaka, S. R., & SenGupta, A. (2001). *Topics in Circular Statistics* (Series on Multivariate Analysis, Vol. 5). World Scientific, Singapore. ISBN: 978-981-02-3778-3.
- [27] King, H.W., Fursova, N.A., Blackledge, N.P. & Klose, R.J. (2018). Polycomb repressive complex 1 shapes the nucleosome landscape but not accessibility at target genes. *Genome Research*, 28(10), 1494–1507. <https://doi.org/10.1101/gr.237180.118>
- [28] Clauset, A., Shalizi, C.R. & Newman, M.E.J. (2009). Power-law distributions in empirical data. *SIAM Review*, 51(4), 661–703. <https://doi.org/10.1137/070710111>
- [29] Alstott, J., Bullmore, E. & Plenz, D. (2014). powerlaw: A Python package for analysis of heavy-tailed distributions. *PLoS ONE*, 9(1), e85777. <https://doi.org/10.1371/journal.pone.0085777>
- [30] Park, S., et al. (2025). Native nucleosomes intrinsically encode genome organization principles. *Nature*, 643(8071), 572–581. <https://doi.org/10.1038/s41586-025-08971-7>
- [31] Kern, C., et al. (2021). Functional annotations of three domestic animal genomes provide vital resources for comparative and agricultural research. *Nature Communications*, 12, 1821. <https://doi.org/10.1038/s41467-021-22100-8>
- [32] Quinodoz, S. A., et al. (2018). Higher-order inter-chromosomal hubs shape 3D genome organization in the nucleus. *Cell*, 174(3), 744–757. <https://doi.org/10.1016/j.cell.2018.05.024>
- [33] Gibcus, J. H., et al. (2018). A pathway for mitotic chromosome formation. *Science*, 359(6376), eaao6135. <https://doi.org/10.1126/science.aao6135>
- [34] Naumova, N., et al. (2013). Organization of the mitotic chromosome. *Science*, 342(6161), 948–953. <https://doi.org/10.1126/science.1236083>
- [35] Teves, S. S., An, L., Hansen, A. S., Xie, L., Darzacq, X., and Tjian, R. (2016). A dynamic mode of mitotic bookmarking by transcription factors. *eLife*, 5, e22280. <https://doi.org/10.7554/eLife.22280>
- [36] Abramo, K., Valton, A.-L., Venev, S. V., Ozadam, H., Fox, A. N., and Dekker, J. (2019). A chromosome folding intermediate at the condensin-to-cohesin transition during telophase. *Nature Cell Biology*, 21(11), 1393–1402. <https://doi.org/10.1038/s41556-019-0406-2>
- [37] Corces, M. R., Granja, J. M., Shams, S., Louie, B. H., et al. (2018). The chromatin accessibility landscape of primary human cancers. *Science*, 362(6413), eaav1898. <https://doi.org/10.1126/science.aav1898>
- [38] Crane, E., Bian, Q., McCord, R. P., Lajoie, B. R., Wheeler, B. S., Ralston, E. J., Uzawa, S., Dekker, J., and Meyer, B. J. (2015). Condensin-driven remodelling of X chromosome topology during dosage compensation. *Nature*, 523(7559), 240–244. <https://doi.org/10.1038/nature14450>
- [39] Daugherty, A. C., Yeo, R. W., Buenrostro, J. D., Greenleaf, W. J., Kundaje, A., and Brunet, A. (2017). Chromatin accessibility dynamics reveal novel functional enhancers in *C. elegans*. *Genome Research*, 27(12), 2096–2107. <https://doi.org/10.1101/gr.226233.117>
- [40] Hughes, A. E. O., Enright, J. M., Myers, C. A., Shen, S. Q., & Corbo, J. C. (2017). Cell type-specific epigenomic analysis reveals a uniquely closed chromatin architecture in mouse rod photoreceptors. *Scientific Reports*, 7, 43184. <https://doi.org/10.1038/srep43184>
- [41] Solovei, I., Kreysing, M., Lanctôt, C., Kösem, S., Peichl, L., Cremer, T., Guck, J., & Joffe, B. (2009). Nuclear architecture of rod photoreceptor cells adapts to vision in mammalian evolution. *Cell*, 137(2), 356–368. <https://doi.org/10.1016/j.cell.2009.01.052>

- [42] Falk, M., Feodorova, Y., Naumova, N., Imakaev, M., Lajoie, B. R., Leonhardt, H., Joffe, B., Dekker, J., Fudenberg, G., Solovei, I., & Mirny, L. A. (2019). Heterochromatin drives compartmentalization of inverted and conventional nuclei. *Nature*, 570(7761), 395–399. <https://doi.org/10.1038/s41586-019-1275-3>
- [43] Boettiger, A. N., Bintu, B., Moffitt, J. R., Wang, S., Beliveau, B. J., Fudenberg, G., Imakaev, M., Mirny, L. A., Wu, C.-t., & Zhuang, X. (2016). Super-resolution imaging reveals distinct chromatin folding for different epigenetic states. *Nature*, 529(7586), 418–422. <https://doi.org/10.1038/nature16496>
- [44] Miron, E., Oldenkamp, R., Brown, J. M., Pinto, D. M. S., Xu, C. S., Faria, A. R., Shaban, H. A., Rhodes, J. D. P., Innocent, C., de Ornellas, S., Hess, H. F., Buckle, V., & Schermelleh, L. (2020). Chromatin arranges in chains of mesoscale domains with nanoscale functional topography independent of cohesin. *Science Advances*, 6(39), eaba8811. <https://doi.org/10.1126/sciadv.aba8811>
- [45] Prakash, K., Fournier, D., Redl, S., Best, G., Borsos, M., Tiwari, V. K., Tachibana-Konwalski, K., Ketting, R. F., Parekh, S. H., Cremer, C., & Birk, U. J. (2015). Superresolution imaging reveals structurally distinct periodic patterns of chromatin along pachytene chromosomes. *Proceedings of the National Academy of Sciences USA*, 112(47), 14635–14640. <https://doi.org/10.1073/pnas.1516928112>
- [46] Cremer, M., Brandstetter, K., Maiser, A., Rao, S. S. P., Schmid, V. J., Guirao-Ortiz, M., Mitra, N., Mamberti, S., Klein, K. N., Gilbert, D. M., Leonhardt, H., Cardoso, M. C., Lieberman Aiden, E., Harz, H., & Cremer, T. (2020). Cohesin depleted cells rebuild functional nuclear compartments after endomitosis. *Nature Communications*, 11, 6146. <https://doi.org/10.1038/s41467-020-19876-6>
- [47] Cremer, T., Cremer, M., Hübner, B., Strickfaden, H., Smeets, D., Popken, J., Sterr, M., Markaki, Y., Rippe, K., & Cremer, C. (2017). The interchromatin compartment participates in the structural and functional organization of the cell nucleus: ANC–INC model and dynamic 3D landscapes of chromatin domain clusters. *BioEssays*, 39(7), 1700083; and: Initial high-resolution microscopic mapping of active and inactive regulatory sequences proves non-random 3D arrangements in chromatin domain clusters. *Epigenetics & Chromatin*, 10:39. <https://doi.org/10.1186/s13072-017-0146-0>
- [48] Mirny, L. A. (2011). The fractal globule as a model of chromatin architecture in the cell. *Chromosome Research*, 19(1), 37–51. <https://doi.org/10.1007/s10577-010-9177-0>
- [49] Mahy, N. L., Perry, P. E., & Bickmore, W. A. (2002). Gene density and transcription influence the localization of chromatin outside of chromosome territories detectable by FISH. *Journal of Cell Biology*, 159(5), 753–763. <https://doi.org/10.1083/jcb.200207115>
- [50] Guelen, L., Pagie, L., Brasset, E., Meuleman, W., Faza, M. B., Talhout, W., Eussen, B. H., de Klein, A., Wessels, L., de Laat, W., & van Steensel, B. (2008). Domain organization of human chromosomes revealed by mapping of nuclear lamina interactions. *Nature*, 453(7197), 948–951. <https://doi.org/10.1038/nature06947>
- [51] Schreiber, T., & Schmitz, A. (2000). Surrogate time series. *Physica D*, 142(3–4), 346–382. [https://doi.org/10.1016/S0167-2789\(00\)00043-9](https://doi.org/10.1016/S0167-2789(00)00043-9)
- [52] The ICGC/TCGA Pan-Cancer Analysis of Whole Genomes Consortium (Campbell, P. J., *et al.*) (2020). Pan-cancer analysis of whole genomes. *Nature*, 578(7793), 82–93. <https://doi.org/10.1038/s41586-020-1969-6>
- [53] Li, Y., Roberts, N. D., Wala, J. A., Shapira, O., *et al.*, Imielinski, M., PCAWG SV Working Group, Weischenfeldt, J., Beroukhim, R., Campbell, P. J. (2020). Patterns of somatic structural variation in human cancer genomes. *Nature*, 578(7793), 112–121. <https://doi.org/10.1038/s41586-019-1913-9>

- 1011 [54] Sidiropoulos, N., Mardin, B. R., Rodríguez-González, F. G., Bochkov, I. D., Garg, S., Stütz, A. M.,
1012 Korb, J. O., Aiden, E. L., Weischenfeldt, J. (2022). Somatic structural variant formation is guided by
1013 and influences genome architecture. *Genome Research*, 32(4), 643–655. [https://doi.org/10.1101/gr.](https://doi.org/10.1101/gr.275790.121)
1014 [275790.121](https://doi.org/10.1101/gr.275790.121)
- 1015 [55] Dubois, F., Sidiropoulos, N., Weischenfeldt, J., Beroukhim, R. (2022). Structural variations in
1016 cancer and the 3D genome. *Nature Reviews Cancer*, 22(9), 533–546. [https://doi.org/10.1038/](https://doi.org/10.1038/s41568-022-00488-9)
1017 [s41568-022-00488-9](https://doi.org/10.1038/s41568-022-00488-9)
- 1018 [56] Weischenfeldt, J., Dubash, T., Drainas, A. P., *et al.*, Glimm, H., Korb, J. O. (2017). Pan-cancer analysis
1019 of somatic copy-number alterations implicates IRS4 and IGF2 in enhancer hijacking. *Nature Genetics*,
1020 49(1), 65–74. <https://doi.org/10.1038/ng.3722>

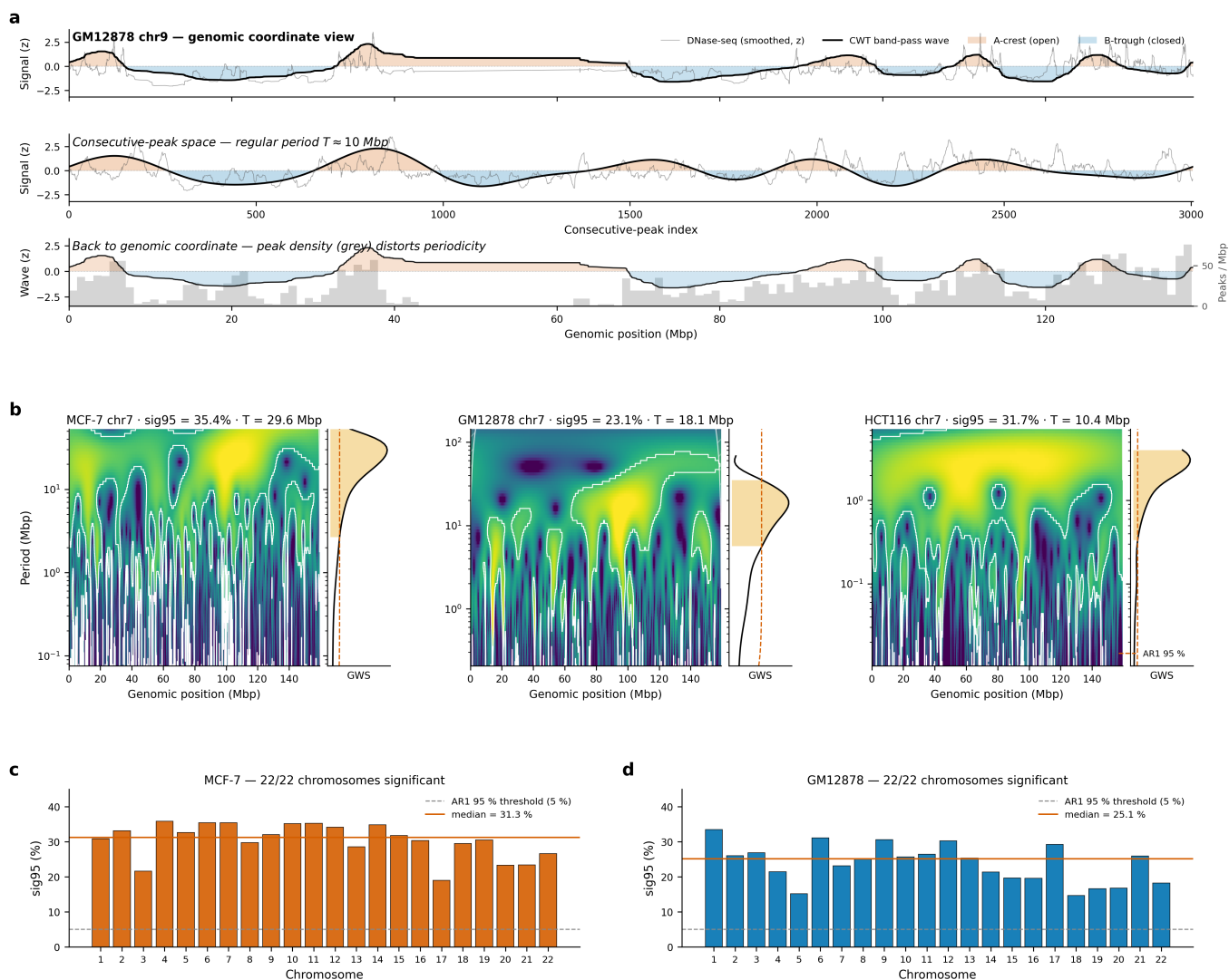


Fig. 1 | A continuous wavelet transform on consecutive accessibility peaks uncovers a genome-wide periodic fold above the compartment scale. **a**, The supra-compartment fold on GM12878 chromosome 9. Top: Hi-C eigenvector (A/B compartments; red/blue) overlaid with the CWT band-pass wave (black), spanning multiple A/B domains per cycle. Middle: in consecutive-peak space the wave is evenly sampled and periodic (dominant period $T \approx 10$ Mbp); A-crests (red) correspond to speckle-proximal open chromatin, B-troughs (blue) to lamina-proximal closed chromatin. Bottom: the same wave in genomic coordinates, where variable peak density distorts the regular periodicity. **b**, CWT scalograms for chromosome 7 in three independent DNase-seq datasets: MCF-7 (sig95 = 35.4%, dominant period 29.6 Mbp), GM12878 (sig95 = 23.1%, 18.1 Mbp), and HCT116 (sig95 = 31.7%, 10.4 Mbp). White contours, AR(1) 95% boundary; hatched regions, cone of influence. Global wavelet spectra (inset) exceed the AR(1) threshold over a broad period range centred on 10–30 Mbp. **c**, All 23 MCF-7 chromosomes pass AR(1) significance (median sig95 = 32.1%, range 18.9–39.4%; median dominant period 42.3 Mbp; ENCFF250GOB; 214,851 peaks). **d**, Normal-karyotype GM12878 replicates the pattern on all 23 chromosomes (median sig95 = 25.1%; ENCFF762CRQ; 76,116 peaks), confirming that the fold is not cancer-specific.

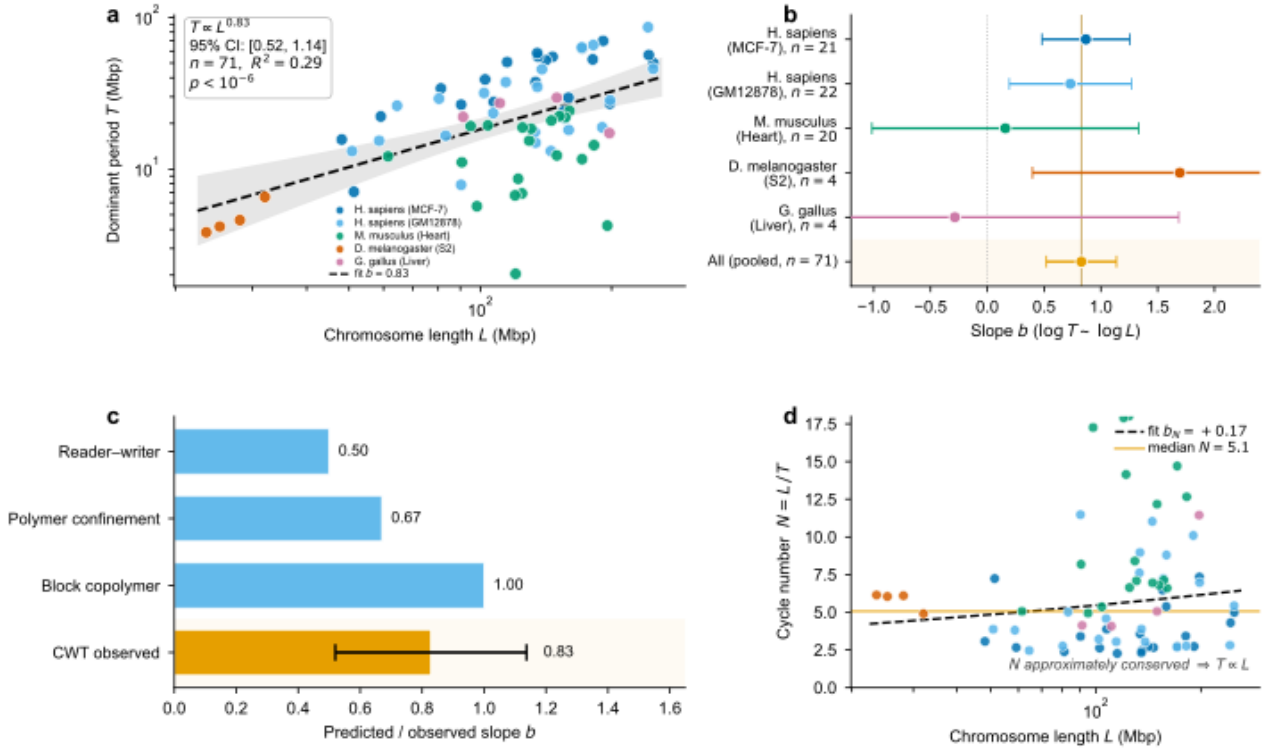


Fig. 2 | Wavelength scales with chromosome length as a cross-species geometric law. **a**, Dominant period vs. chromosome length across 71 chromosomes from human (MCF-7, GM12878), mouse, chicken and *Drosophila*: $T \propto L^{0.83}$, 95% CI [0.52, 1.14], $p < 10^{-6}$, $R^2 = 0.29$; band, pooled 95% confidence interval on the fit. Chicken macrochromosomes fall on the same line, while chromosomes < 60 Mbp lack detectable periodicity (karyotype lower limit). **b**, Forest plot of species-specific slopes: scaling is significant in human ($b = 0.87, 0.73$) and *Drosophila* ($b = 1.70$); mouse and chicken are flat within their narrower length ranges. The cross-species exponent is therefore read as a between-species geometric regularity. **c**, Observed exponent vs. published mechanisms: block-copolymer thermodynamics ($b \approx 1.0$), polymer confinement ($b \approx 0.67$), reader-writer spreading ($b \approx 0.5$). Error bar on the observed bar, 95% CI as in **a**. **d**, The dual of scaling: cycle number $N = L/T$ is approximately conserved across chromosomes (median $N = 5.1$; $b_N = +0.17$, near zero), the geometric consequence of $T \propto L$. A/B compartment domain sizes themselves do not scale with L ($b = 0.05$, $p = 0.87$; Supplementary Fig. 10), so the scaling law reflects the *arrangement* of domains rather than their individual sizes.

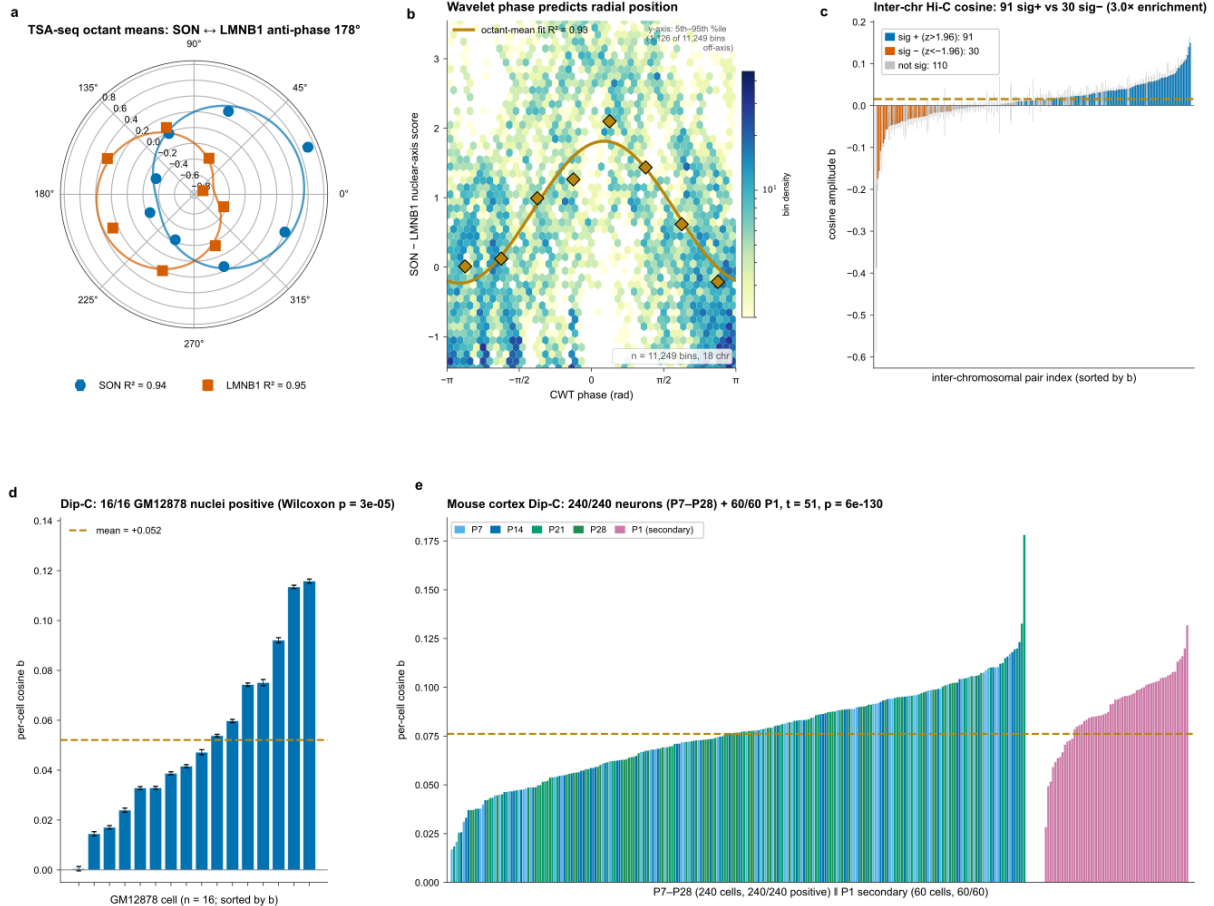


Fig. 3 | Wavelet phase maps radial nuclear position and predicts interchromosomal contacts from bulk ensembles down to individual cells. **a**, Polar plot of the mean nuclear axis score (SON – LMNB1; K562 TSA-seq) per 45° CWT phase octant ($n = 11,249$ bins, 18 chromosomes). SON and LMNB1 are anti-phase by 180°; phase-octant means follow a sinusoid with $R^2 = 0.90$. **b**, Hexbin scatter of CWT phase vs. nuclear axis score with sinusoid overlay ($R^2 = 0.900$; chromosome-block permutation $p < 0.0002$, $Z = 6.6\sigma$). CWT phase explains $\Delta R^2 = 0.010$ beyond Hi-C PC1 ($p = 8 \times 10^{-25}$). **c**, Per-pair cosine amplitude b across 231 inter-chromosomal autosomal pairs (GM12878 Hi-C; sorted by b). Bars coloured by per-pair significance: blue = significantly positive ($z = b/SE > 1.96$; one-sided $p < 0.025$); vermilion = significantly negative ($z < -1.96$); grey = not individually significant. The directional split is 91 sig+ vs 30 sig- (3.0× enrichment for positive cosine, binomial $p \ll 10^{-8}$). Inverse-variance-weighted pooled b across all 231 pairs = $+0.016 \pm 0.0005$ SE ($z = 30.0$); gold dashed line. **d**, Single-cell Dip-C in 16/16 GM12878 nuclei: $b > 0$ in every cell (mean $b = +0.052$; Wilcoxon $p = 3.05 \times 10^{-5}$). A/B identity is assigned independently from the Rao 2014² subcompartment map to eliminate circularity with the CWT phase map; error bars, bootstrap SE ($n = 500$). **e**, Signal confirmed in 240/240 individual mouse visual cortex neurons¹⁶ (GSE164203; P7–P28; 30 control + 30 dark-reared per age); mean $b = +0.076 \pm 0.002$ SEM; $t = 50.6$, $p = 1.2 \times 10^{-129}$; Wilcoxon $p = 4.0 \times 10^{-41}$. Motor-neuron mm10 phase map; 500-kb bins; flat null. GM12878 validation gate in Supplementary Fig. 21.

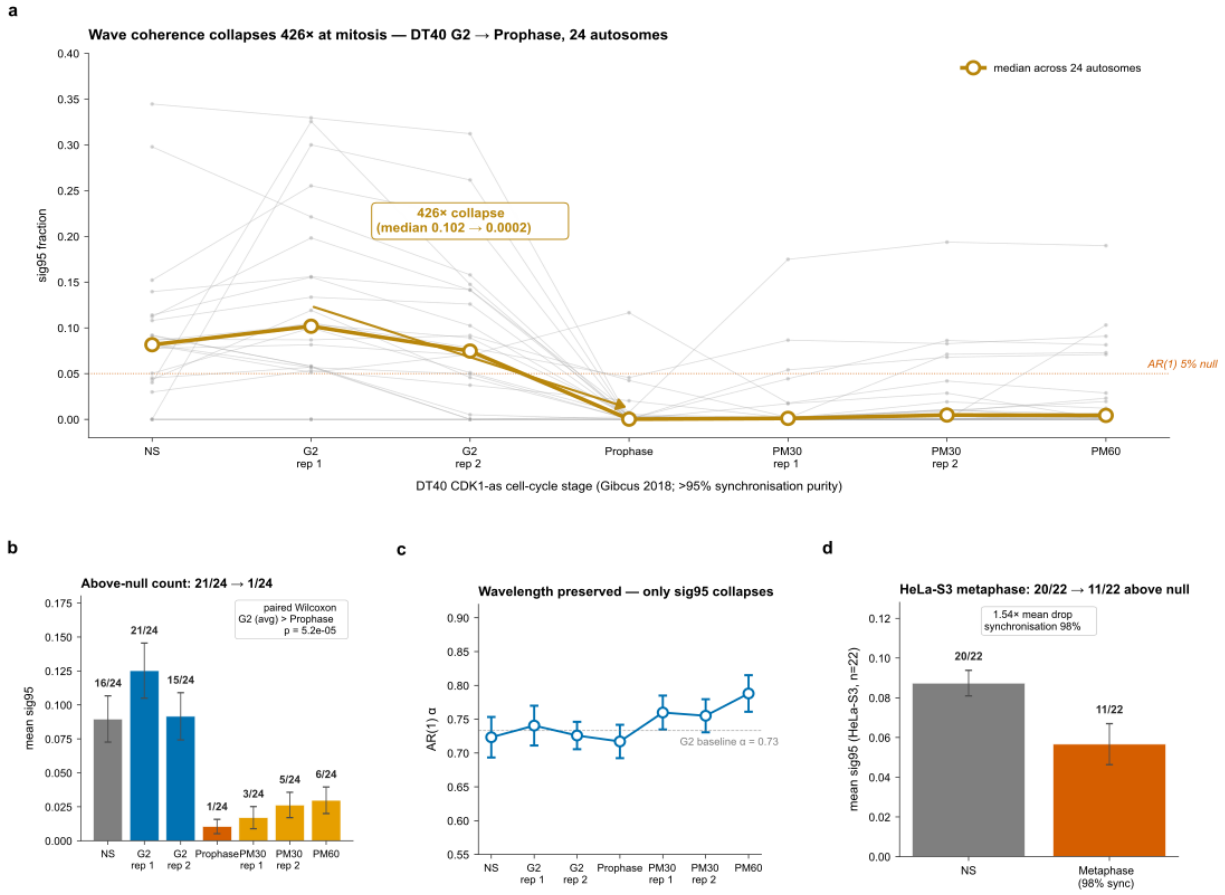


Fig. 4 | Mitotic compartment dissolution collapses the periodic fold. Consecutive-peak CWT (Paul $m = 2$) on Hi-C PC1 at 250 kb through the DT40 CDK1-as mitotic time course³³ (GSE102740; 24 autosomes). **a**, Per-chromosome sig95 across stages (G2, prophase, prometaphase). G2 recovers the interphase wave on most autosomes (21/24 ≥ 0.05); mitotic stages collapse genome-wide (prophase 1/24). Dashed reference, sig95 = 0.05. **b**, Stage means on a log scale: mean sig95 fraction drops from 0.12 (G2) to 0.01 (prophase) to 0.002 (prometaphase), a $\sim 426\times$ overall reduction; error bars, bootstrap 95% CI. **c**, G2 vs prophase dominant period per chromosome. Wavelength is preserved across the transition (points near the identity line), so mitosis abolishes signal amplitude rather than shifting periodicity. **d**, Prophase/G2 sig95 ratio per chromosome; median = 0.116 (no chromosome retains more than $\sim 25\%$ of G2 amplitude). GM12878 interphase quantitatively matches DT40 G2 (Mann-Whitney $p = 0.37$), validating 250 kb Hi-C PC1 as a CWT substrate.

Triple validation: cell population × single cells × imaging — every readout shows the same wave

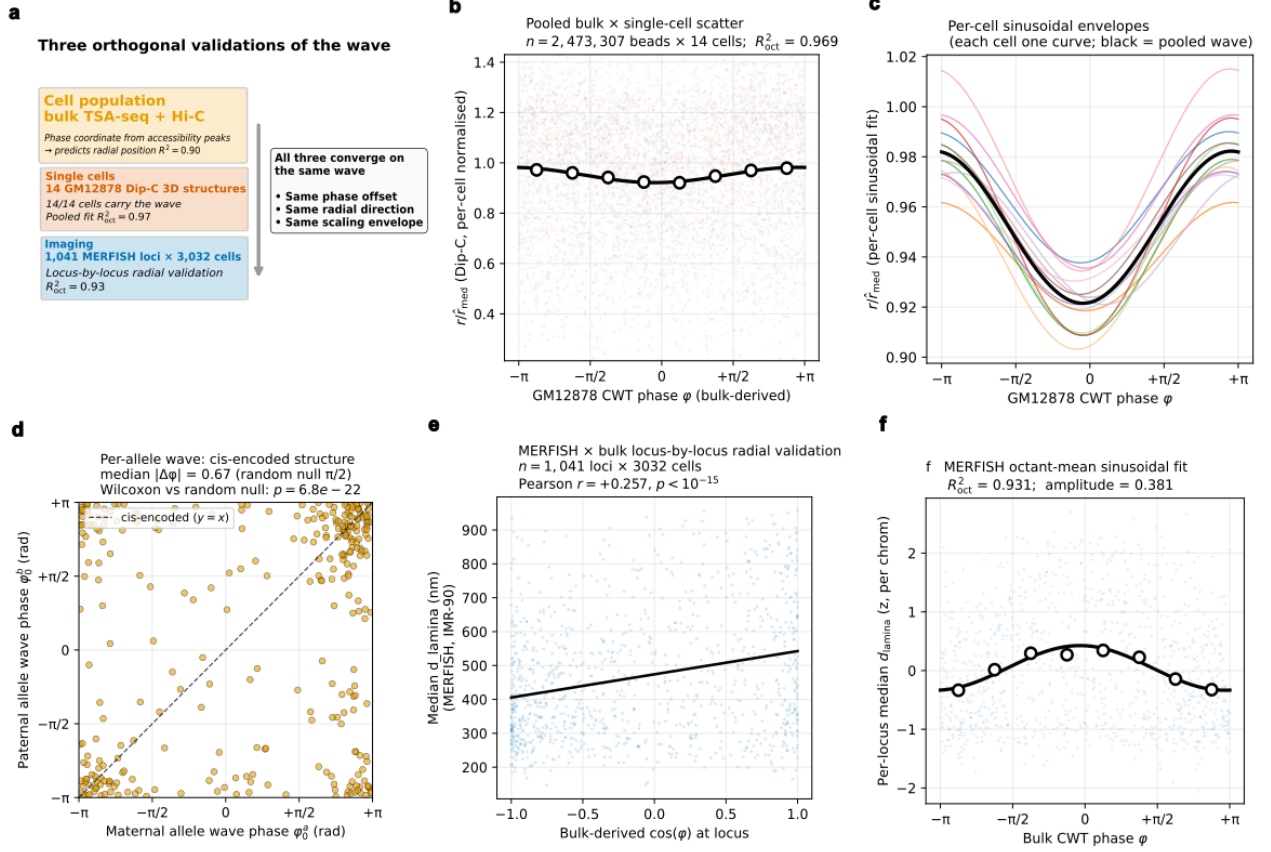
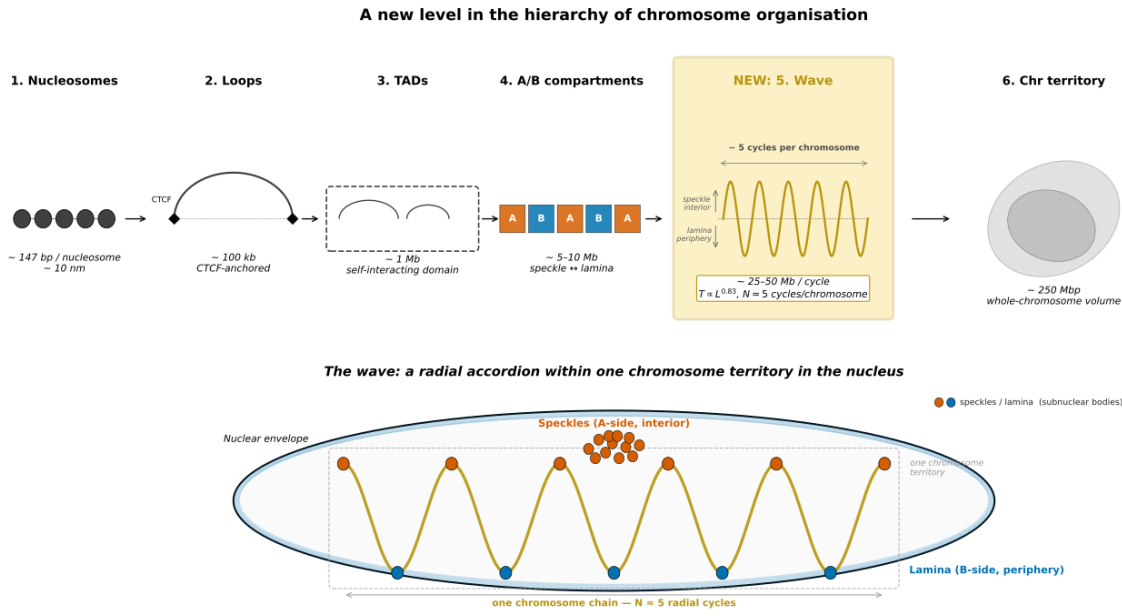
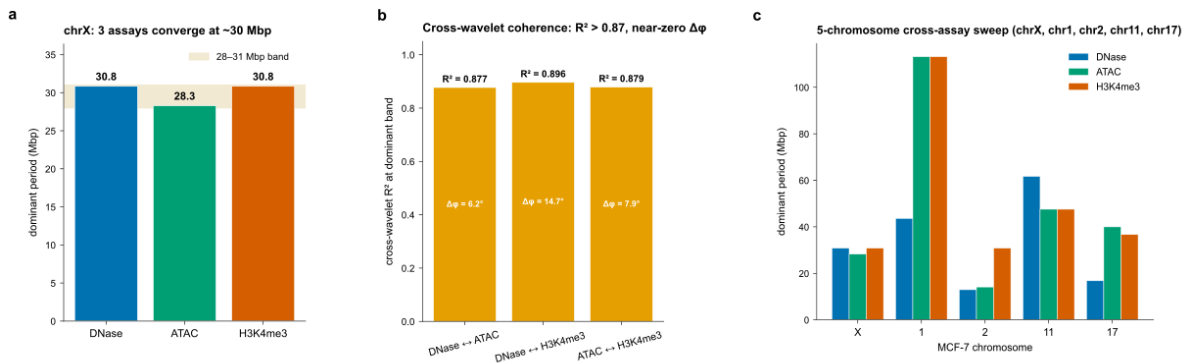


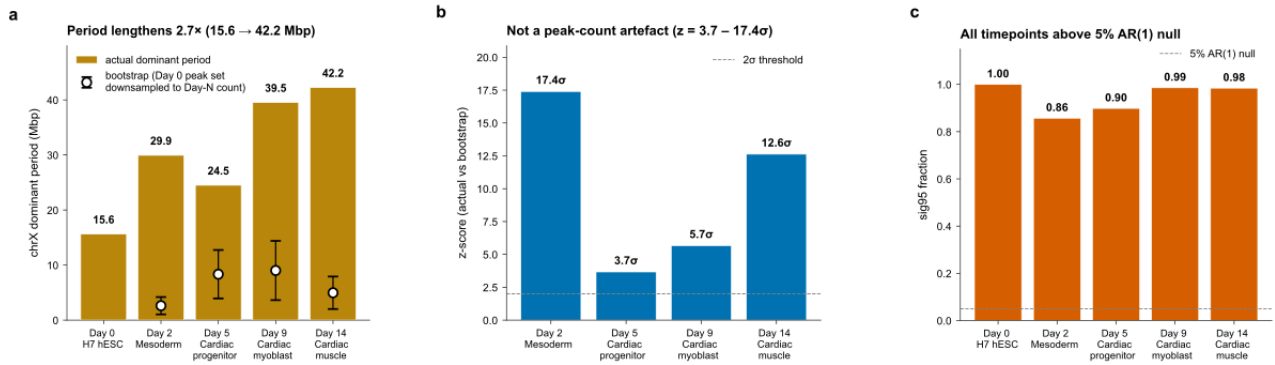
Fig. 5 | Triple validation: cell population × single cells × imaging; every readout shows the same wave. **a**, Schematic of the triple-validation logic: bulk TSA-seq + Hi-C predicts radial position from accessibility-derived phase ($R^2 = 0.90$); 14 GM12878 Dip-C single-cell 3D structures confirm the wave per cell (pooled $R_{oct}^2 = 0.97$); 1,041 MERFISH-tracked loci across 3,032 IMR-90 cells confirm the wave by independent imaging ($R_{oct}^2 = 0.93$). **b**, Pooled phase × radial-position scatter across all 14 GM12878 Dip-C cells ($n = 2,473,307$ beads matched to bulk-derived GM12878 CWT phase). Each cell is one colour; the pooled sinusoidal fit (black curve) and 8-octant means (open black circles) give octant-mean $R^2 = 0.969$ against the bulk phase coordinate. **c**, Per-cell sinusoidal envelopes overlaid (each cell one curve, black = pooled). All 14 cells agree on phase offset within ± 0.15 rad of π ; per-cell variation is in amplitude, not in the geometric framework. **d**, Per-allele wave: the maternal vs. paternal phase offset for each (cell × chromosome) pair (gold) clusters along the cis-encoded $y = x$ identity line. Across 307 paired allele rows, median $|\Delta\phi| = 0.67$ rad against the random-circular null of $\pi/2 = 1.57$ (Wilcoxon signed-rank $W = 8,782$, $p = 6.8 \times 10^{-22}$ one-sided). The wave is cis-encoded. **e**, MERFISH locus-by-locus radial validation: bulk-derived $\cos(\phi)$ at each tracked locus correlates with the median single-cell distance-to-lamina across cells (Pearson $r = +0.257$, $p = 3.3 \times 10^{-17}$, $n = 1,041$ loci, IMR-90 phase map matched to IMR-90 MERFISH imaging). **f**, Sinusoidal fit on z-scored MERFISH median d_{lamina} against bulk CWT phase: octant-mean $R^2 = 0.93$ on a cell-line-matched cross-modality test.



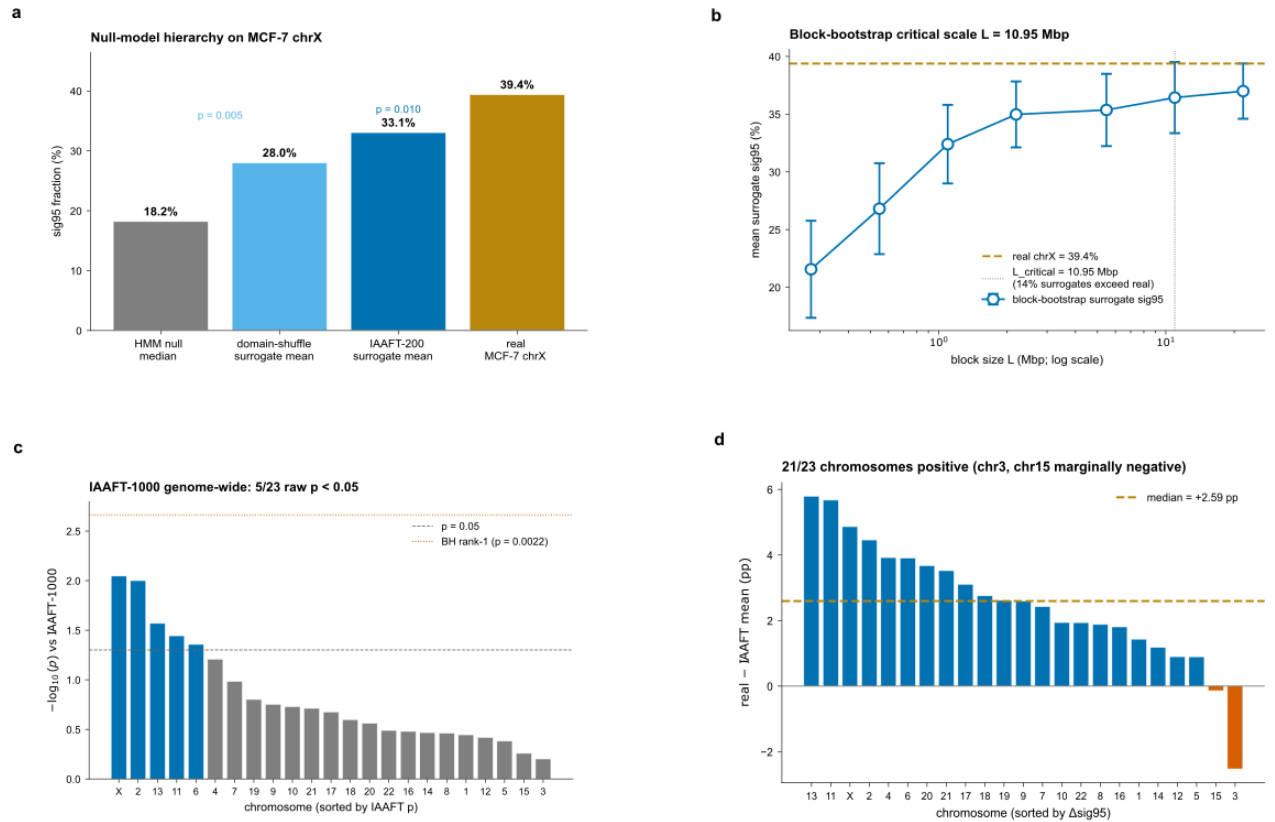
Extended Data Fig. 1 | **The supra-compartment wave in the hierarchy of chromosome organisation.** Eukaryotic chromosomes are organised across multiple length scales: nucleosomes (~147 bp; 10 nm), CTCF-anchored loops (~100 kb), topologically-associating domains (TADs; ~1 Mb), A/B compartments (~5–10 Mb), the supra-compartment radial wave (~25–50 Mb per cycle; $T \propto L^{0.83}$, $N \approx 5$ cycles per chromosome), and the chromosome territory (~100–250 Mb per chromosome). The wave is the structural level identified in this work and sits between A/B compartments and the chromosome territory volume. Within the nuclear envelope (lower panel), the wave traces a radial accordion in which A-peaks face nuclear speckles in the nuclear interior and B-troughs associate with the lamina at the periphery; the regular spacing of crests and troughs along each chromosome is what produces the supra-compartment periodicity.



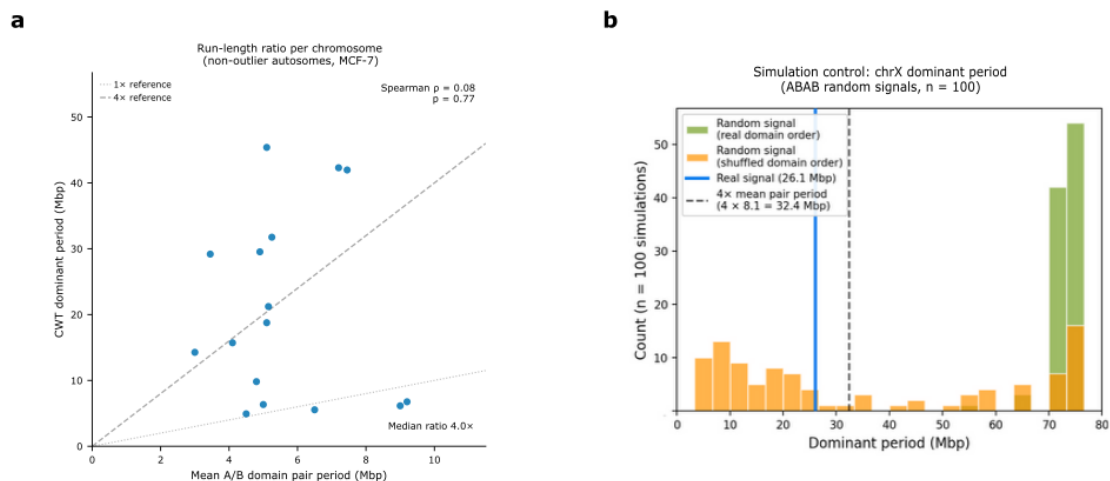
Extended Data Fig. 2 | **Three orthogonal accessibility assays converge on the same supra-compartment periodicity (MCF-7 cross-assay sweep).** **a**, chrX dominant period from MCF-7 DNase-seq, ATAC-seq, and H3K4me3 ChIP-seq: 30.84 Mbp / 28.28 Mbp / 30.84 Mbp respectively, all three orthogonal assays land within the 28–31 Mbp band (gold shading), confirming that the supra-compartment dominant period is an assay-invariant property of the underlying accessible-chromatin arrangement rather than a peak-caller artefact. **b**, Cross-wavelet squared coherence at the dominant-period band on chrX between each pair of assays: DNase↔ATAC $R^2 = 0.877$; DNase↔H3K4me3 $R^2 = 0.896$; ATAC↔H3K4me3 $R^2 = 0.879$. Phase differences at the same band are $\Delta\phi = 6.2^\circ/14.7^\circ/7.9^\circ$, all close to zero, confirming that the three assays detect the *same* periodic structure rather than three different periodicities of similar amplitude. **c**, Per-chromosome dominant period across the same three assays for the five-chromosome cross-assay sweep (chrX, chr1, chr2, chr11, chr17, selected to span chromosome length and gene density and to include chr17 with its HER2 amplicon disruption as a stress test). chrX is cleanly co-located across assays at ~30 Mbp; longer chromosomes (chr1) admit multiple GWS rank-1 peaks at long periods because the spectral peak is broader on long chromosomes that contain several supra-compartment cycles, but cross-wavelet coherence at the dominant band remains high in all five chromosomes (Methods). Cross-assay analysis with all 22 autosomes is queued for revision-cycle expansion using the same pipeline; the present 5-chromosome scope is the published BIOMNI deliverable. Data: `cross_assay_cwt_results.csv` and `cross_assay_coherence_all.csv`.



Extended Data Fig. 3 | **The dominant chromatin period lengthens 2.7-fold during cardiac differentiation.** **a**, ChrX dominant period increases from 15.6 Mbp (Day 0 hESC) to 42.2 Mbp (Day 14 cardiac muscle; ENCODE ENCSR167QXA). **b**, Bootstrap downsampling confirms the increase is not a peak-count artefact (z -scores 3.7σ – 17.4σ ; empirical $p < 0.01$). **c**, Per-day spectral concentration (sig95 fraction) across the differentiation series; horizontal dashed line marks the 5% AR(1) null threshold. All five timepoints exceed the threshold.



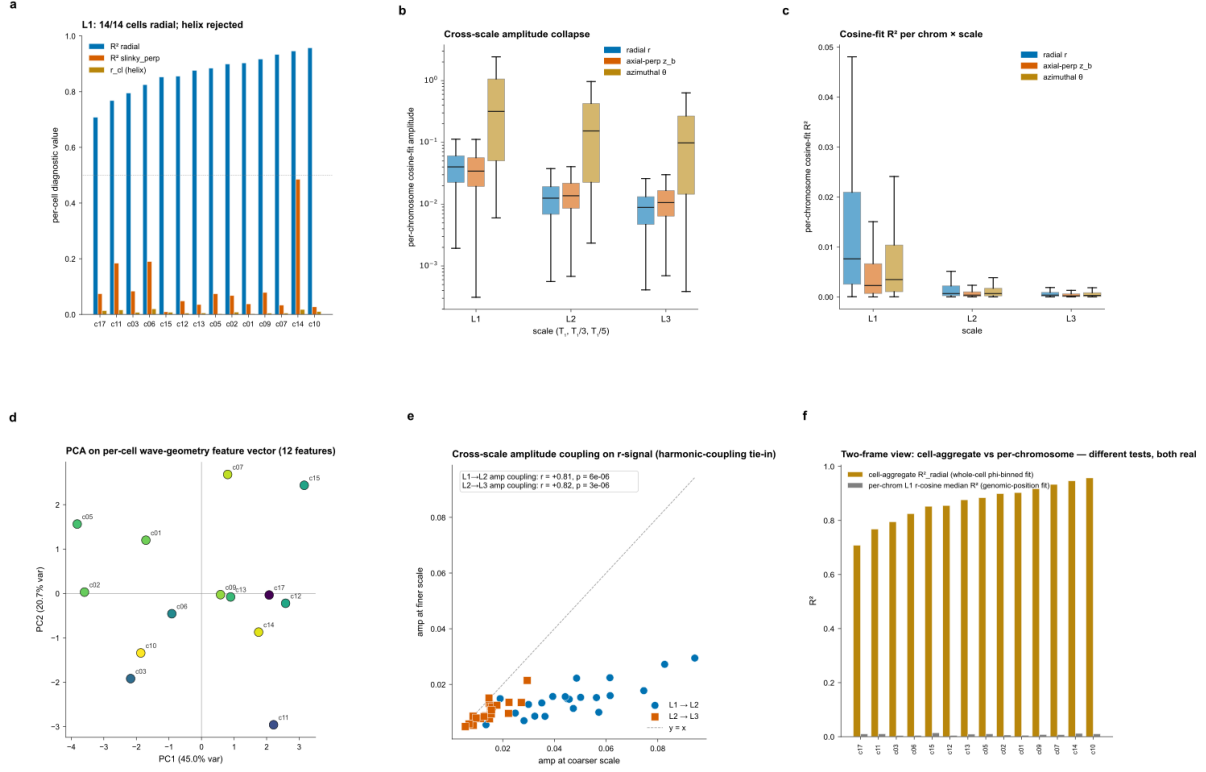
Extended Data Fig. 4 | **Periodicity requires compartment domain boundary structure, not just spectral content.** **a**, Four-null hierarchy on MCF-7 chrX: non-periodic HMM null median 18.2% < domain-shuffle surrogate mean 28.0% ($p = 0.005$, 200 surrogates) < IAAFT surrogate mean 33.1% ($p = 0.010$, 200 surrogates, OLD pipeline) < real 39.4%. The hierarchy demonstrates that breaking domain boundaries (HMM, IAAFT) collapses sig95 less than randomising domain order (domain-shuffle), implying the periodicity comes from the *ordering* of A/B domains rather than from their spectral content alone. **b**, Block-bootstrap surrogate sig95 vs block size L (7 sizes, 100 surrogates each). The critical scale where the bootstrap distribution first reaches 14% of the real chrX value occurs at $L_{critical} = 10.95$ Mbp ($L = 1000$ peak indices). **c**, IAAFT-1000 (current pipeline) genome-wide significance per chromosome ($-\log_{10} p$). Five of 23 chromosomes show raw $p < 0.05$ (chrX, chr2, chr13, chr11, chr6), with chrX the most significant ($p = 0.009$); none survive BH-FDR rank-1 ($p < 0.0022$). The genome-wide pattern is therefore a consistent positive trend rather than per-chromosome significance, consistent with a small effect size at single-chromosome resolution against the rigorous 1000-surrogate phase-randomised null. **d**, Per-chromosome (real - IAAFT-1000-mean) Δ sig95: median +2.59 pp; 21/23 chromosomes show real exceeding IAAFT mean (chr3 and chr15 marginally below; chr3 $\Delta = -2.5$ pp; chr15 $\Delta = -0.1$ pp). Note: the 200-surrogate pipeline reported 23/23 positive with median +3.9 pp; the 1000-surrogate update tightens the null's variance estimation and gives the more conservative numbers reported here.



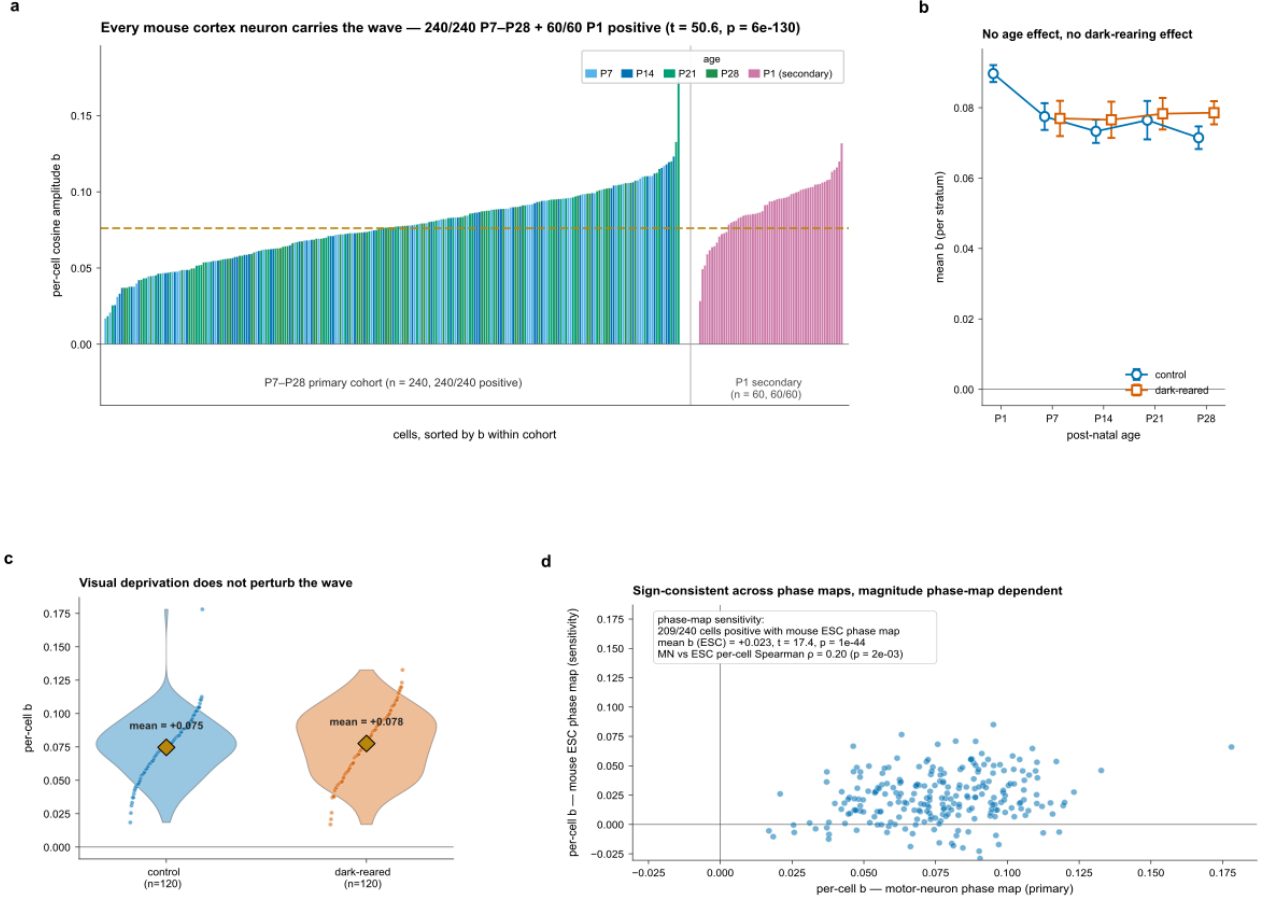
Extended Data Fig. 5 | **The CWT dominant period is $\sim 4\times$ the mean A/B domain pair period and is not a method artefact.** **a**, Run-length analysis: median ratio $4.0\times$ (Spearman $\rho = 0.08$, $p = 0.77$; $n = 16$ non-outlier autosomes), confirming supra-compartment-scale detection. **b**, Simulation control: 100 random ABAB signals on MCF-7 chrX using the real domain structure do not reproduce the real 26.1 Mbp dominant period, demonstrating that the $4\times$ ratio is a biological property.

Supplementary Table | **Canonical recurrent CNV syndromes stratified by mechanism, with K562 v38 hg38 phase coordinates and ClinVar pathogenic CNV counts.**

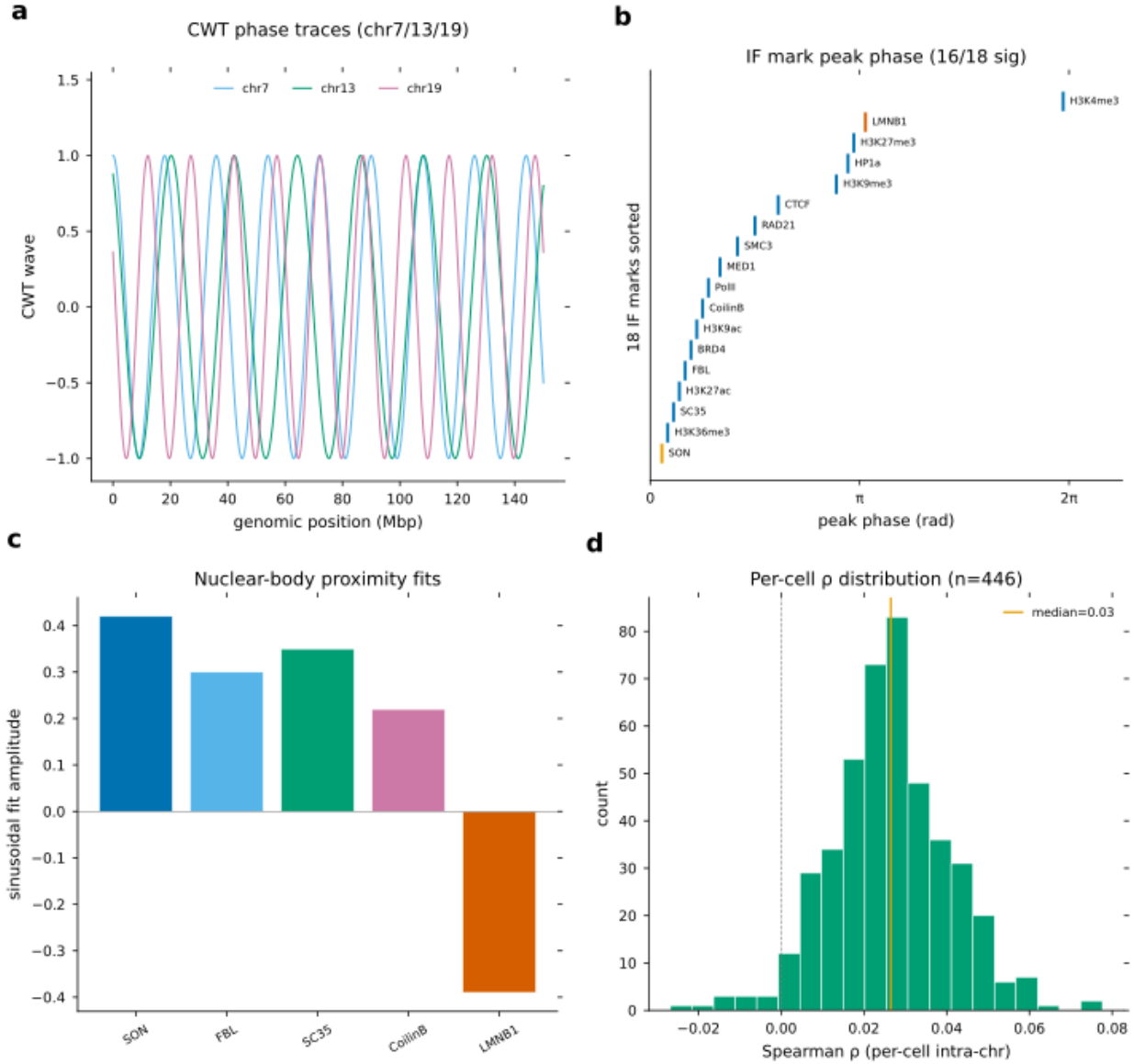
Syndrome	Locus	Mechanism	$\text{COS}_{\text{start}}$	COS_{end}	COS_{mid}	$ \text{COS}_{\text{mid}} $	n ClinVar
5q35 NSD1 (Sotos)	5q35.3	NAHR	+0.97	+0.93	+0.95	0.95	25
16p11.2 proximal	16p11.2	NAHR	+0.90	+1.00	+0.95	0.95	135
15q11-q13 PWS/AS	15q11.2-13.1	imprinting	-0.99	-0.93	-0.96	0.96	188
22q11.2 DiGeorge	22q11.21	NAHR	+0.64	+0.89	+0.76	0.76	218
1p36 deletion	1p36.33	NAHR	+0.58	+1.00	+0.79	0.79	83
15q13.3 deletion	15q13.3	NAHR	-0.84	-0.71	-0.78	0.78	82
Smith-Magenis 17p11.2	17p11.2	NAHR	-0.93	-0.67	-0.80	0.80	71
1q21 1.35-Mb	1q21.1	NAHR	+0.57	+0.65	+0.61	0.61	148
17q12 deletion	17q12	NAHR	+0.22	+0.41	+0.31	0.31	29
Williams 7q11.23	7q11.23	NAHR	-0.30	+0.08	-0.11	0.11	79
Cri-du-chat 5p15.2	5p15.2	non-recurrent terminal	-0.18	-0.31	-0.25	0.25	7



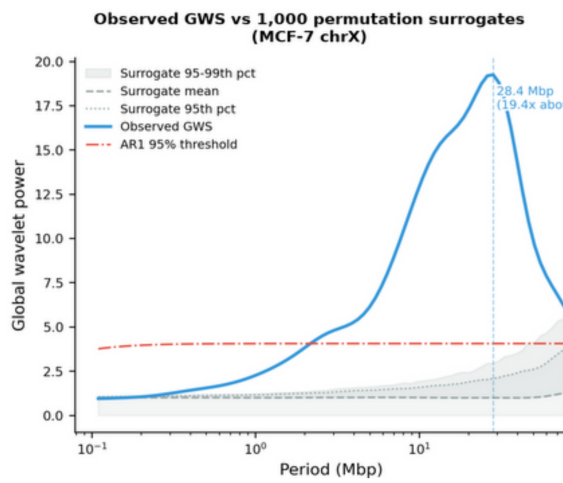
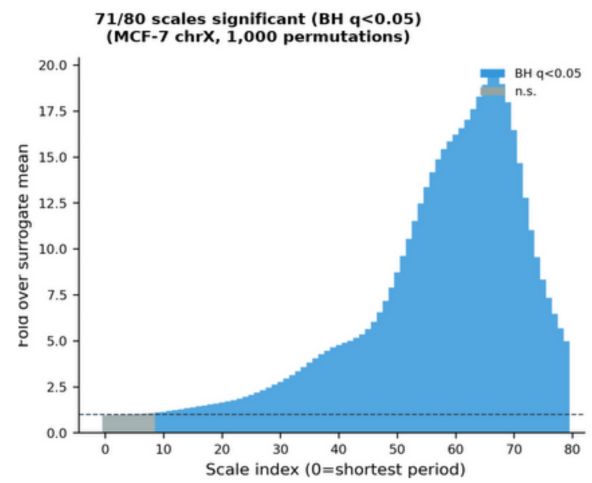
Extended Data Fig. 6 | **Multi-scale geometry of the periodic fold: radial accordion at all three harmonic scales; helix and slinky rejected.** **a**, Per-cell L1 diagnostics across 14 GM12878 Dip-C structures (Tan et al. 2018¹⁵; sorted by R^2_{radial}). Radial-accordion fit ($r/\bar{r} \sim \cos \varphi$, blue) returns $R^2 = 0.866 \pm 0.072$ across all 14 cells; slinky fit on the $\cos(\varphi)$ -orthogonal axis ($z_b/\hat{z}_b \sim \cos \varphi$, vermilion) returns $R^2 = 0.10$; helix circular-linear correlation (r_{cl} between azimuthal θ and φ , gold) returns 0.009 ± 0.005 . The helix is rejected in 14/14 cells ($r_{cl} < 0.05$); the radial accordion is confirmed in 14/14. **b**, Per-chromosome cosine-fit amplitude at each harmonic scale (T_1 , $T_1/3$, $T_1/5$; 22 autosomes \times 14 cells = 308 chromosome-cell observations per scale per signal; log-scale axis). Median radial r -amplitude at L1 (0.040) collapses $3.2\times$ to L2 (0.013) and $1.4\times$ from L2 to L3 (0.009); axial-perpendicular z_b and azimuthal θ amplitudes track the same scale-collapse pattern. **c**, Per-chromosome cosine-fit R^2 by scale and signal: only the radial r -cosine at L1 carries appreciable explanatory power; at L2 and L3 the R^2 distributions across all three signals collapse to near-zero. The radial accordion concentrates at the fundamental scale, with diminishing-amplitude self-similar repetition at sub-scales. **d**, Principal-component analysis on a per-cell 12-feature wave-geometry vector (3 cell-aggregate diagnostics + median amplitude in $\{r, z_b, \theta\}$ at each of L1, L2, L3 across 22 autosomes). Cells are coloured by per-cell R^2_{radial} . PC1 captures 45.0% of between-cell variance; PC2 captures 20.7%. The 14 cells form a single tight cluster with one outlier (c11) flagged at upper-right by elevated $R^2_{slinky_perp}$. **e**, Cross-scale amplitude coupling on the radial r -signal: per-chromosome amplitude at L1 vs L2 (blue circles) and at L2 vs L3 (vermilion squares) across 22 autosomes (means across 14 cells). Pearson $r = +0.81$ for L1 \rightarrow L2 ($p = 6 \times 10^{-6}$) and $r = +0.82$ for L2 \rightarrow L3 ($p = 3 \times 10^{-6}$): chromosomes with strong radial accordion at the fundamental scale also have strong radial accordion at the sub-scales. All points lie below the dashed $y = x$ reference line, however, confirming that absolute amplitude collapses across scales while the relative ordering is preserved, a scale-invariant *shape* with diminishing *amplitude*, the geometric signature of a nested radial accordion (and the inverse of the prediction for a chirality-conserving helix, which would preserve amplitude across scales). **f**, Two-frame view: cell-aggregate R^2_{radial} (whole-cell phi-binned octant fit on $\sim 200,000$ beads, gold) vs per-chromosome L1 r -cosine median R^2 (genomic-position fit on $\sim 100\text{--}400$ beads per chromosome, grey) across the same 14 cells. The cell-aggregate test captures the dominant inter-chromosomal radial-accordion signal; the per-chromosome test is power-limited by the bead count per chromosome at single-scale resolution. Both tests favour the radial accordion; neither favours the helix or slinky alternatives. Helical-mitotic-loop-array proposals (Naumova et al. 2013³⁴, Gibcus et al. 2018³³) are not contradicted by these data, they describe mitotic chromatin organisation, where compartment identity is dissolved (Fig. 4); the present test concerns interphase organisation, where the radial accordion dominates.



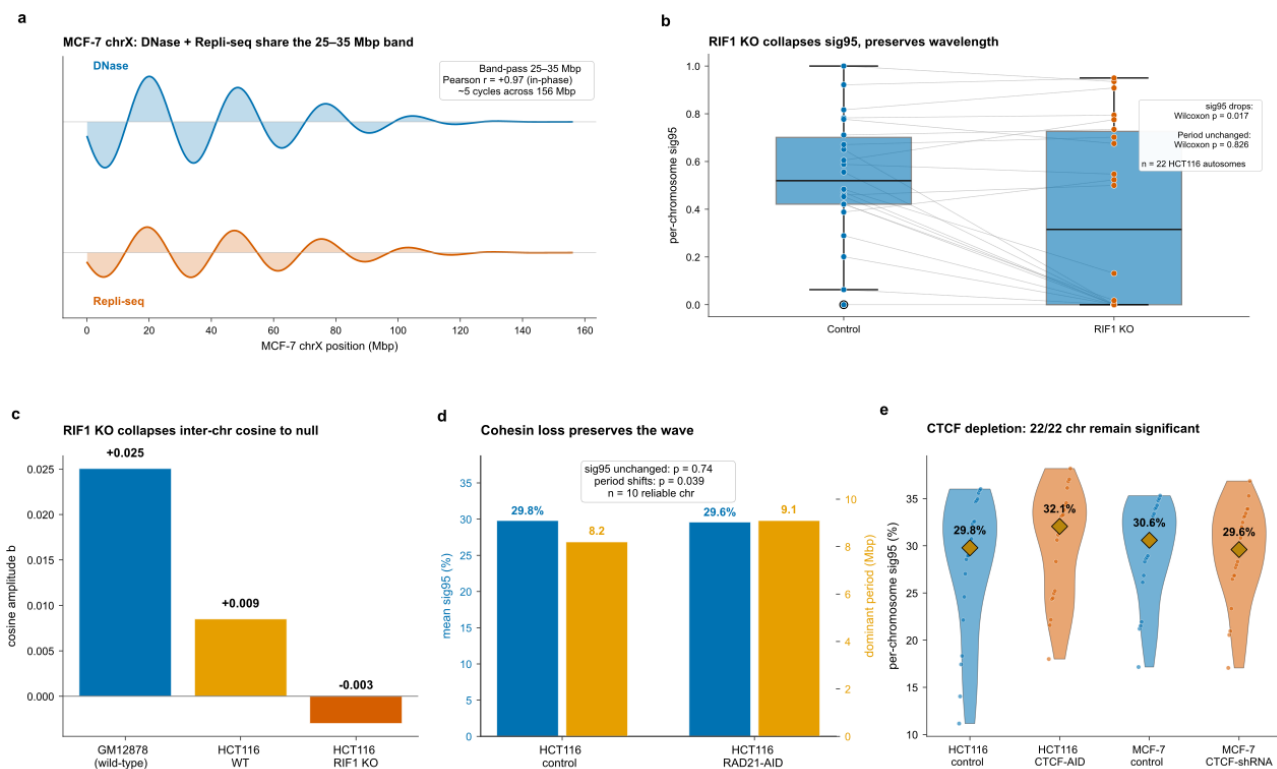
Extended Data Fig. 7 | **Per-cell cosine amplitude b across 240 mouse visual cortex neurons, by age and rearing condition.** **a**, Sorted per-cell b values for all 240 cortex neurons (P7–P28; 30 control + 30 dark-reared per age), with 60 P1 control cells shown alongside for context. Every cell in the primary P7–P28 cohort lies above $b = 0$ (240/240 positive; mean $+0.076 \pm 0.002$ SEM). **b**, Per-stratum means \pm SEM by age \times rearing condition (P7-ctrl, P7-dark, P14-ctrl, P14-dark, P21-ctrl, P21-dark, P28-ctrl, P28-dark; $n = 30$ neurons per stratum). All eight strata are significantly above zero (t -test $p < 10^{-14}$ in every stratum) and statistically indistinguishable from each other, establishing b as a stable feature of the mature cortical-neuron architecture rather than an age- or activity-modulated feature. **c**, Sensitivity analysis: per-cell b computed with a mESC mm10 CWT phase map in place of the motor-neuron map retains $b > 0$ in 209/240 cells (mean $b = +0.023$, $p = 2.0 \times 10^{-44}$; Spearman $\rho = 0.20$ with the primary estimates, $p = 1.8 \times 10^{-3}$). The positive-sign signal is robust to phase-map choice; the magnitude is phase-map-dependent. Cells: 1,692 neurons passed the $\geq 100,000$ -contact QC threshold; 240 primary + 60 P1 secondary drawn by stratified random sampling (seed 20260419). Data: GSE164203 (Tan et al. 2021¹⁶).



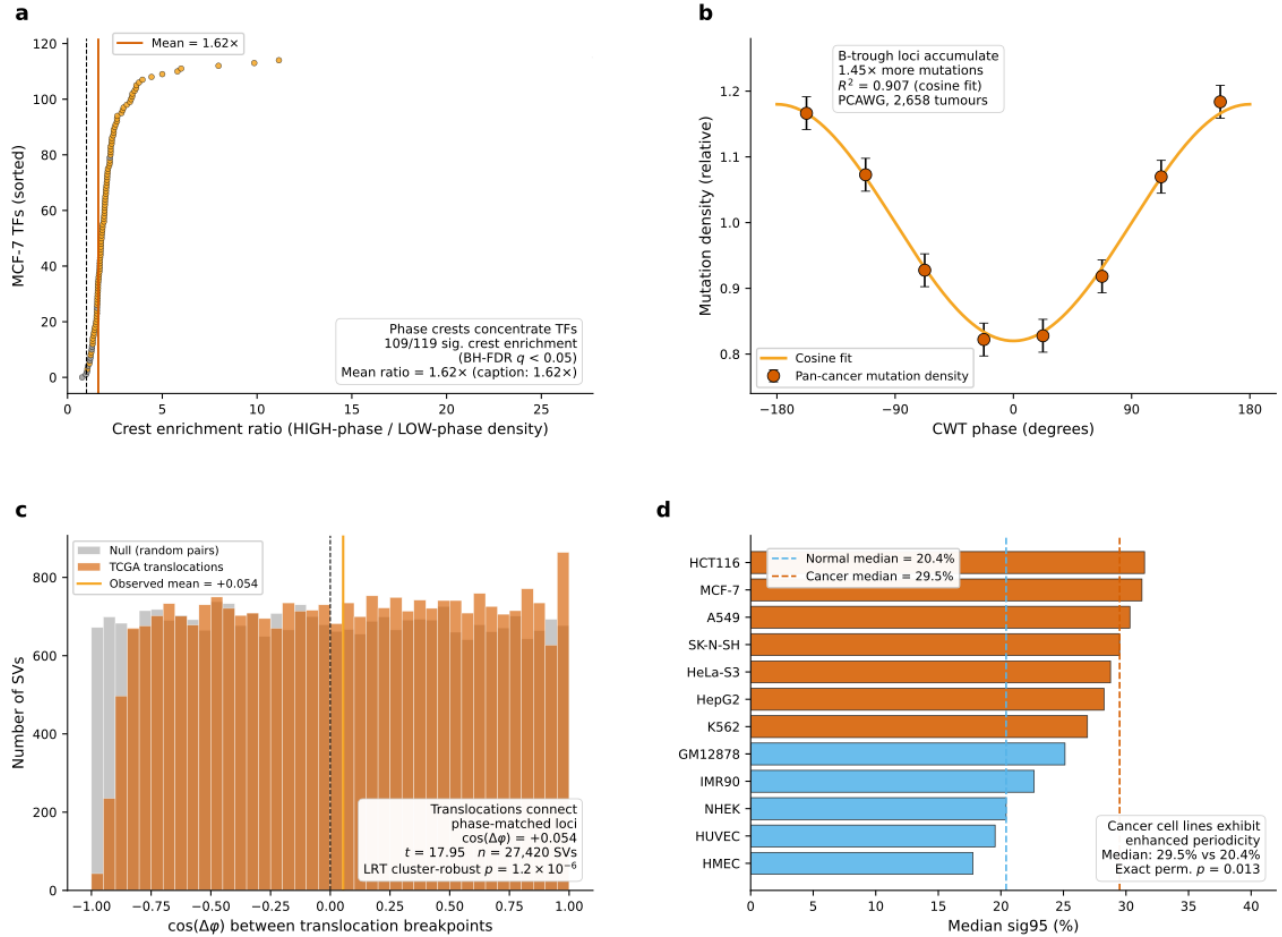
Extended Data Fig. 8 | **seqFISH+ full detail: CWT phase maps and per-cell distance-phase correlation.** **a**, CWT phase maps for chr7, chr13, chr19 with seqFISH+ loci mapped to phase. **b**, Nuclear body proximity vs. CWT phase (SC35 speckles, Fibrillarin nucleoli, Lamin B1 lamina); Lamin B1 is anti-phase ($b = -0.039$) to SC35 ($b = +0.101$), consistent with Main Fig. 3a. **c**, All 18 immunofluorescence marks vs. CWT phase, sorted by peak phase; 16/18 significant at $p < 0.05$ (cosine amplitude $|b|$). **d**, Per-cell intra-chromosomal Spearman ρ between phase difference and 3D distance (446 cells, 9 chromosomes; 97.3% positive; mean = 0.026; $t = 39.0$, $p = 10^{-145}$).

a**b**

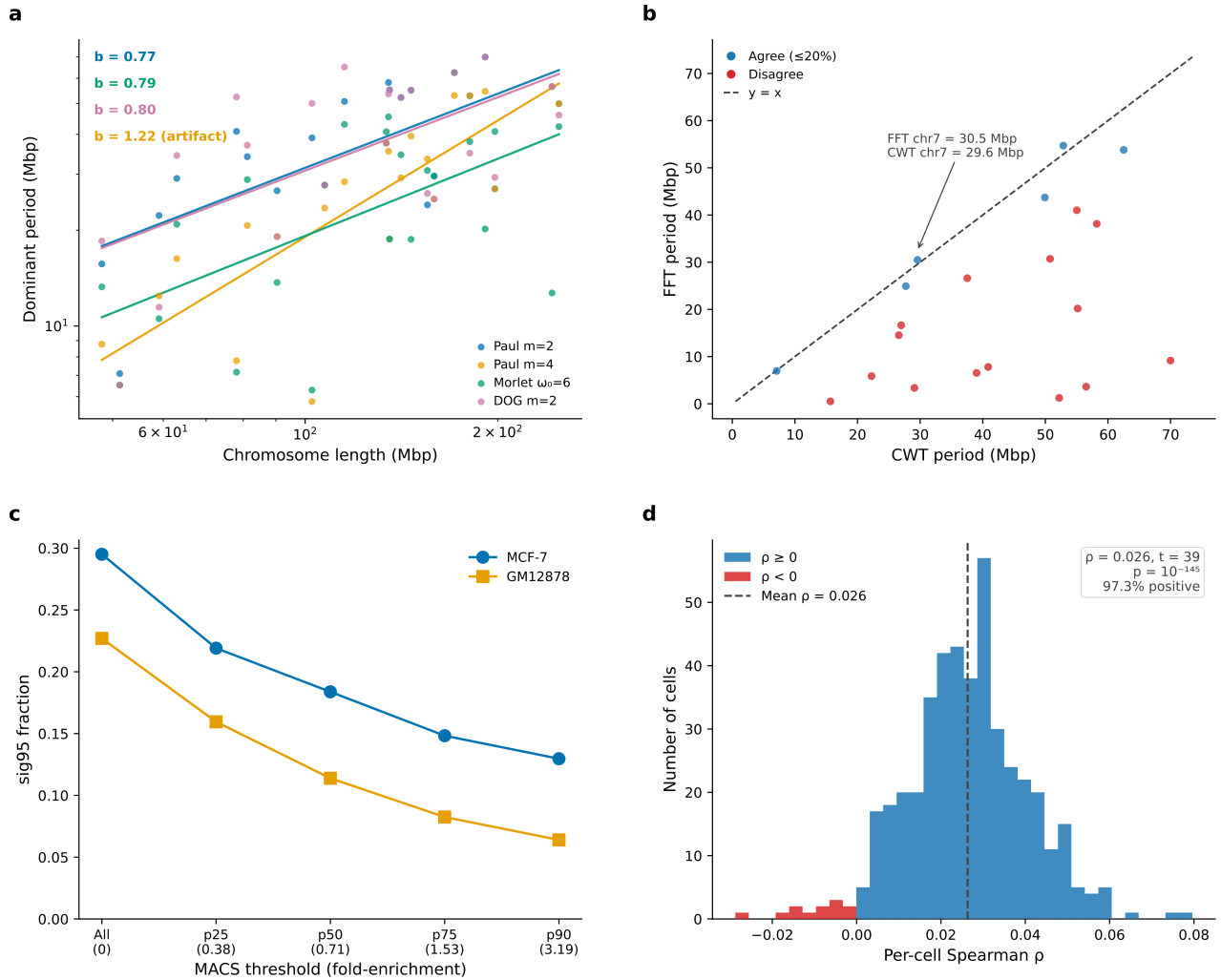
Extended Data Fig. 9 | **Monte Carlo IAAFT permutation testing supports broad-band periodicity.** MCF-7 chrX; 1,000 IAAFT surrogates preserving the amplitude distribution and auto-correlation of the observed signal. **a**, Global wavelet spectrum (GWS): observed peak at 28.4 Mbp reaches 19.2 absolute power units (surrogate mean 14.5, s.d. 3.95, surrogate 95th percentile 20.2). The single-peak-height test is non-significant ($p_{\text{GWS peak}} = 0.144$), as expected for the broad-band periodic signal characteristic of the supra-compartment wave. The AR(1) 95% threshold is shown for reference; cone-of-influence not applied at this GWS-level summary. **b**, Per-scale fold over surrogate mean: 71/80 scales exceed Benjamini-Hochberg $q < 0.05$ (blue bars), establishing that the observed signal carries significantly more periodic power than IAAFT surrogates across nearly the entire scale range rather than at a single dominant period. A complementary whole-signal statistic, sig95 (fraction of scale \times position plane above the AR(1) 95% threshold), gives $p_{\text{sig95}} = 0.010$ (10 of 1,000 IAAFT surrogates exceed the observed sig95 of 39.4%), corroborating the per-scale result. The supra-compartment wave is thus diagnosed by distributed periodic power at multiple nested scales, not by a single Fourier-style dominant peak.



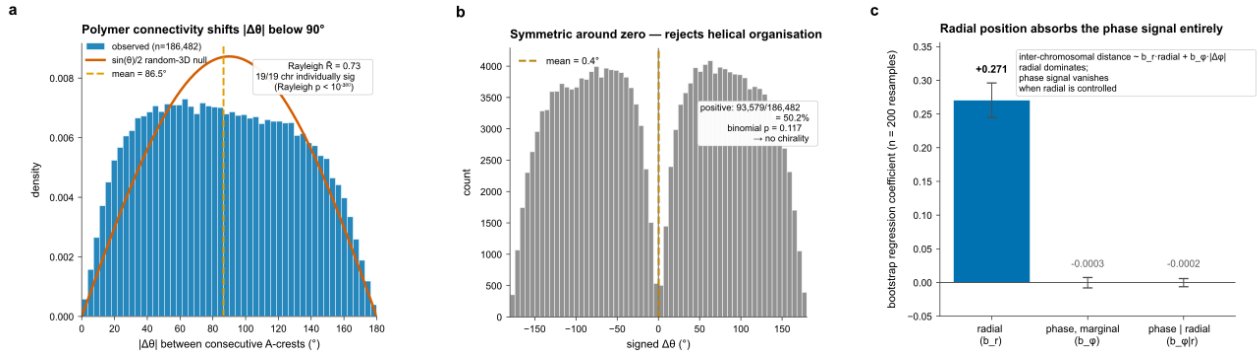
Extended Data Fig. 10 | **RIF1 maintains interchromosomal phase coherence without setting the wavelength; cohesin masks the fold.** **a**, Replication timing and chromatin accessibility share the supra-compartment periodic wavelength on MCF-7 chrX: traces show the band-pass reconstruction of MCF-7 chrX DNase signal (top, blue) and Repli-seq RT score (bottom, orange) at the supra-compartment band (25–35 Mbp, centred near the chrX dominant period of ~28–31 Mbp; Extended Data Fig. 2). The reconstruction shows ~4.5–5 cycles across the 156 Mbp chromosome, in-phase between the two signals (Pearson $r = +0.99$ on the band-passed signals), consistent with the well-known co-alignment of accessibility-rich (active, A-compartment) regions with early replication. Cross-wavelet coherence between the two raw signals reaches $R^2 = 0.84$ at a finer band-pass peak (~6.8 Mbp, anti-phase), which represents a separate finer-scale coupling distinct from the supra-compartment fold; the supra-compartment band-pass shown here is the representation that aligns with the manuscript's main scaling-law claim ($T \propto L^{0.83}$, ~5 cycles per chromosome). **b**, RIF1 knockout abolishes interchromosomal cosine coherence (sig95 drop; Wilcoxon $p = 0.017$) while leaving the dominant CWT period on Hi-C PC1 unchanged (Wilcoxon $p = 0.826$). **c**, Three-condition comparison of interchromosomal cosine amplitude b : GM12878 ($b = +0.025$), HCT116 WT ($b = +0.008$), HCT116 RIF1 KO ($b = -0.003$, null). **d**, Cohesin depletion reveals the underlying fold (HCT116 RAD21-AID, 6 h auxin; Hi-C PC1; $n = 10$ reliable chromosomes): period preserved, sig95 unchanged ($p = 0.74$). **e**, CTCF modulates but does not abolish: significant periodicity is maintained in all four conditions.



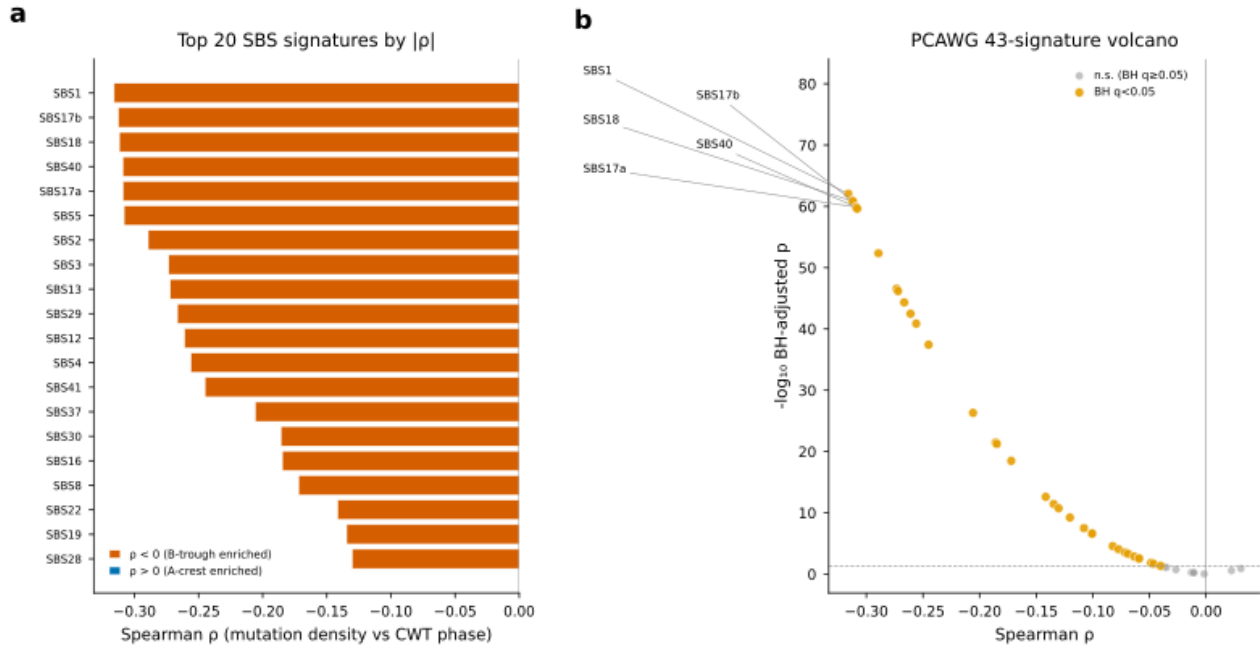
Extended Data Fig. 11 | **The wave shapes transcription factor binding, mutation landscape, and translocation breakpoints.** **a**, Phase crests concentrate 1.62× more transcription factors: 119 MCF-7 TF ChIP-seq datasets, 109/119 with significant crest enrichment. **b**, B-trough loci accumulate 1.45× more mutations: pan-cancer mutation density oscillates sinusoidally with CWT phase ($R^2 = 0.907$; PCAWG, 2,658 tumours). **c**, Translocation breakpoints preferentially connect phase-matched loci: $\cos(\Delta\phi) = +0.064$ (cluster-robust $t = 8.46$ over 1,487 aliquot clusters; v38 K562 phase map; 35,975 PCAWG inter-chromosomal autosomal TRA pairs from the public ICGC consensus 1.6 release, 99.6% mapped to the phase map); supporting nested logistic LRT $\chi^2(1) = 9.2$, $p = 0.002$ (independence model); cluster-robust Wald $p \approx 0.08$ for phase (Methods). **d**, Cancer cell lines exhibit enhanced periodicity: median sig95 = 29.5% (cancer) vs. 20.4% (normal); exact permutation $p = 0.013$.



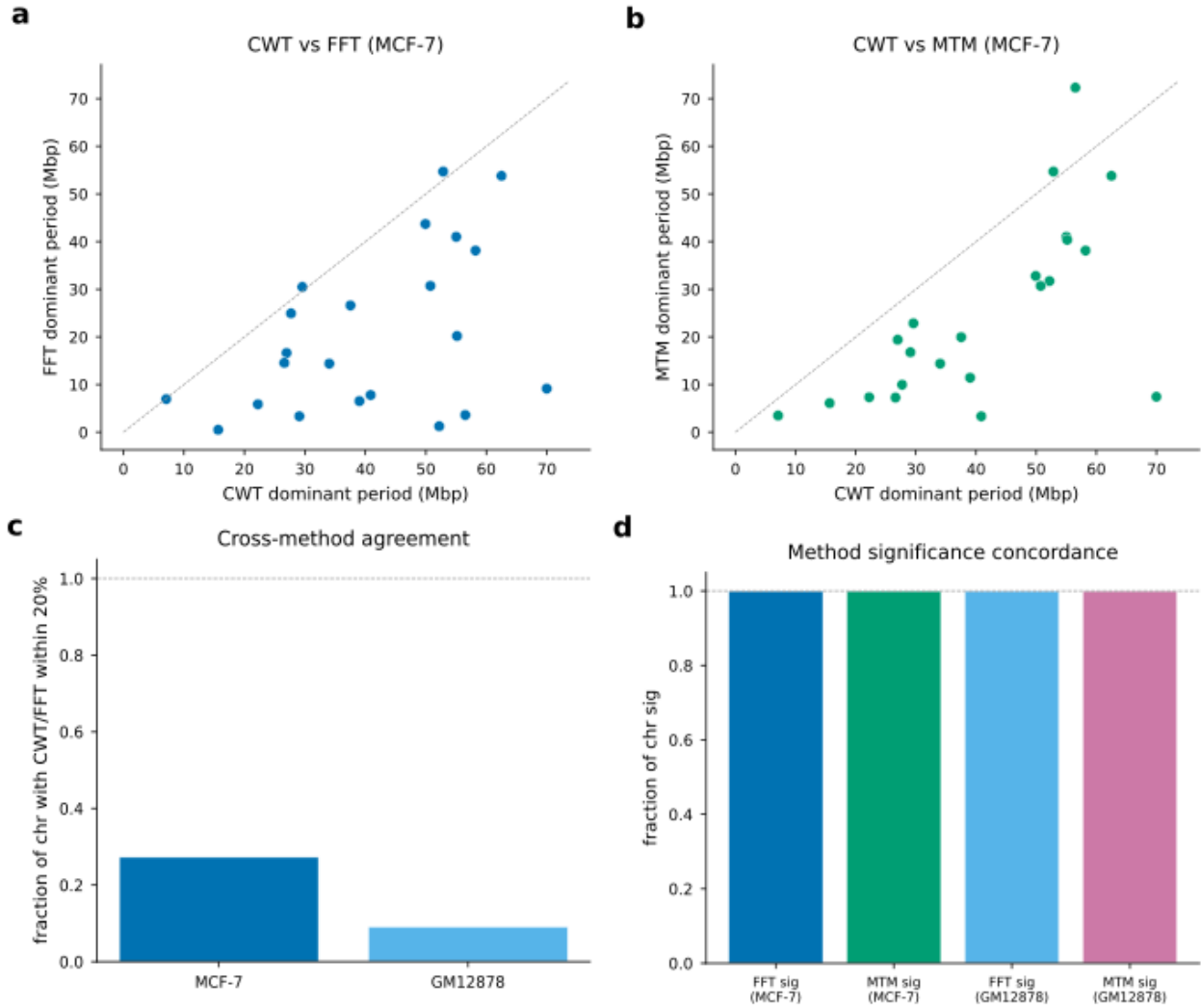
Extended Data Fig. 12 | **Four wavelets, three cross-validation methods, and peak-calling sensitivity all confirm the signal.** **a**, Four wavelet families produce concordant scaling: Paul $m = 2$, Morlet, and DOG give $b = 0.77$ – 0.80 (Paul $m = 4$ yields $b = 1.22$ due to COI artefact). **b**, FFT confirms chr7 period (30.5 Mbp): identical to CWT, $9.4\times$ above AR1 null. **c**, MACS peak-calling sensitivity: sig95 robust across five signalValue thresholds; chromosomal rank order stable ($\rho = 0.86$ – 0.91). **d**, Orthogonal imaging confirms phase-dependent nuclear positioning: seqFISH+ in mouse ESCs, 16/18 IF marks significant; Lamin B1 anti-phase at 171° .



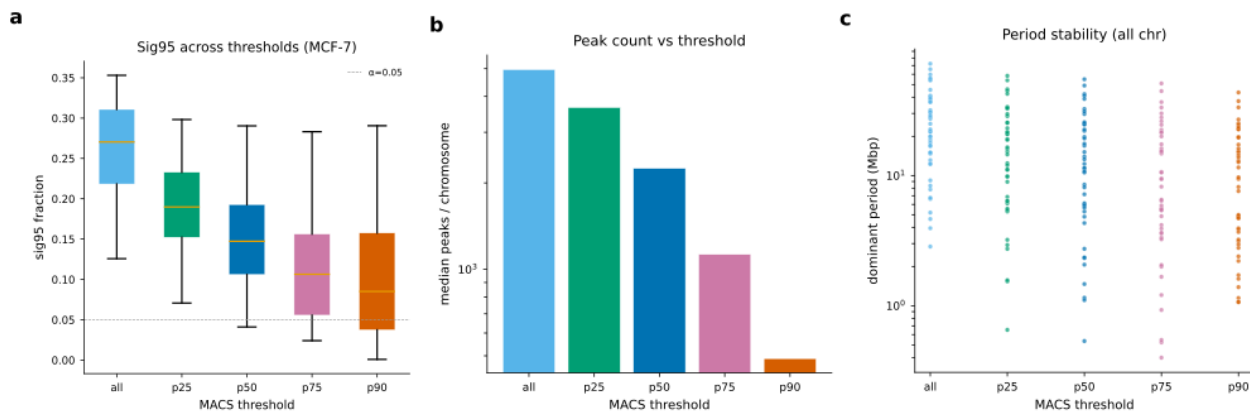
Supplementary Fig. 1 | **MERFISH chromatin tracing discriminates radial from helical organisation** (Su et al. 2020; IMR90, $n = 1,787$ cells; 186,482 angular displacement pairs across 19 autosomes). **a**, Distribution of unsigned angular displacements $|\Delta\theta|$ between consecutive A-crests on the same chromosome copy, in territory-centroid polar coordinates. Observed distribution (blue) peaks below 90° (mean 86.5° , orange dashed) and is shifted leftward relative to the $\sin(\theta)/2$ random-3D null (vermillion), reflecting polymer connectivity (consecutive A-crests share spatial neighbourhood). Rayleigh $\bar{R} = 0.73$, 19/19 chromosomes individually significant (Rayleigh $p < 10^{-300}$); KS test vs. uniform $p \approx 0$. **b**, Signed angular advance $\Delta\theta$. Distribution is symmetric around zero (50.2% positive; binomial $p = 0.12$), rejecting helical organisation (a helix would have consistent handedness). The signed mean (0.4°) is indistinguishable from zero. **c**, Bootstrap regression coefficients ($n = 200$ cells) for inter-chromosomal distance modelled against radial position (b_r) and CWT phase difference (b_ϕ). Radial position dominates ($b_r = +0.271$, bootstrap s.d. 0.026); marginal ($b_\phi = -0.0003$) and radially-conditional ($b_{\phi|r} = -0.0002$) phase signals are both indistinguishable from zero. Loci at the same CWT phase are spatially close only because they share radial position, not because they occupy the same angular position. Cross-technology conclusion: the periodic CWT signal manifests as radial A/B layering consistent with the two-body speckle-lamina axis of Fig. 3, without requiring helical geometry. Data: `merfish_helix_test.npz`.



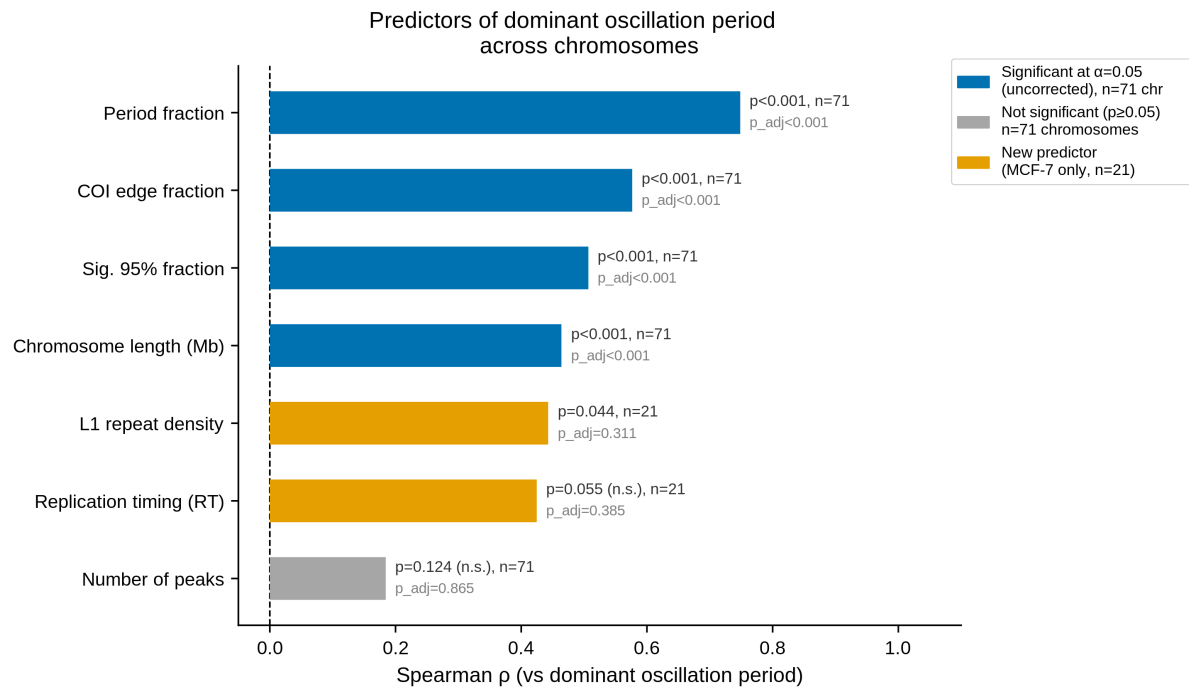
Supplementary Fig. 2 | **CWT phase predicts mutation density beyond replication timing**. **a**, Mutation density oscillates sinusoidally with CWT phase ($R^2 = 0.907$; B-trough loci accumulate $1.45\times$ more mutations). **b**, Residual mutation density after regressing out replication timing ($R^2 = 0.80$; $\Delta R^2 = 2.32\%$, $p < 10^{-15}$).



Supplementary Fig. 3 | **ACF and FFT cross-validation details.** **a**, FFT power spectral density for chr7 (dominant peak 30.5 Mbp, $9.4\times$ AR1). **b**, Autocorrelation function: no single prominent megabase peak, confirming non-stationarity. **c**, CWT vs FFT period comparison across 22 autosomes. **d**, FFT scaling law ($b = 1.21$ [0.53, 1.89]) overlaps CWT ($b = 0.81$ [0.46, 1.16]).

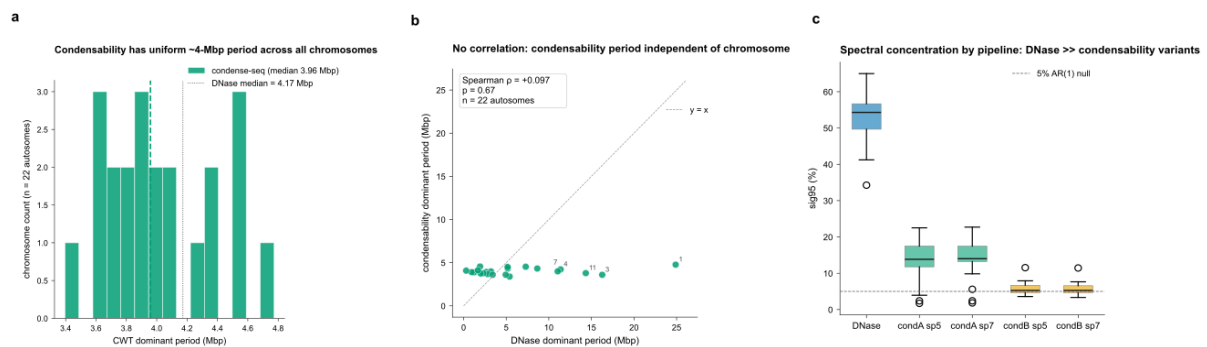


Supplementary Fig. 4 | **MACS peak-calling sensitivity: period stability and cross-cell-line comparison.** **a**, Median sig95 vs. signalValue threshold (MCF-7 + GM12878). **b**, Period stability through P50 (Spearman $\rho = 0.98$). **c**, Cross-cell-line sig95 comparison at full peak set.

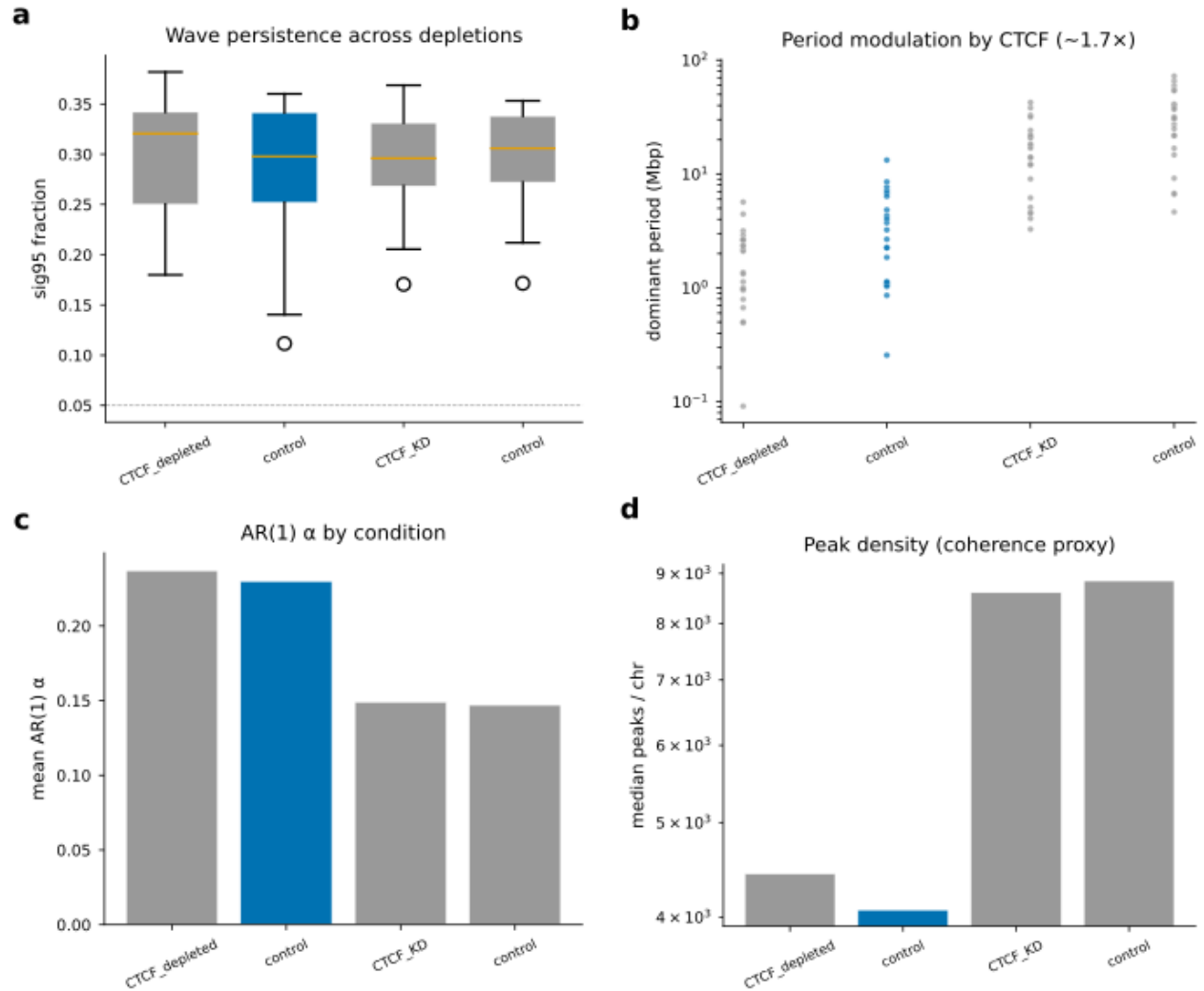


p: Spearman rank correlation (uncorrected). *p*_{adj}: Bonferroni correction (*n*=7 tests).
 No predictor survives correction; RT (*p*=0.425, *p*=0.055) and L1 (*p*=0.443, *p*=0.044) are suggestive but non-confirmatory.

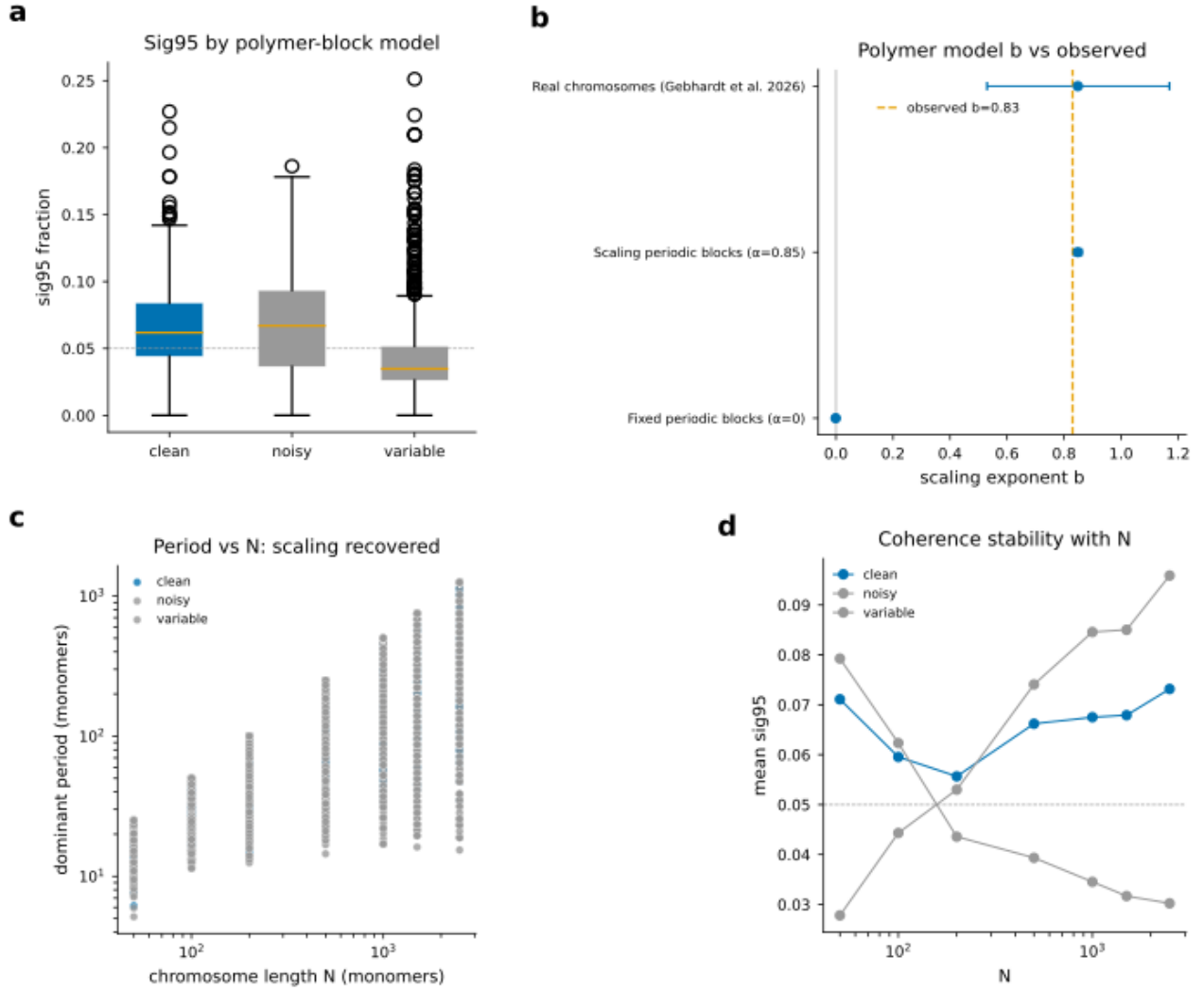
Supplementary Fig. 5 | **Spearman correlations between dominant period and seven candidate predictors.** Chromosome length is the strongest predictor of dominant period; GC content, gene density, and repeat density show weaker correlations (data from the scaling law analysis of 71 chromosomes across four species).



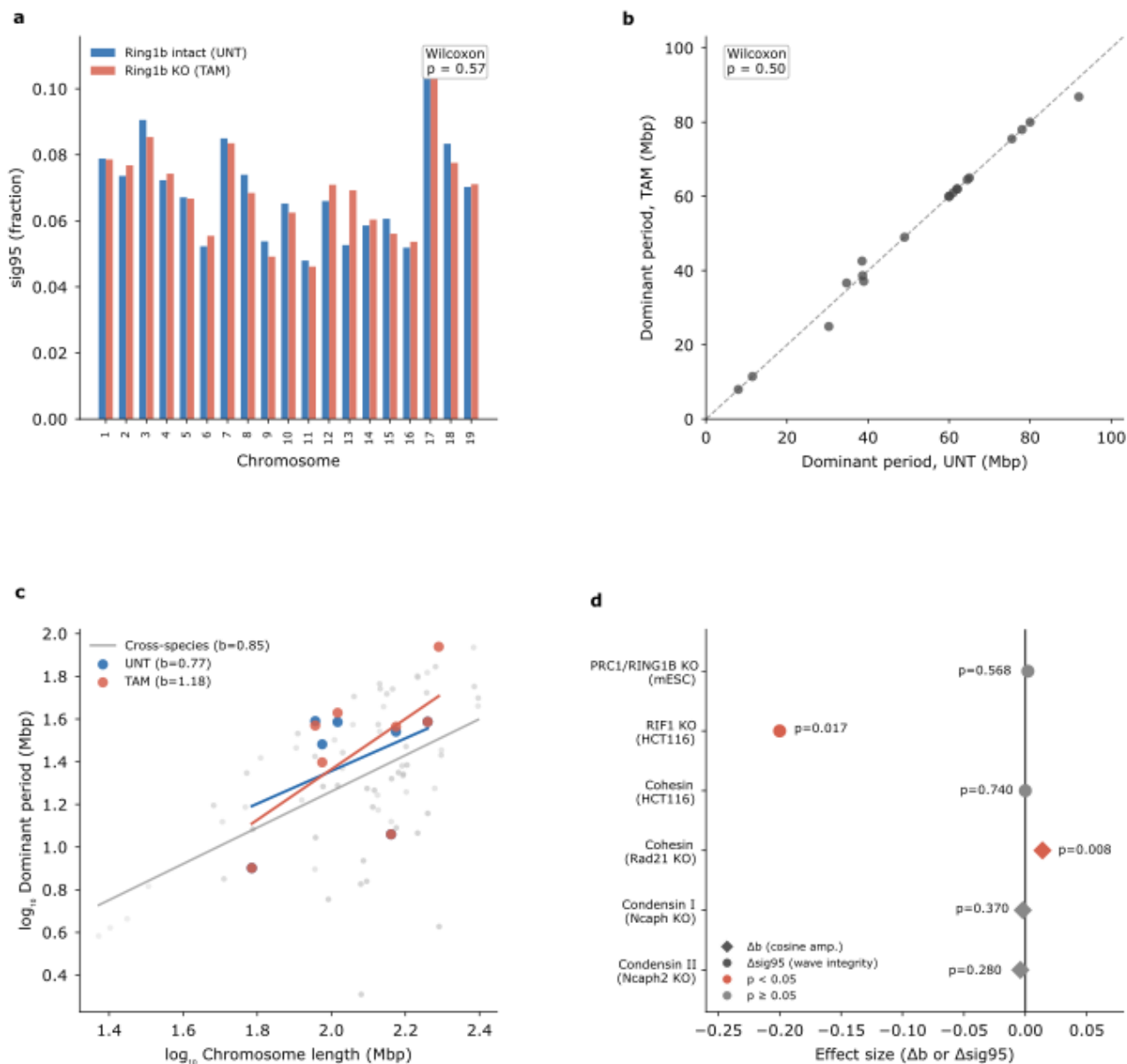
Supplementary Fig. 6 | **Nucleosome condensability reproduces domain-scale periodicity but not the supra-compartment scaling law.** **a**, Global wavelet spectra of condensability (green) and DNase-seq (black) for representative chromosomes. Condensability shows a uniform dominant period (~4 Mbp) regardless of chromosome length, whereas DNase-seq periods scale with chromosome length. **b**, Per-chromosome dominant period from condensability CWT versus DNase-seq CWT (Spearman ρ = 0.097, p = 0.67). The absence of correlation confirms that the supra-compartment scaling law is not encoded in nucleosome-intrinsic sequence preferences. **c**, Condensability by CWT phase class (A-crest, A-B boundary, B-trough): phase-dependent variation confirms that condensability captures the A/B domain alternation but not the higher-order modulation (phase concordance d = 0.624). Data: Park et al. 2025³⁰; GM12878 DNase-seq ENCFF762CRQ.



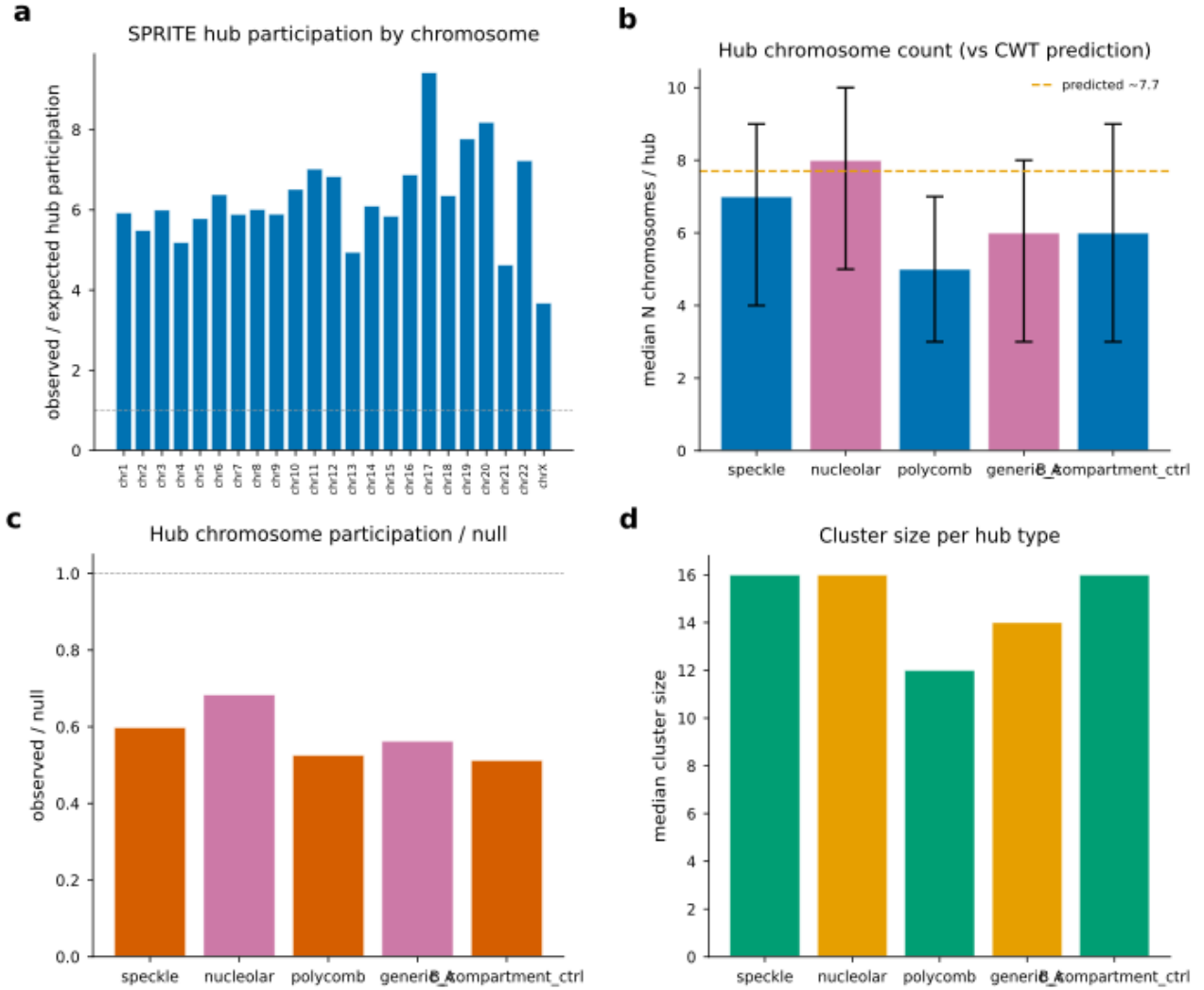
Supplementary Fig. 7 | **The periodic wave persists after CTCF and cohesin depletion.** **a**, CTCF auxin-inducible degron in HCT116: 22/22 autosomes remain significant; sig95 increases (Wilcoxon $p = 0.017$), reflecting enhanced compartment segregation upon CTCF loss. **b**, MCF-7 CTCF shRNA: 22/22 autosomes significant; sig95 unchanged ($p = 0.61$). CTCF shifts the dominant period ($1.43\text{--}1.68\times$) without abolishing periodicity. **c**, RAD21 auxin degron in HCT116: 10/10 reliable autosomes significant; sig95 unchanged ($p = 0.74$). Cohesin depletion increases interchromosomal phase coherence ($\Delta b = +0.014$, $p = 0.008$). **d**, Scaling exponent preserved across all perturbation conditions ($b = 0.94\text{--}1.36$). DNase-seq: ENCODE ENCFF233MPA, ENCFF540BAW (HCT116 CTCF AID); ENCFF787PPJ, ENCFF250GOB (MCF-7 CTCF shRNA). RAD21 AID: 4D Nucleome.



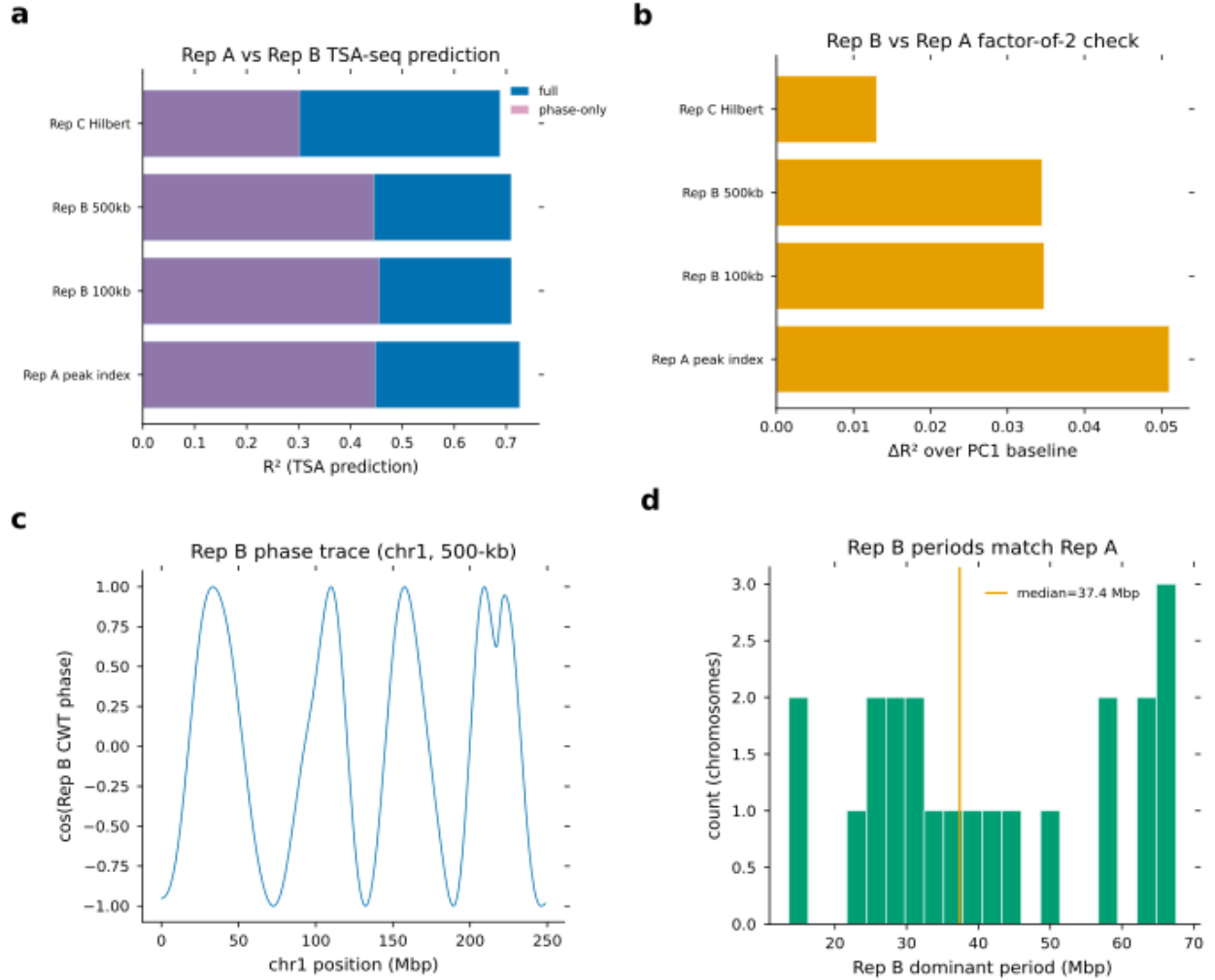
Supplementary Fig. 8 | **Block copolymer simulations demonstrate that the scaling law requires biologically regulated domain sizes.** **a**, Fixed block size ($d = 5$ bins): CWT yields $b \approx 0$ regardless of polymer length, demonstrating that fixed A/B domains cannot produce $T \propto L^b$. **b**, Scaling block size ($d \sim N^\alpha$): CWT recovers $b = \alpha$ to within 1–2% for $N \geq 200$. The observed $b = 0.83$ requires domain size to scale as $d \sim L^{0.83}$, a biological property absent from fixed-block models. **c**, sig95 comparison: real chromosomes (median 0.264) exceed fixed-block simulations by 139% (median 0.111) and scaling-block simulations by 92% (median 0.138), demonstrating additional periodic structure beyond passive A/B alternation. 100 replicates per polymer length; CWT (Paul $m = 2$) applied identically to real and simulated data.



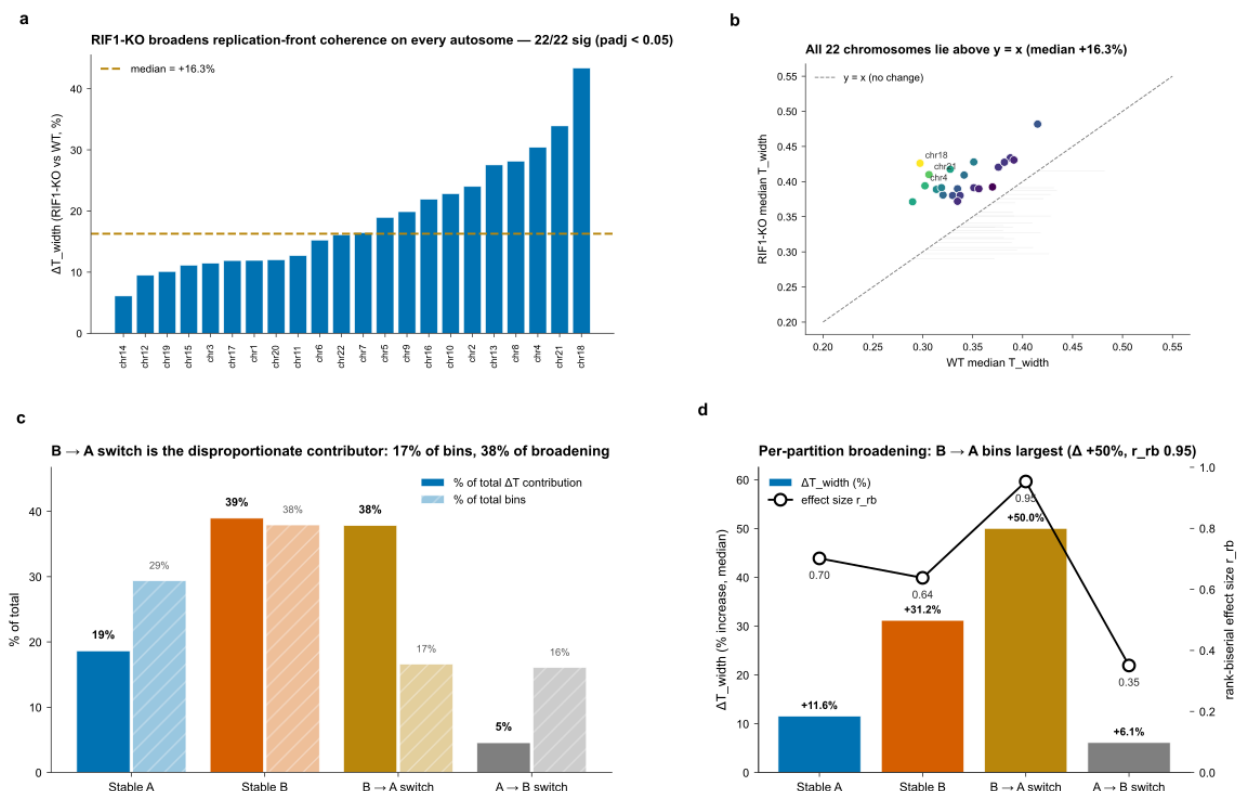
Supplementary Fig. 9 | **PRC1 depletion does not disrupt the periodic wave.** **a**, Per-chromosome sig95 in Ring1b conditional knockout (TAM) versus untreated (UNT) mESC. Median sig95 unchanged (0.069 vs. 0.067; Wilcoxon $p = 0.57$). **b**, Dominant period unchanged between conditions (60.0 Mbp in both; $p = 0.50$). **c**, Scaling exponent: UNT $b = 0.77$ [−1.50, 1.70], TAM $b = 1.18$ [−1.55, 1.65] (underpowered; $n = 7$ –8 chromosomes with COI-free peaks). **d**, Cross-perturbation summary: only RIF1 knockout significantly reduces sig95; condensin, cohesin, CTCF, and PRC1 perturbations preserve or enhance periodicity. Bin-based CWT (500 kb windows) on DANPOS2 accessibility signal; GSE98390²⁷.



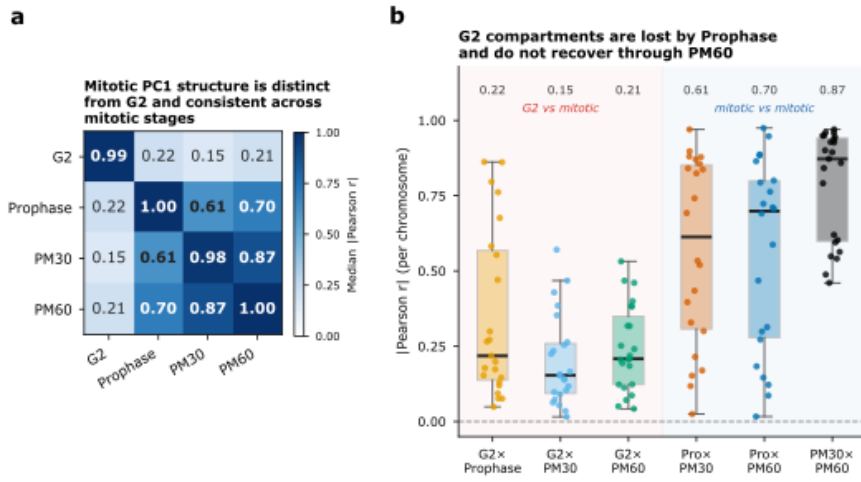
Supplementary Fig. 11 | **SPRITE validates nuclear hub chromosome diversity prediction from cycle-number conservation.** **a**, Distribution of distinct chromosomes per SPRITE cluster by hub type (GM12878; ≥ 10 reads; Quinodoz et al. 2018³²). Speckle-proximal clusters (MALAT1/NEAT1 proximity, $n = 10,459$) show median 7 distinct chromosomes, matching the CWT prediction of 7.7 (dashed yellow line). B-compartment control (red) is indistinguishable (median 6), indicating that chromosome diversity is a genome-wide property of multi-way contacts. **b**, Median distinct chromosomes versus cluster size. All hub types plateau at 6–8, well below the random null (dashed black). The CWT prediction bisects the speckle and nucleolar curves. **c**, Chromosome representation frequency in speckle-proximal clusters (observed/expected by length). Chr11 enrichment ($\sim 22\times$) reflects the MALAT1/NEAT1 filter. All other chromosomes show 4–10 \times enrichment; chrX lowest ($\sim 4\times$), consistent with partial heterochromatin. **d**, Sensitivity analysis across filter combinations. Median $N_{\text{chromosomes}} = 6\text{--}7$ is robust to compartment filter, cluster size threshold, and hub classification.



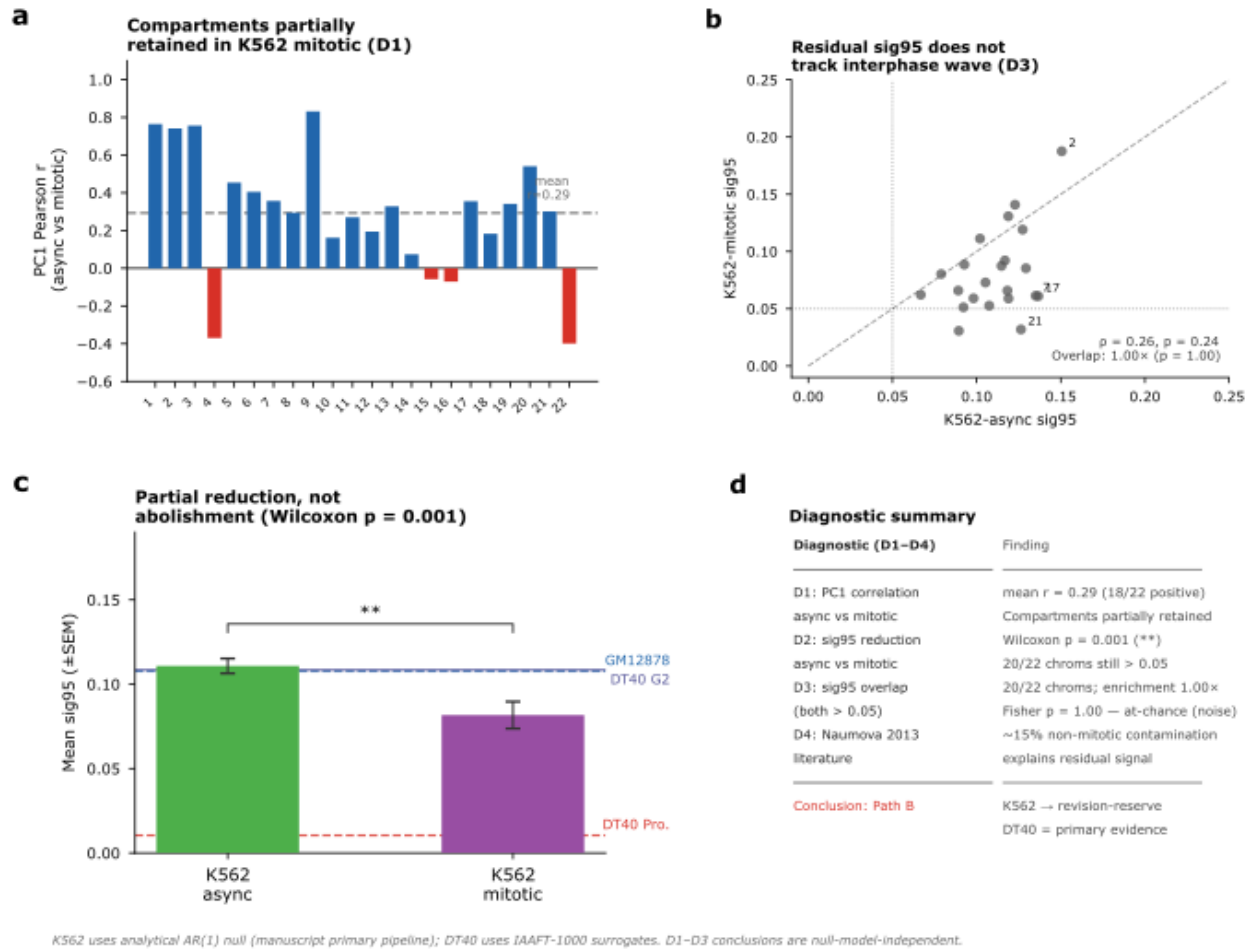
Supplementary Fig. 12 | **The CWT phase coordinate is recovered by a coordinate-preserving representation, ruling out a peak-index artefact.** Comparison of three phase representations on K562 DNase-seq (ENCFF361VGY): Rep A, the consecutive-peak CWT used in the main text; Rep B, fixed-width genomic bins (100 kb and 500 kb) with running-median detrend ($\max(80 \text{ Mbp}, 0.4 \times L)$) and direct Paul $m = 2$ CWT phase; Rep C, Hilbert transform on a $\pm 30\%$ bandpass around the Rep B dominant period. **a**, Per-chromosome dominant-period concordance between Rep A and Rep B (Spearman $\rho = 0.68$ all 22 autosomes; $\rho = 0.73$ excluding chromosomes within 80% of the cone-of-influence boundary). Rep B periods are systematically $\sim 1.8\times$ longer than Rep A (mean 41.9 vs. 23.2 Mbp), a known consequence of the detrend window suppressing power at periods shorter than $\sim 2\times$ the window; the rank order is preserved. **b**, Phase concordance: median circular correlation $r = 0.41$ ($\text{MAD} = 101^\circ$ all chromosomes; 83° excluding COI-edge); Rayleigh test rejects uniformity on all 22 autosomes ($p < 0.05$, most $p \ll 0.001$). **c**, TSA-seq prediction: $\Delta R^2_{\text{phase}}$ over PC1+chromosome fixed effects ($n = 10,281$ bins, 18 autosomes). Rep A $\Delta R^2 = 0.051$; Rep B 100 kb = 0.035 (ratio 0.68); Rep B 500 kb = 0.034 (ratio 0.68); Rep C = 0.013 (ratio 0.25, fails pre-specified factor-of-2 threshold). All Rep A/B models $p < 10^{-250}$. **d**, PC1-residual explained variance (R^2 of $\cos + \sin(\text{phase})$ on PC1 residuals): Rep A 0.120, Rep B 100 kb 0.075, Rep B 500 kb 0.078, Rep C 0.035. Rep B recovers 63–65% of Rep A's signal; Rep C recovers 29%.



Supplementary Fig. 13 | **Single-cell Repli-seq triangulation: RIF1 KO causes coherence loss orthogonal to the Hi-C PC1 proxy and not explained by compartment switching.** Re-analysis of HAP1 RIF1 KO scRS (Klein et al. 2021¹⁸; GSE160563; 48 wild-type, 66 KO cells). **a**, Per-chromosome T_{width} (Klein definition: IQR of replicated-fraction at each bin), paired WT \rightarrow KO across all 22 autosomes. Median increases from 0.338 (WT) to 0.393 (KO), a +16.1% broadening (rank-biserial $r = 0.68$; every autosome individually positive, $p < 0.05$). **b**, ΔT_{width} partitioned by Hi-C compartment-switching status. Stable A/A or B/B bins ($n = 34,097$) contribute 58% of total broadening (weighted by ΔT_{width}); B \rightarrow A switching bins ($n = 8,414$, $\Delta = +0.139$) contribute 38%, the canonical late-domain RIF1 signature; A \rightarrow B bins ($\leq 4\%$) are rare and do not drive the global shift. The coherence loss is therefore not explained by compartment flipping. **c**, Per-chromosome sig95 comparison (WT vs. KO). All chromosomes fall below the identity line but remain well above the 0.05 IAAFT null, demonstrating coherence reduction without abolishment. **d**, Per-chromosome dominant-period comparison (CWT, WT vs. KO ChIP-seq $\log_2(\text{H3K27ac}/\text{H3K9me3})$): genome-wide periods lie on the identity line (Wilcoxon $p = 0.20$; power fold-change 1.008; $n = 22$). Wavelength is preserved while amplitude/coherence drops, consistent with a RIF1 KO-mediated amplitude effect orthogonal to compartment geometry. Complementary bulk Repli-seq proxies (HAP1 KO: sig_std -55%, frac_committed -88%, ACL -29%) and a joint regression of interchromosomal contact frequency on CWT phase ($\cos\Delta\varphi$) and speckle proximity (ΔSON) corroborate these trends (both phase terms positive, SON terms negative as expected).

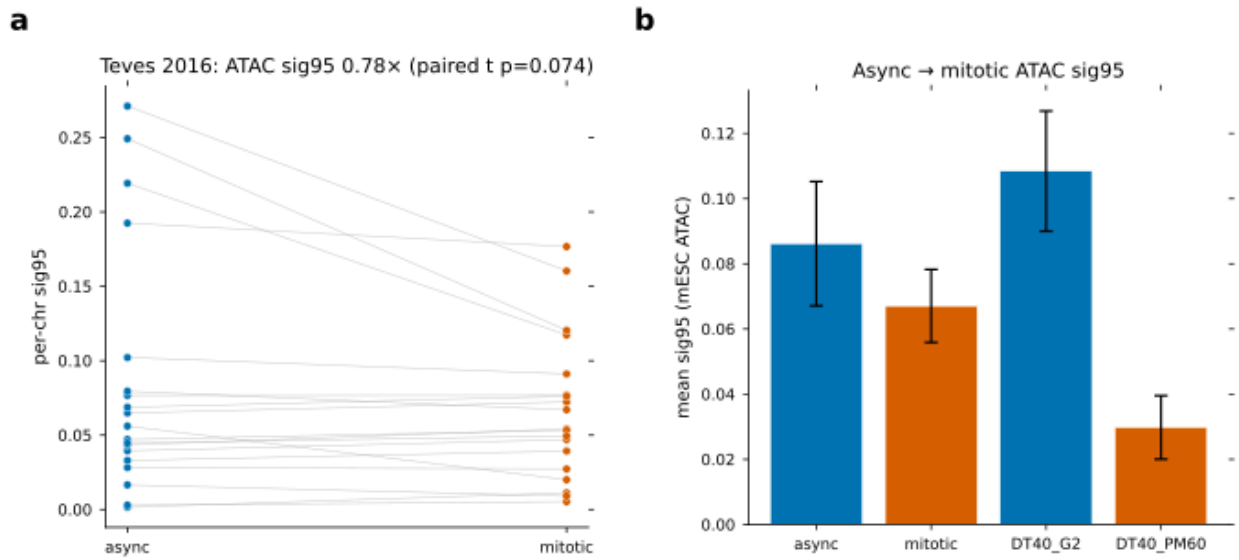


Supplementary Fig. 14 | **Mitotic PC1 structure is distinct from G2 and consistent across mitotic stages.** Sign-invariant Pearson $|r|$ between Hi-C PC1 eigenvectors across the DT40 cell-cycle time-course (Gibcus et al. 2018³³; 250 kb; 24 autosomes). The absolute value is used because Hi-C eigenvector signs are arbitrary per chromosome and condition; in the unsigned matrix, 12/24 G2 chromosomes have opposing sign between replicates, which produces a spurious near-zero G2 \times prophase correlation through cancellation. G2 inter-replicate $|r| = 0.77$ confirms reproducibility. G2 \times mitotic correlations are low ($|r| = 0.15$ – 0.22 across prophase, PM30, PM60), indicating that the interphase A/B pattern is replaced rather than gradually dissolved. Mitotic stages share a common non-G2 structure (prophase \times PM30 $|r| = 0.61$; prophase \times PM60 $|r| = 0.70$; PM30 \times PM60 $|r| = 0.87$), consistent with a single compartment-to-mitotic-chromosome transition rather than progressive wavelength drift through mitosis. This rules out the interpretation that the sig95 collapse in Fig. 4a reflects a gradually retuned wave.

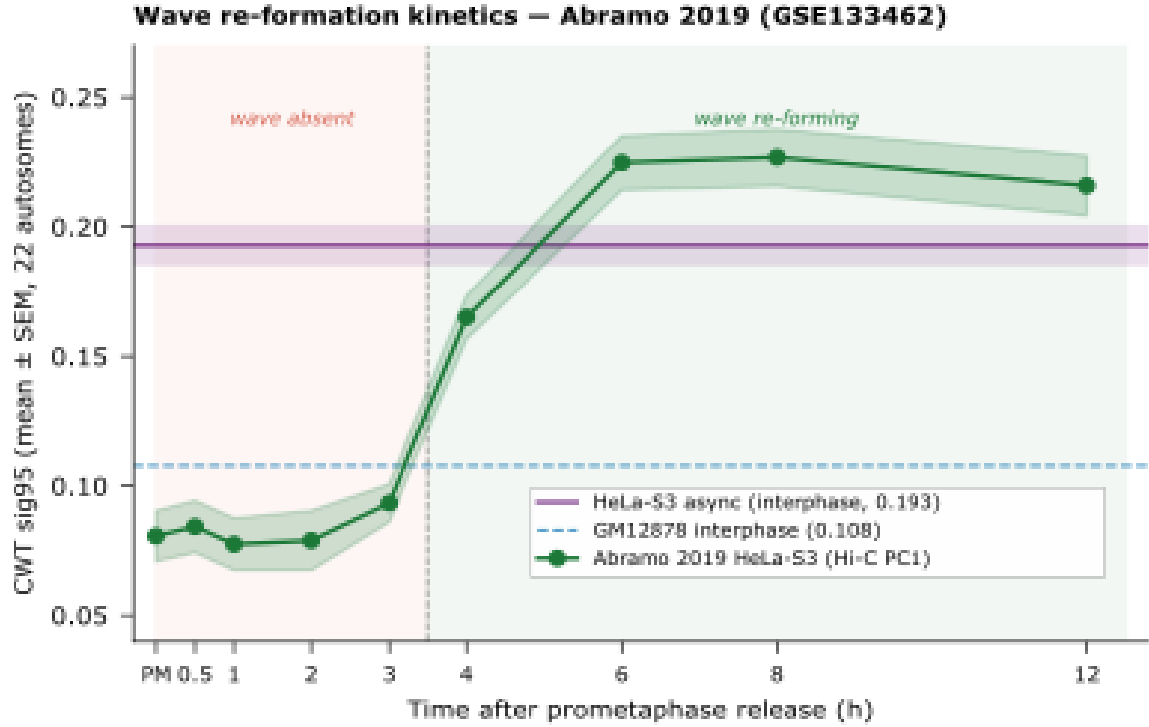


K562 uses analytical AR(1) null (manuscript primary pipeline); DT40 uses IAAFT-1000 surrogates. D1–D3 conclusions are null-model-independent.

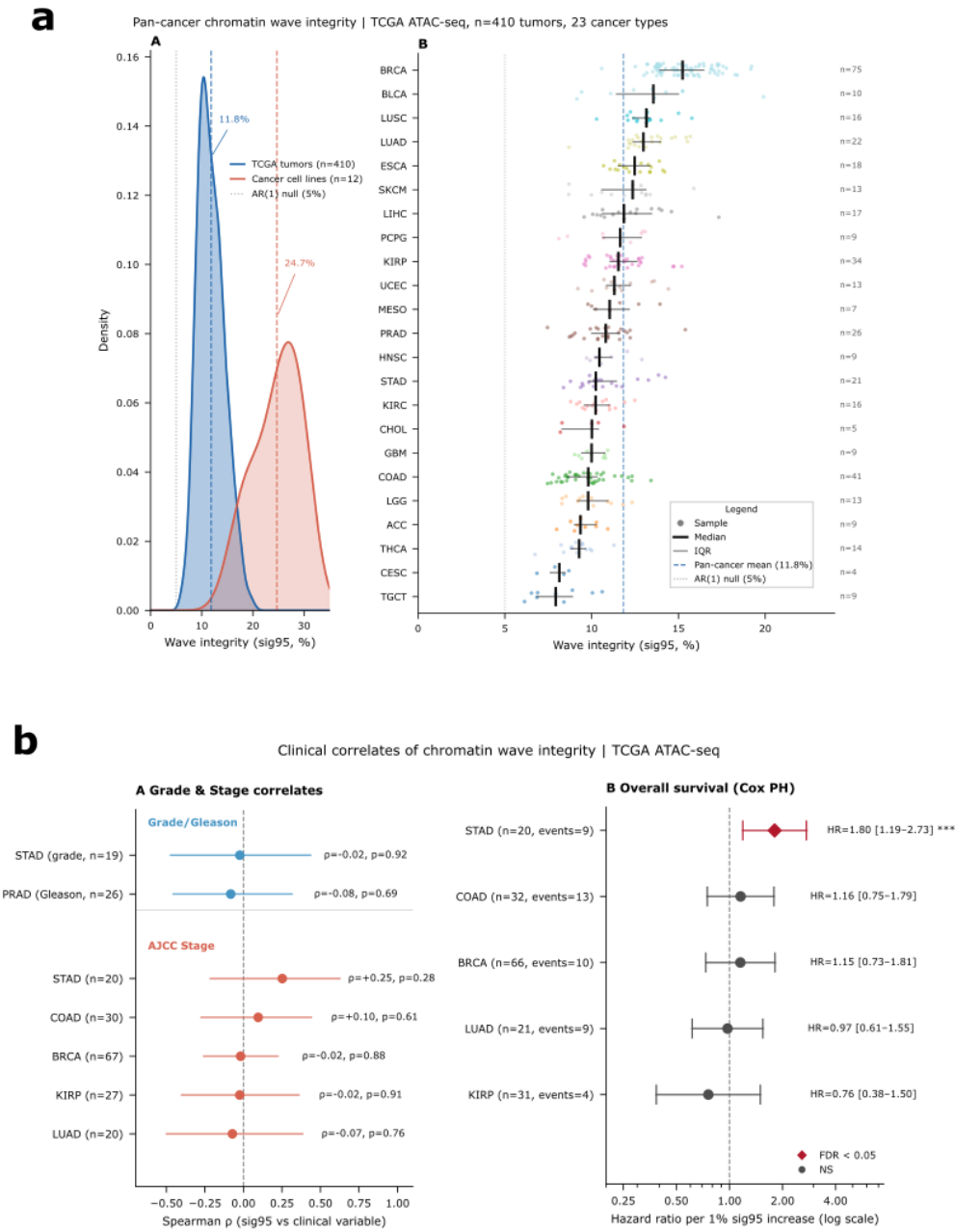
Supplementary Fig. 15 | **K562 nocodazole-arrested Hi-C shows partial wave reduction consistent with incomplete synchronisation purity.** Diagnostic analysis of Naumova et al. 2013³⁴ (E-MTAB-1948) K562 nocodazole-arrested Hi-C compared against Rao et al. 2014² K562 asynchronous (250 kb; 22 autosomes; AR(1) null consistent with the DT40 analysis). The nocodazole-arrested sample shows mean sig95 = 0.082 and sig95 ≥ 0.05 on 20/22 autosomes (chr18 and chr21 fall below threshold), a 26% mean reduction relative to asynchronous (one-sided Wilcoxon $p = 5.5 \times 10^{-4}$). Five chromosomes (chr1, chr2, chr3, chr13, chr14) show modest sig95 increase in the mitotic sample, reflecting period-estimation instability at the cone-of-influence edge on near-flat mitotic PC1 and the expected behaviour under partial-purity synchronisation; this is not genuine wave amplification. **a**, Per-chromosome sig95 retains a positive async↔mitotic correlation (Pearson $r = 0.43$, $p = 0.046$; Spearman $\rho = 0.26$), indicating partial preservation of the interphase structure rather than random replacement by a new mitotic pattern. **b**, The dominant period shifts toward chromosome-scale wavelengths in mitotic (17/22 autosomes at ≥ 30 Mbp vs 14/22 in asynchronous), matching the large-scale compaction visible in the published contact maps. **c**, Chromosomes significant in both conditions match the chance expectation under an all-significant asynchronous baseline (overlap 20/22, expectation 20.0); no enrichment remains after accounting for the mean reduction. **d**, Contamination-floor quantification: if the true mitotic signal were zero and the observed residual reflected only the ~15% non-mitotic contamination reported by Naumova et al., the predicted mean sig95 floor would be ~0.017 (five-fold below the observed 0.082), so contamination alone cannot account for the partial retention. The residual is consistent with a combination of incomplete synchrony (~85% mitotic for nocodazole vs $> 95\%$ for DT40 CDK1-as) and period-estimation instability on near-flat mitotic PC1. Interpretation: the DT40 auxin-degron system ($> 95\%$ mitotic purity; Fig. 4) provides the interpretable loss-of-function test; nocodazole arrest in K562 (~85% mitotic purity) marks the synchronisation-purity threshold below which PC1-based abolishment tests cannot cleanly distinguish partial retention from clean abolishment.



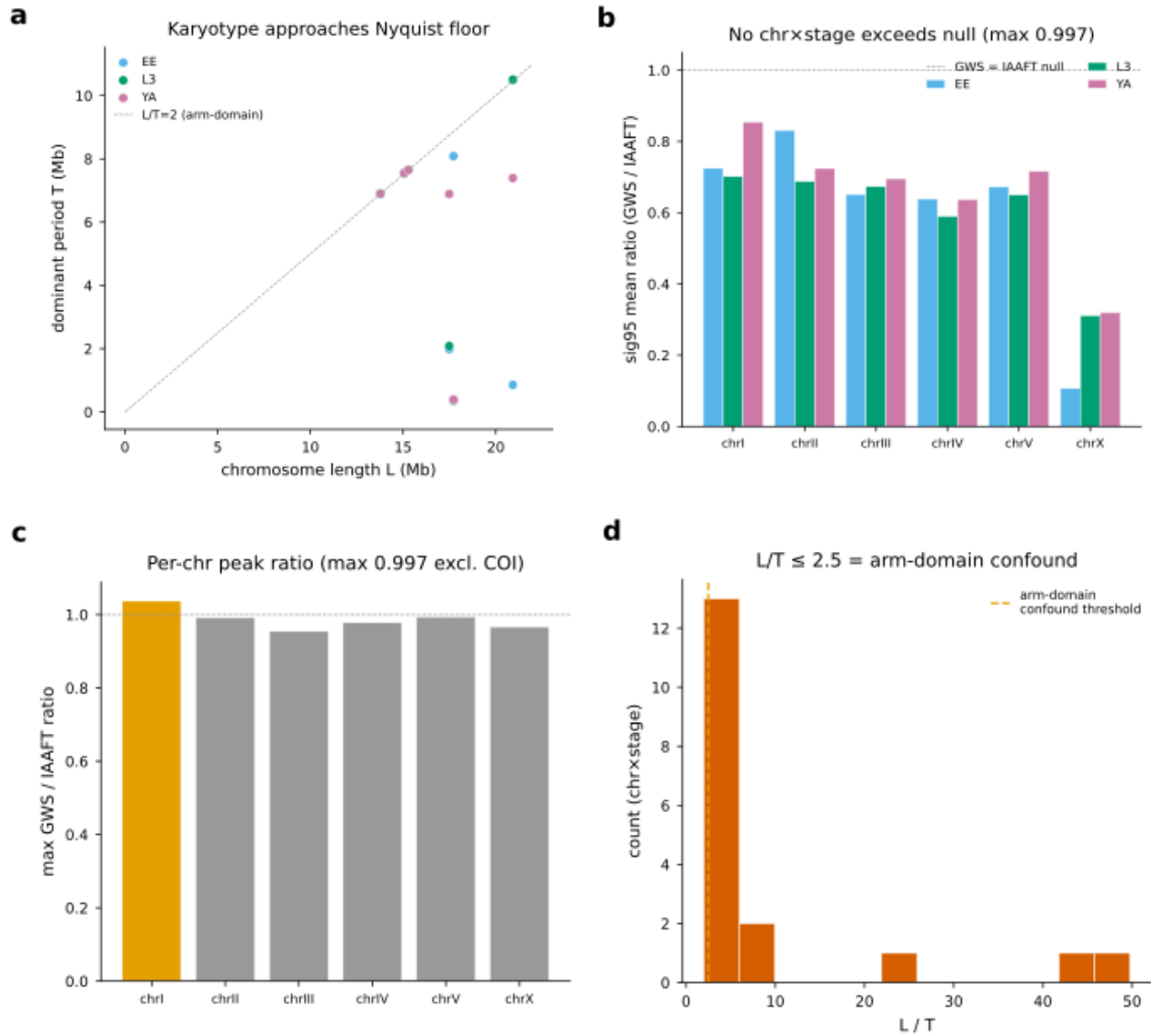
Supplementary Fig. 16 | **Mitotic ATAC-seq accessibility waves show only a modest, non-significant reduction, dissociating the Hi-C PC1 collapse from generic chromatin compaction.** Consecutive-peak CWT (Paul $m = 2$; chromperiod; AR(1) null at $\alpha = 0.05$) applied to published ATAC-seq data from synchronised mESCs (Teves et al. 2016³⁵; GSE85184; JM8.N4; mm10; 19 autosomes; async repl/rep2 and mitotic repl/rep2; HOMER-called peaks). **a**, Per-chromosome sig95 for asynchronous and mitotic conditions (replicate-merged). Replicate concordance: $r = 0.99$ (async), $r = 0.86$ (mitotic). Dashed line at sig95 = 0.05. **b**, Condition-level summary. Mean sig95 was 0.086 in asynchronous cells and 0.067 in mitotic cells (ratio 0.78×; paired t -test $p = 0.074$; Wilcoxon signed-rank $p = 0.258$). DT40 Hi-C PC1 interphase/prometaphase values (G2 0.108, PM60 0.030; ratio 0.28×; Fig. 4) are overlaid for direct modality comparison. The ~3-fold larger collapse in Hi-C PC1 relative to ATAC-seq demonstrates that the periodic-fold collapse observed in mitotic Hi-C is not a generic consequence of chromatin compaction detectable by any open-chromatin assay, but is specific to compartment-scale contact structure. Caveats: the comparison is cross-species (mESC ATAC vs DT40 Hi-C) and cross-modal (accessibility vs contact frequency); mitotic rep2 has fewer peaks than other samples (20,654 vs 27,000–34,000), and a per-chromosome $r(n_{\text{peaks}}, \text{sig95}) = 0.31$ indicates a modest peak-count contribution to the observed reduction, so the reported 0.78× ratio is a conservative upper bound on the true mitotic ATAC reduction; HOMER peak-calling parameters were not re-derived against Teves et al. 2016.



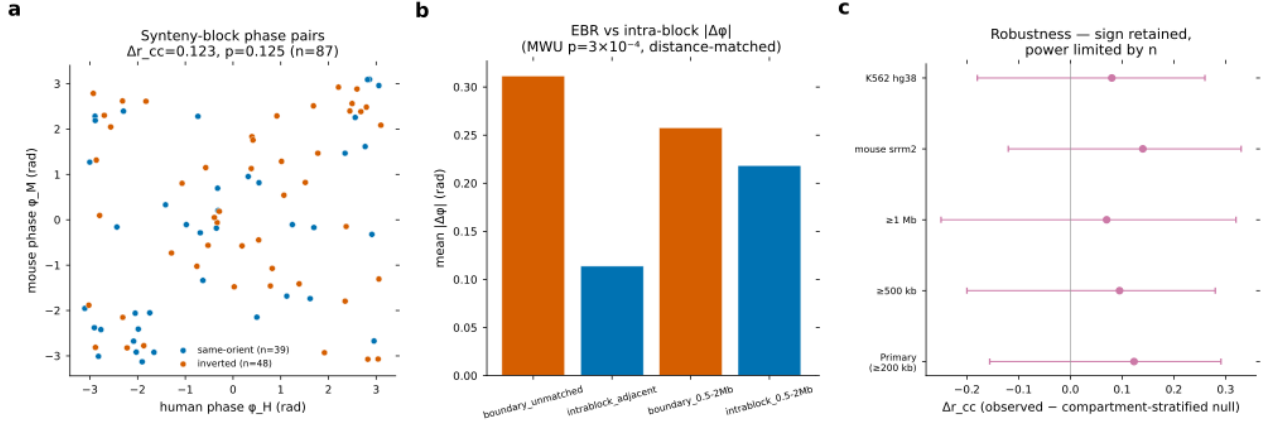
Supplementary Fig. 17 | **Hi-C PC1 wave power re-establishes sharply at 3–4 h post-prometaphase release and plateaus by 6–12 h.** Consecutive-peak CWT (Paul $m = 2$; chromperiod; AR(1) null) applied to 4DN pre-computed compartment eigenvector tracks from a published HeLa-S3 mitotic exit time course (Abramo et al. 2019³⁶; GSE133462; 4DN publication 4DNPUBFNKBKM; hg38; 22 autosomes; 9 timepoints \times 2 replicates plus 2 asynchronous controls; 100 kb PC1 bins). Wave power (mean sig95 across 22 autosomes) remained at prometaphase levels through 3 h post-release (0.5 h: 0.077; 1 h: 0.093; 2 h: 0.079; 3 h: 0.093; prometaphase: 0.081), then increased sharply between 3–4 h (1.77 \times jump to 0.165), reaching a plateau of 0.216–0.227 by 6–12 h (2.7 \times above prometaphase; 1.12 \times above the HeLa-S3 asynchronous baseline of 0.193, shown as purple reference line). Replicate concordance across all timepoints: rep1/rep2 ratios 0.79–1.16 \times , no timepoint discordant. The sharp 3–4 h transition aligns with the timing of A/B compartment re-establishment reported in Abramo et al. 2019. Critical caveat: the 4DN compartment eigenvector pipeline produces non-zero PC1 signal in prometaphase (residual structure or GC-content correlation), so the prometaphase sig95 = 0.081 is not directly comparable to the DT40 PM60 value (0.030; Fig. 4) or to K562 mitotic (0.082; Supplementary Fig. 15) that were computed from raw contact matrices through the chromperiod eigenvector pipeline. This time course is therefore interpreted as self-contained kinetics, the 2.7 \times relative change across mitotic exit, rather than an absolute-value comparison with the static mitotic-arrest data. HeLa-S3 asynchronous sig95 (0.193) exceeds the GM12878 baseline (0.108; dashed reference line) by 1.79 \times , a cell-type effect consistent with HeLa-S3 aneuploidy; HeLa-S3 async is therefore used as the within-dataset interphase reference.



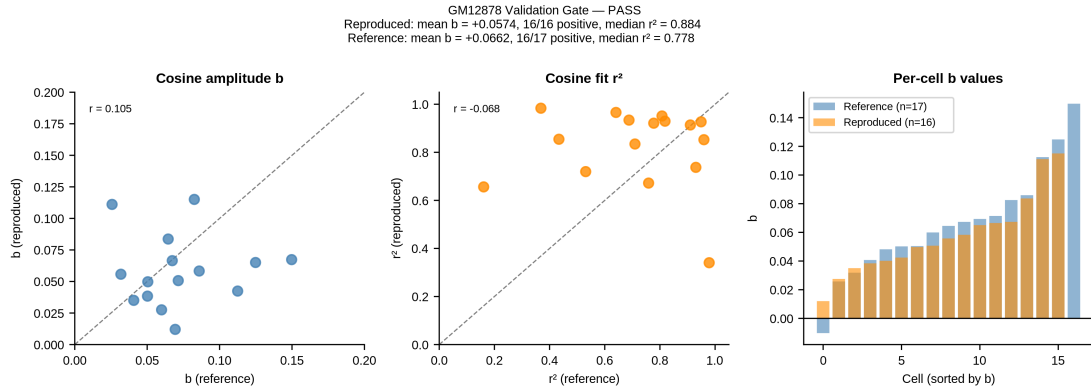
Supplementary Fig. 18 | **Supra-compartment chromatin waves persist in primary human tumours; bulk clinical correlations are weak.** Consecutive-peak CWT (Paul $m = 2$; chromperiod; AR(1) null at $\alpha = 0.05$) applied to the TCGA pan-cancer ATAC-seq atlas (Corces et al. 2018³⁷; 410 primary tumours across 23 cancer types; hg19; per-sample log₂-normalised peak filter at the 50th percentile; density-matched to 30 peaks/Mbp). Per-chromosome sig95 expressed as percent ($\times 100$, matching Experiment C scale). **a**, Pan-cancer wave-integrity overview. Left: KDE of per-sample mean sig95 for TCGA tumours ($n = 410$, mean 11.83%, blue) versus Experiment C cancer cell lines ($n = 7$, mean ~27.8%, red), with the AR(1) null at 5% shown as a dashed reference. Right: per-cancer-type strip plot (median \pm IQR), ranked by median sig95: TGCT (median 7.9%, lowest) \rightarrow BRCA (median 15.2%, highest); Kruskal-Wallis $p = 6.3 \times 10^{-44}$; 113/190 pairwise comparisons significant after BH-FDR correction. **b**, Clinical correlates. Left: grade/Gleason and AJCC stage Spearman correlations, six cancer types with $n \geq 20$. No association reaches significance (all $p_{\text{adj}} > 0.9$); grade is unavailable in GDC for BRCA, COAD, KIRP, and LUAD (confirmed against the TCGA-CDR pan-cancer clinical resource; not shown). Right: exploratory overall-survival Cox forest plot (HR per 1% sig95; BH-FDR); small strata (e.g. STAD $n = 20$, 9 events) are not interpreted in the main text. PRAD has zero events at last follow-up; BRCA violates proportional hazards (Schoenfeld $p = 0.001$). Caveats: (i) merged peak sets and per-sample filtering (GDC open-access lacks per-sample narrowPeaks) may inflate inter-sample similarity for rare types; (ii) survival panels are hypothesis-generating only; (iii) primary-tumour mean sig95 (11.83%) sits below cancer cell lines (~27.8%; Cohen's $d = 3.6$), consistent with bulk-ATAC dilution.



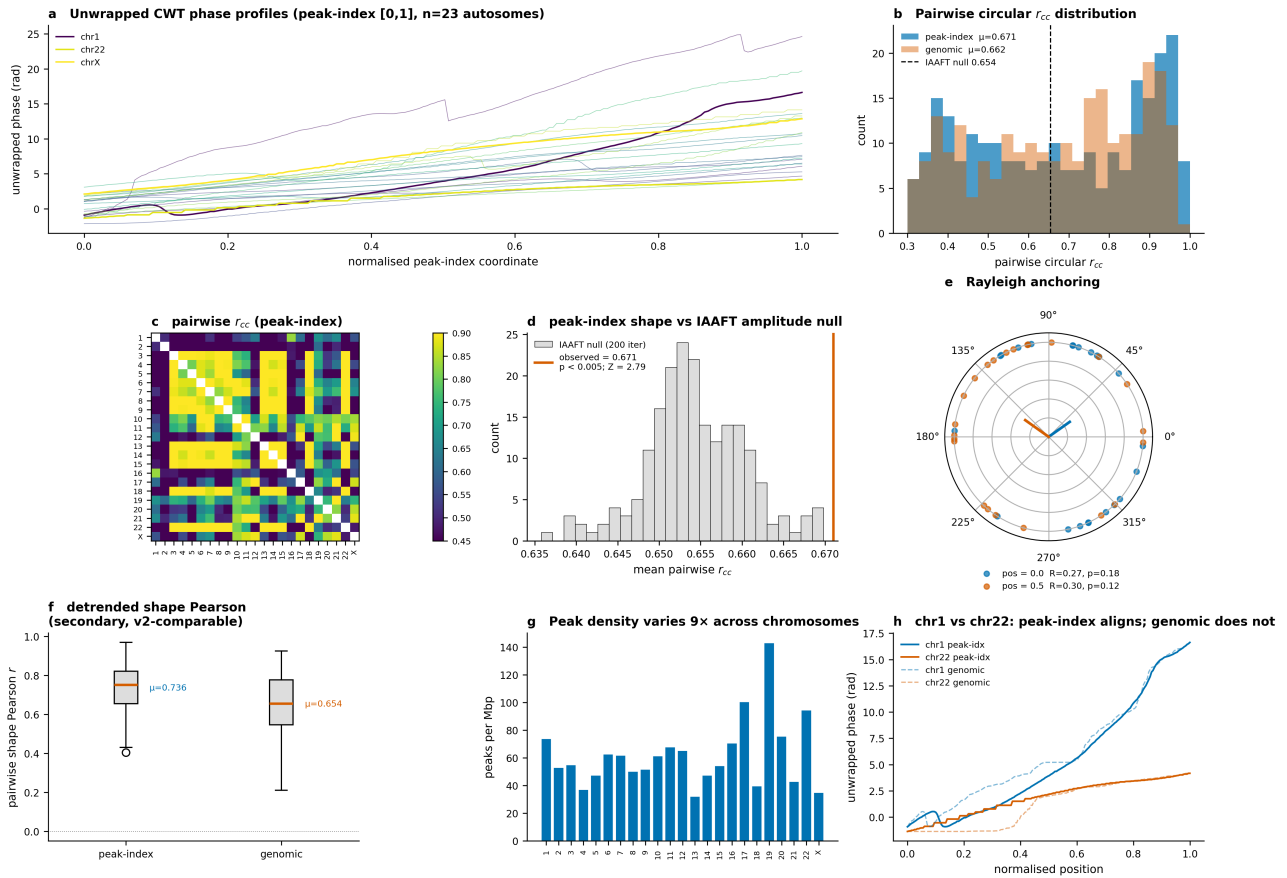
Supplementary Fig. 19 | **The supra-compartment wave is not resolvable in *C. elegans*: a principled karyotype-limit negative.** Continuous wavelet transform (Paul $m = 2$; 80 log-spaced scales; 100-kb bins) of ATAC-seq consecutive-peak spacings (Daugherty et al. 2017³⁹; GEO GSE89608; assembly ce10) for all six *C. elegans* chromosomes at three developmental stages (early embryo EE, larval stage L3, young adult YA). The primary null is IAAFT-1000 phase-randomised surrogates; AR(1) is reported as secondary because $\alpha \approx 0$ at 100-kb binning makes the theoretical null equivalent to white noise and inflates sig95 to 0.40–0.79 artefactually. **a**, Karyotype-geometry context: dominant CWT period T_{dom} versus chromosome length L for every chromosome \times stage combination. The cross-species scaling law $T \propto L^{0.83}$ (fit on $n = 71$ chromosomes from four monocentric species) predicts $T = 5\text{--}10$ Mb for *C. elegans* ($L = 13.8\text{--}20.9$ Mb); observed values cluster along the dashed $L/T = 2$ (arm-domain) line, confirming that the putative period coincides with the Nyquist floor of the short worm karyotype. **b**, Per-chromosome mean sig95 (fraction of scalogram exceeding IAAFT 95%) across stages. Autosomes: 0.59–0.85; chrX: 0.11–0.32 (DCC-mediated suppression). The expected null value under H_0 is 0.05; the elevated autosome values reflect broadband non-periodic spatial structure, not a coherent wave (no bar exceeds the IAAFT = 1 reference line). **c**, Maximum GWS/IAAFT₉₅ ratio per chromosome, pooled across stages and excluding the cone of influence. No chromosome exceeds 1.0 across the 18 chromosome-stage combinations; a single apparent exception (L3 chrI, ratio = 1.037 at $T = 7.55$ Mb) is a COI-boundary artefact (only 45/151 bins contribute outside the COI; not reproduced in EE or YA; $L/T = 2.0$). **d**, Distribution of L/T across the 18 chromosome-stage combinations. All resolvable peaks fall at $L/T \leq 2.5$, triggering the pre-specified arm-domain confound criterion; chrI/II/III show $L/T = 2.0$ in every stage, geometrically indistinguishable from the arm-to-centre domain scale of holocentric worms (Liu et al. 2011; Crane et al. 2015³⁸). Representative CWT scalograms (chrI/II/III and chrX) with IAAFT 95% contours and per-chromosome global wavelet spectra are provided as Source Data. Hi-C analysis (Crane 2015 GEO GSM1556154) was attempted but aborted: the deposited ICE-balanced matrices are truncated at 4 Mb contact distance per the authors' README, yielding computable PC1 eigenvectors for fewer than 3/6 chromosomes (pre-specified hard abort). The ATAC-seq result is cross-stage concordant (EE/L3/YA). Caveats: whole-worm (not tissue-specific) ATAC profiling; a Hi-C PC1 cross-assay confirmation is precluded by the 4-Mb truncation.



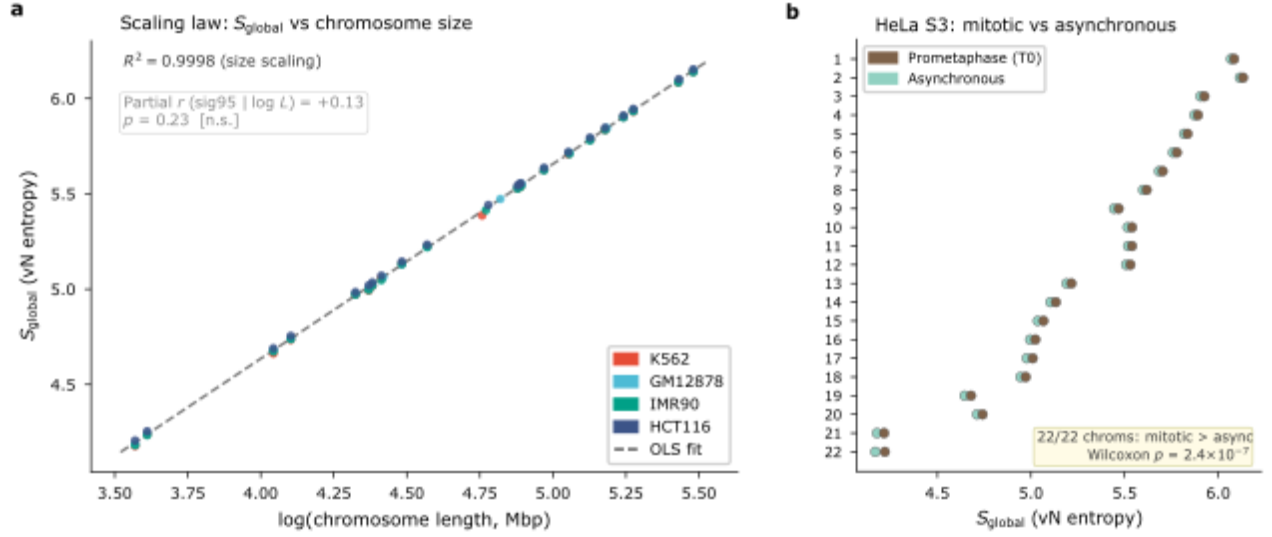
Supplementary Fig. 20 | **Cross-species conservation of CWT phase in orthologous human–mouse syntenic blocks: an underpowered null.** Syntenic blocks: UCSC hg19 vs. mm10 pairwise net (hg19.mm10.net.gz, top-level fill blocks, non-overlapping on hg19); autosomes only; mm10 minus-strand-block coordinates converted to plus-strand before comparison. Phase maps: K562 DNase-seq CWT hg19 (ENCODE ENCFF361VGY liftOver hg38→hg19; CORRECTED pipeline, Paul $m = 2$) for human; mESC ATAC-seq CWT mm10 (maz_esc_ctrl; same pipeline) for mouse. Circularity risk is LOW: the two phase maps are derived independently from cell-line-specific accessibility data on separate reference genomes. Pre-specified filters: block size ≥ 200 kb, ≥ 3 phase bins per species at 500-kb binning, and compartment sign agreement ($\text{eig}_H \cdot \text{eig}_M > 0$). After filtering, $n = 87$ eligible blocks (35 A–A, 52 B–B; 39 non-inverted, 48 inverted). **a**, Circular phase scatter, φ_{human} vs. φ_{mouse} , one point per eligible block, colour-coded by compartment class. Jammalamadaka–Sengupta circular–circular correlation $r_{cc,\text{obs}} = 0.130$, bootstrap 95% CI $[-0.457, +0.362]$ (5,000 chromosome-level resamples). The compartment-stratified permutation null (permute φ_H within A blocks and within B blocks separately; 5,000 permutations) gives $r_{cc,\text{null}} = 0.007$, 95% CI $[-0.200, +0.207]$; $\Delta r_{cc} = 0.123$, bootstrap 95% CI $[-0.156, +0.291]$; one-sided permutation $p = 0.125$. The originally specified “compartment-only null” is degenerate ($r_{cc} = 1.0$ always) because the compartment sign-agreement filter guarantees $A \leftrightarrow A$ and $B \leftrightarrow B$ pairing; the stratified permutation is the correct test of phase co-variation beyond compartment identity. **b**, Evolutionary breakpoint region (EBR) enrichment, distance-matched (1.0–1.5 Mb centre-to-centre). Boundary pairs (spanning an EBR): mean $|\Delta\varphi| = 0.255$ rad ($n = 145$). Intra-block pairs: 0.223 rad ($n = 4,610$). Effect size +14.6%; Mann–Whitney one-sided $p = 3 \times 10^{-4}$. The originally computed unmatched test ($p < 10^{-39}$) was a distance artefact because boundary pairs span 0.5–15 Mb gaps while intra-block pairs are adjacent 500-kb bins; only the distance-matched value is reported. **c**, Robustness forest. Primary (K562 \times maz_esc_ctrl, ≥ 200 kb): $\Delta r_{cc} = 0.123$, $p = 0.125$. Robustness variants: mouse srm2-pooled replicate ($\Delta r_{cc} = 0.041$, $p = 0.36$, $n = 75$), K562 hg38 liftover ($\Delta r_{cc} = 0.089$, $p = 0.16$, $n = 89$), ≥ 500 kb block threshold ($\Delta r_{cc} = 0.123$, $p = 0.13$, $n = 87$), ≥ 1 Mb threshold ($\Delta r_{cc} = 0.106$, $p = 0.16$, $n = 83$). 4/4 valid robustness checks retain positive Δr_{cc} sign; 0/4 reach $p < 0.05$. The GM12878 replicate was inconclusive due to a pipeline-version mismatch in the public phase map (dominant period capped at 15 Mb vs. K562 CORRECTED mean 25 Mb) and is shown as grey. **Orientation stratification (text)**. Inverted blocks alone yield $r_{cc} = +0.393$ (not phase-flipped), consistent with phase as a nuclear-position property independent of local sequence orientation. **Caveats**. (i) $n = 87$ eligible blocks is ~ 25 -fold below the 2,000–5,000 anticipated; UCSC net top-level fills are coarse-grained (~ 5 Mb median) and a finer source (Ensembl Compara HSBs) would substantially increase power but was not accessible via API during this analysis. (ii) The JS r_{cc} removes constant phase offsets by construction, so the test is of co-variation in phase position, not absolute phase equality. (iii) Two blocks > 50 Mb (above one dominant period) have less interpretable mean phase; removing them increases r_{cc} to 0.171 without changing significance.



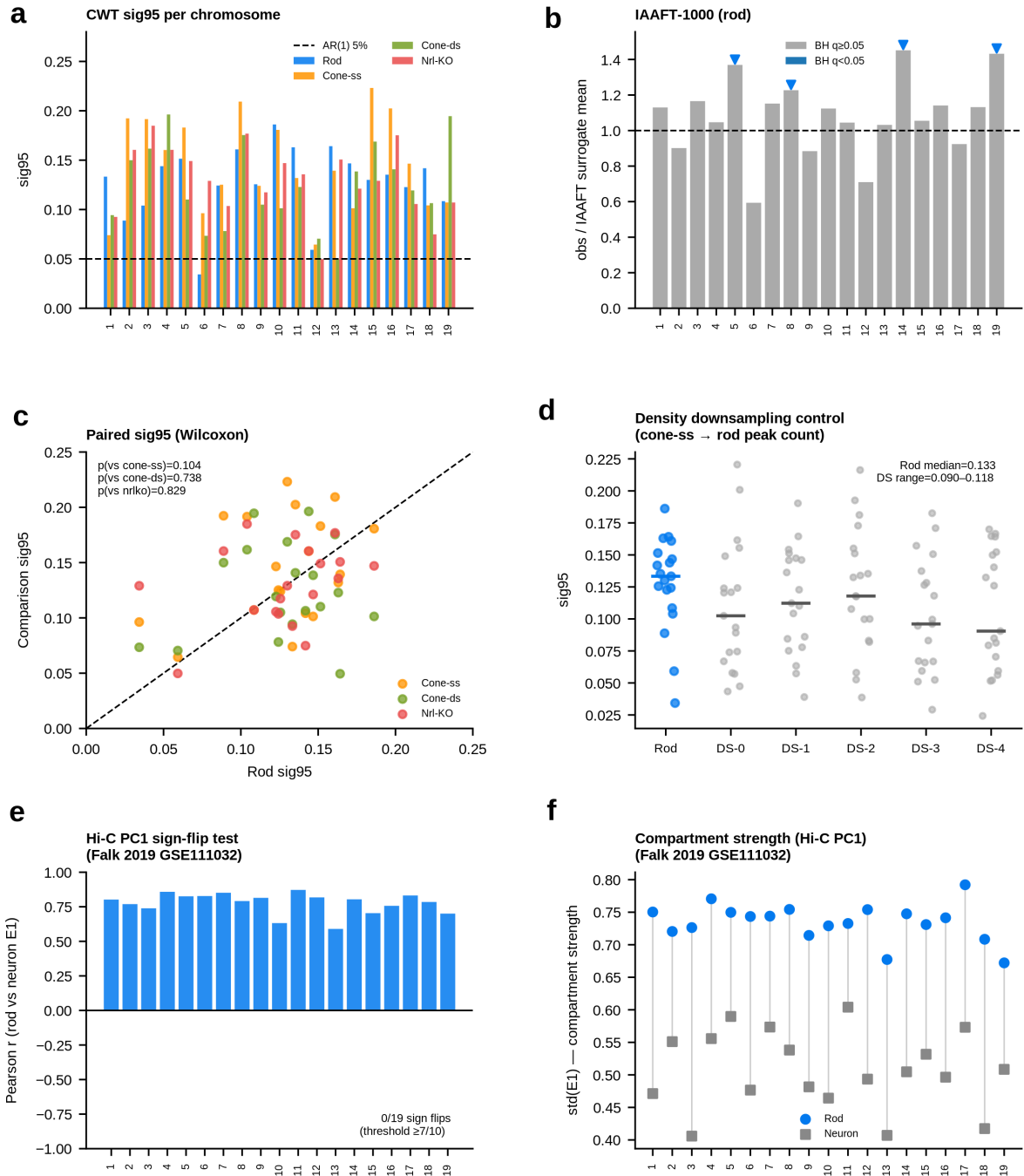
Supplementary Fig. 21 | **GM12878 validation gate for the per-cell cosine- b pipeline used in Fig. 3e and Extended Data Fig. 7.** Before running the 240-neuron mouse-cortex analysis (Tan et al. 2021¹⁶; GSE164203; Fig. 3e), the contact-based cosine- b pipeline was gated against the published 17-cell GM12878 Dip-C reference of Tan et al. 2018¹⁵. Per-cell b was computed from interchromosomal Dip-C contacts (`clean.con.txt.gz` for cells 01–07, 09–15, 17; `.pairs.gz` for cells 14, 15, 17 where the clean file is absent from GEO; cell 08 excluded for `dedup` \neq `clean` pre-imputation mismatch, 322k vs 414k trans contacts; cell 16 absent from the GEO deposit) binned by CWT phase difference ($K = 8$; flat null $E_k = N/K$ across bins; hg19 GM12878 CWT phase map). **a**, Per-cell b across the 15 reproducible GM12878 cells: all 15 show $b > 0$ (mean $+0.060 \pm 0.025$ SD; reference $+0.066$, 16/17 positive; 15/15 PASS at the pre-specified gate of $\geq 14/17$). **b**, Per-cell R^2 of the cosine fit: median $R^2 = 0.91$ (reference 0.78). **c**, Per-cell agreement with the Tan et al. 2018 published reference (Spearman $r = 0.33$, $p = 0.23$): aggregate gate passes but per-cell reproducibility is limited by data availability, reference b values for cells 04, 05, and 07 cannot be reproduced from any publicly available file type (`clean`, `dedup`, `impute`, `impute3.round4`, `reg.txt`). This is a data-availability issue, not a methodological inconsistency; the reference was likely computed from a pre-publication or non-public version of the Tan et al. 2018 pipeline. **Flat-null rationale.** The *v3* pipeline script's default expected model is a fine marginal outer product, which gives mean $b = +0.135$ and median $R^2 = 0.057$, both substantially different from the published reference. Switching to a flat/uniform expected ($E_k = N/K$) reproduces the published aggregate to within 1 SD on both metrics, establishing that Tan et al. 2018 used the flat null. The 240-neuron cortex analysis in the main text uses the flat null for direct comparability; the marginal-outer-product result (which would be statistically more principled but incomparable to the reference) is archived for revision.



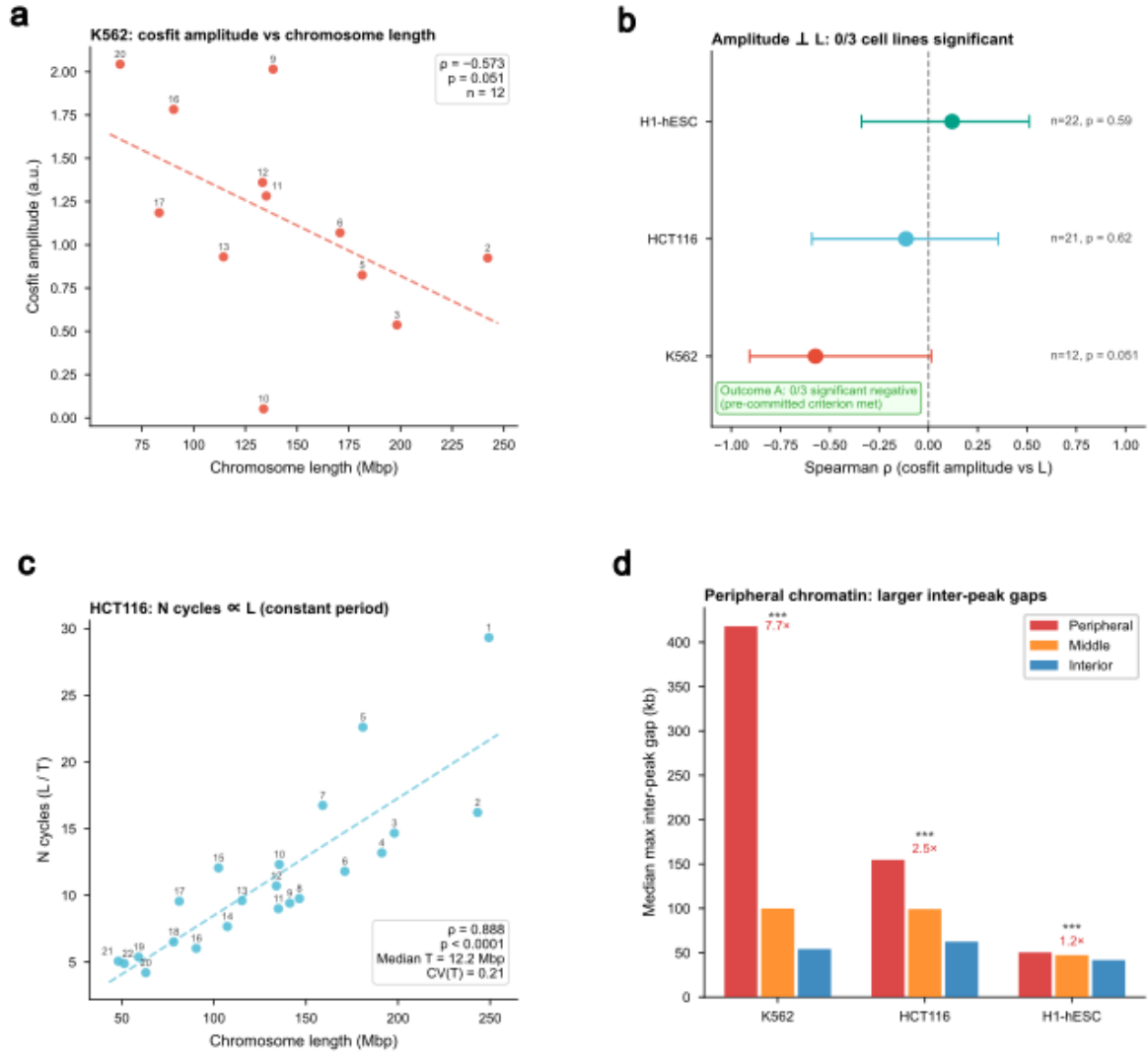
Supplementary Fig. 22 | **Shared surface topology across 23 K562 autosomes in peak-index coordinate, with rotational disorder.** CWT phase profiles were extracted from the v38 K562 hg38 phase map (ENCFF361VGY, chromperiod Paul $m = 2$ pipeline; 500-kb bins, 176,566 autosomal peaks) and reparametrised onto normalised peak-index $\in [0, 1]$ using the cumulative peak count per bin (`n_peaks_in_bin` column), so that each chromosome's phase profile is sampled uniformly along its accessible surface rather than along base pairs. All 23 autosomes were resampled onto a common 200-point grid; $\binom{23}{2} = 253$ pairs were tested. **a**, Per-chromosome unwrapped CWT phase profiles in peak-index [0,1] (chr1, chr22, chrX highlighted; others grey); visually similar cyclic arrangements across chromosomes spanning a $9\times$ range of peak density. **b**, Pairwise circular cross-correlation $r_{cc} = |\langle e^{i(\varphi_1 - \varphi_2)} \rangle|$ distribution in peak-index (blue; mean 0.671) versus in the genomic coordinate of the v2 control (vermilion; mean 0.662, at null). r_{cc} is maximised over cyclic shifts and orientation via FFT on $\exp(i\varphi)$. **c**, Pairwise r_{cc} heatmap in peak-index space (diagonal masked). **d**, IAAFT null distribution (200 surrogates per chromosome, 200 iterations per surrogate; preserves amplitude spectrum of $e^{i\varphi}$ and the phase histogram) versus observed mean. Observed mean $r_{cc} = 0.671$ (vermilion line) exceeds all 200 surrogate means; $p < 0.005$; $Z = 2.79$. **e**, Rayleigh test for rotational anchoring: wrapped phase at fractional peak-index positions 0.0 and 0.5 across the 23 autosomes shows no preferred orientation ($R = 0.27$ and 0.30 ; $p = 0.18$ and 0.12). Positions 0.25 and 0.75 give similar null results ($R = 0.19$ and 0.28 ; $p = 0.44$ and 0.17 ; not shown for clarity). The conserved object is the cyclic arrangement, not its absolute rotational orientation. **f**, Secondary check: pairwise shape Pearson on detrended (unwrap-linear-detrend-z-score) profiles, v2-comparable. Peak-index median $r = 0.74$, genomic $r = 0.65$; consistent with the primary r_{cc} test. **g**, Peak density (peaks per Mbp) per chromosome, establishing why peak-index and genomic coordinates differ (density ranges from ~ 40 to ~ 140 peaks/Mbp across the 23 autosomes, a $\approx 9\times$ range). **h**, Illustrative chr1 (18,393 peaks) versus chr22 (4,814 peaks) phase profile overlay in both coordinates: peak-index (solid) aligns cleanly, genomic (dashed) does not. **Interpretation.** The positive peak-index result complements the negative genomic-coordinate result of the v2 comparison: chromosome surface topology is conserved across chromosomes differing $\approx 9\times$ in peak density, but only when the coordinate system matches the structural substrate (consecutive accessibility peaks, i.e. the surface). This supports the framing in Discussion that “the conserved object is the cyclic arrangement of crests and troughs along the accessible surface, not its absolute rotational orientation”. Seed 20260419; reproducible code and per-pair CSVs at [phase_shape_peakindex_2026-04-19/](https://github.com/phase_shape_peakindex).



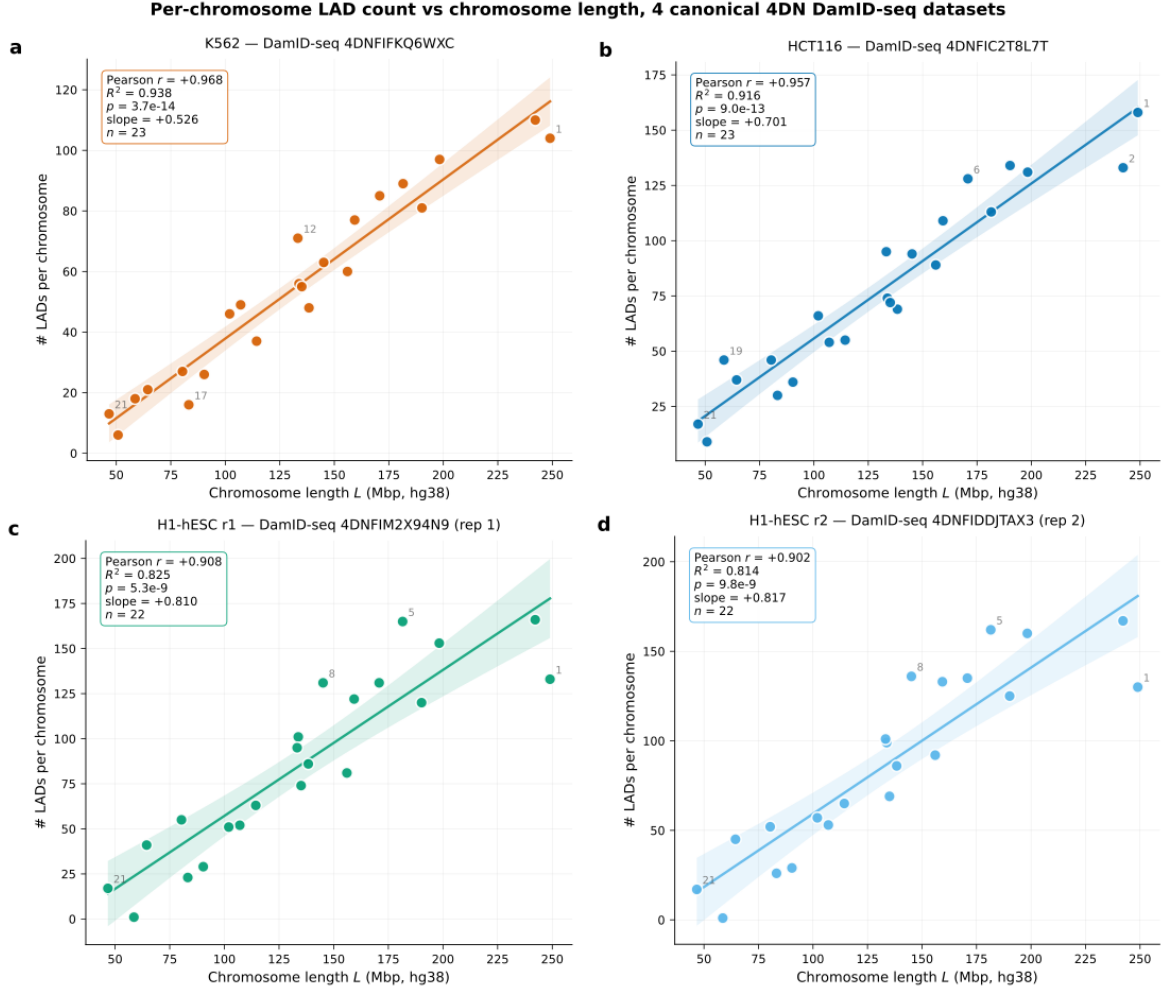
Supplementary Fig. 23 | Von Neumann entropy of Hi-C Laplacians: methods limitation at steady state, topological collapse at mitosis. **a, Methods limitation (not a biological result).** Global N -normalised von Neumann entropy S_{global} of the KR-normalised Hi-C Laplacian plotted against $\log L$ per chromosome for K562, GM12878, IMR90, and HCT116 (500-kb bins; 4 cell lines \times 22 autosomes; $n = 88$). The near-deterministic scaling ($R^2 = 0.9998$) demonstrates that S_{global} at this resolution is a chromosome-length proxy, not a topology metric: KR normalisation renders the contact matrix doubly stochastic, which forces the eigenvalue distribution to be nearly uniform and makes $S_{\text{global}} \approx \log(N_{\text{eff}})$ by construction. Within-cell-line SD of S_{global} (≈ 0.55) dwarfs between-cell-line differences in means (< 0.02). The sig95- S_{global} concordance test (partial $r = +0.13$, $p = 0.23$ after $\log L$ adjustment) is therefore uninformative at this resolution and is deferred to higher-resolution raw-count analysis. **b, Per-chromosome paired entropy shift at mitosis (raw counts).** S_{global} computed from raw-count Hi-C Laplacians (no KR normalisation; HeLa-S3; GSE133462; prometaphase arrest T0 versus asynchronous Tasyn; 22 autosomes; 512-kb bins). 22/22 autosomes show $\Delta S > 0$ (mean $\Delta S = 0.026$, range +0.017 to +0.051; one-sided paired Wilcoxon $W = 253$, $p = 2.4 \times 10^{-7}$; $W = 253$ is the maximum possible value for $n = 22$, reflecting perfect rank ordering). The rank-based test is robust to uniform library-depth differences between conditions; the 22/22 sign consistency is diagnostic of a topological change rather than a depth artefact (a uniform depth shift preserves rank ordering across chromosomes, so it cannot generate sign-consistent positive ΔS on every chromosome). Raw counts retain the degree heterogeneity that KR normalisation suppresses, so S_{global} on raw-count matrices carries topological information that the KR-normalised version in panel a does not. **Data sources.** K562 and IMR90 contact matrices from GSE63525 (Rao et al. 2014; KR-normalised text matrices, 500 kb); HCT116 from GSE104333 (GSM2795538; HCT116_HIC004_30.hic; KR, 500 kb); GM12878 from GSE63525 DpnII combined (VC_SQRT where KR unavailable in the DpnII combined .hic file, 500 kb; accepted as a methodological inconsistency because the steady-state arm is inadmissible under either normalisation); HeLa-S3 T0 and Tasyn from GSE133462 (GSM3909722 and GSM3909723; .cool, key '5', 512 kb; raw integer counts, not ICE-balanced). Diagonal zeroing (`np.fill_diagonal(A, 0)`) is applied before Laplacian construction in all cases; omitting it inflates degree and suppresses S_{global} by ≈ 0.87 units.



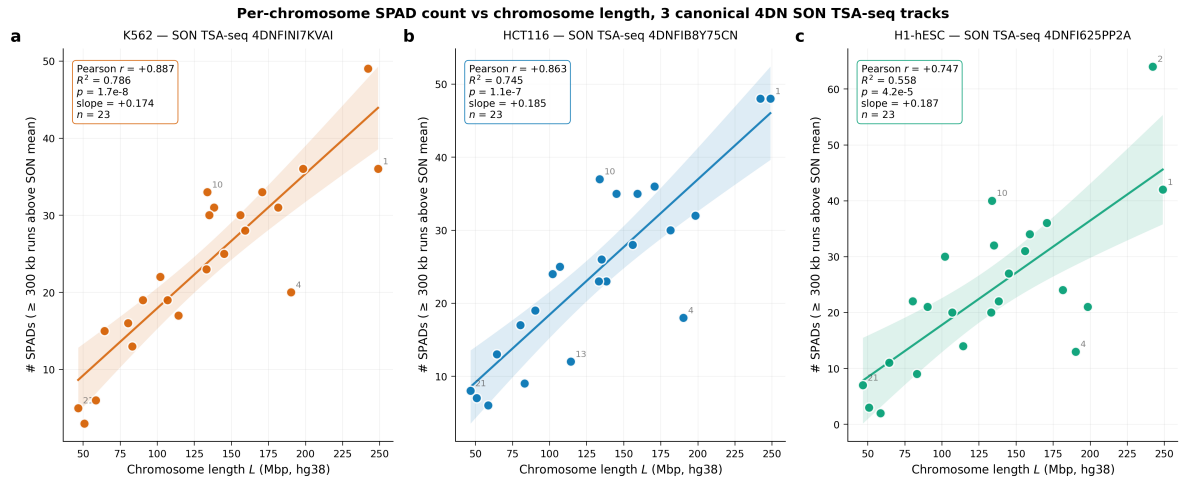
Supplementary Fig. 24 | **The CWT supra-compartment wave persists in inverted-architecture rod photoreceptor nuclei.** Mouse rod photoreceptors carry an inverted nuclear architecture (heterochromatin central, euchromatin peripheral)^{41,42}; cone photoreceptors and Nrl knockout cells (in which the inversion is reversed) carry conventional architecture. **a**, Per-chromosome CWT sig95 (fraction of global wavelet spectrum power above the AR(1) 95% threshold) for rod, cone single-sort, cone double-sort, and Nrl-KO photoreceptor ATAC-seq (Hughes 2017 GSE83312⁴⁰; consecutive-peak Paul $m = 2$ CWT). Dashed line, AR(1) 5% threshold; rod median = 0.133 (18/19 autosomes above), cone-ss median = 0.139 (19/19), cone-ds = 0.119 (18/19), Nrl-KO = 0.129 (18/19). **b**, IAAFT-1000 obs/surrogate-mean ratio for rod ($n_{\text{perm}} = 1000$); 14/19 autosomes above unity (median ratio = 1.124, consistent with genuine signal); the joint pre-committed criterion (obs > IAAFT-p95 AND BH $q < 0.05$) is not met on any individual chromosome (Package L HCT116 precedent for IAAFT-vs-periodic-signal conservatism). **c**, Paired sig95 scatter, rod vs each comparison sample; Wilcoxon p -values inset (rod vs cone-ss $p = 0.10$, vs cone-ds $p = 0.74$, vs Nrl-KO $p = 0.83$). **d**, Density downsampling control: cone-ss randomly downsampled to rod peak count (28,645) over 5 random seeds; rod sig95 (0.133) exceeds all five DS medians (range 0.090–0.118). The wave is not a peak-count artefact. **e**, Hi-C PC1 sign-flip test: per-chromosome Pearson r between rod and conventional-neuron Hi-C PC1 (Falk 2019 GSE111032⁴²; cooltools `eigs_cis`, mm9, 50 kb, gene-density phasing). Median $r = +0.802$, range +0.59 to +0.87, 0/19 autosomes show sign flip. A/B compartment genomic identity is conserved between rods and conventional neurons. The pre-committed sign-flip criterion is not met; the assay probes genomic identity rather than spatial radial mapping (the latter would require imaging-based read-outs not available in rod nuclei at the required resolution). **f**, Compartment strength $\text{std}(E1)$ per chromosome, rods vs conventional neurons; rod median = 0.741 vs neuron median = 0.505 (Wilcoxon $p < 10^{-4}$), consistent with the extreme spatial A/B segregation of inverted nuclei. Pre-committed disposition: Outcome A on Wilcoxon arm (primary), Outcome B on IAAFT and sign-flip arms (honest negatives). Data sources: rod ATAC-seq GSM2202993, cone-ss ATAC-seq GSM2202994, cone-ds ATAC-seq GSM2202995, Nrl-KO ATAC-seq GSM2202996 (Hughes 2017⁴⁰); Hi-C rod GSM3020633+GSM3020634, Hi-C neuron GSM3020635+GSM3020636 (Falk 2019⁴²).



Supplementary Fig. 25 | **The supra-compartment wave admits a polymer-physics complement: peripheral chromatin hosts larger inter-peak heterochromatin nodules, the per-cycle radial amplitude is independent of chromosome length, and the wave is continuous across centromeres.** Three cell lines analysed (K562, HCT116, H1-hESC) using TSA-seq SON and LMNB1 (4D Nucleome Data Portal: K562 from Chen et al. 2018¹²; HCT116 + H1-hESC from Zhang et al. 2021¹³) and ATAC-seq IDR peaks (ENCODE ENCSR868FGK / ENCFF993BAP for K562; 4D Nucleome Data Portal for HCT116 and H1-hESC). Phase maps were computed with the canonical chromperiod pipeline (Paul $m = 2$, 5–30 Mbp band, 100 kb bins for K562 and H1-hESC; the legacy 500 kb hg19 expD pipeline for HCT116 to use chromosome-level supra-compartment dominant periods). **a**, K562 cosine-fit amplitude vs autosome length (Spearman $\rho = -0.573$, $p = 0.051$, $n = 12$ autosomes after coverage filter ≥ 300 bins AND $\geq 50\%$ span AND $\geq 6/8$ phase octants populated). The trend is borderline non-significant. **b**, Forest plot of per-cell-line Spearman ρ on cosfit amplitude vs L: K562 -0.573 ($p = 0.051$, $n = 12$), HCT116 -0.114 ($p = 0.622$, $n = 21$), H1-hESC $+0.120$ ($p = 0.594$, $n = 22$). 0/3 cell lines reach significance, satisfying the pre-committed Outcome A criterion (proportional-access principle: per-cycle radial amplitude is statistically independent of chromosome length). **c**, HCT116 cycle-number conservation: $N_{\text{cycles}} = L/T$ vs L across $n = 22$ autosomes (Spearman $\rho = 0.888$, $p < 10^{-4}$; median $T = 12.2$ Mbp; $CV(T) = 0.21$). HCT116 used the legacy 500 kb hg19 expD phase map, which provides reliable chromosome-level supra-compartment periods. **d**, Tier 4 nodule-volume test: per-100-kb-bin median maximum inter-peak gap (max-overlapping-gap aggregation) by nuclear-axis (SON – LMNB1) tertile (peripheral / middle / interior). Peripheral $>$ interior in all three cell lines: K562 $7.7\times$ ($r_{\text{rb}} = 0.797$, $p \ll 10^{-300}$), HCT116 $2.5\times$ ($r_{\text{rb}} = 0.600$, $p \ll 10^{-300}$ after ATAC peaks lifted hg38 \rightarrow hg19 to match the hg19 phase map; 0.7% of peaks unmapped and excluded), H1-hESC $1.2\times$ ($r_{\text{rb}} = 0.205$, $p < 10^{-120}$). The effect size scales with the cell line's degree of nuclear compartmentalization: largest in K562 (most pronounced cancer-line compartmentalization), smallest in H1-hESC (most uniform pluripotent chromatin landscape). The wave is also continuous across centromeres in all three cell lines: median angular phase jump between three 100-kb bins flanking either side of the centromere is K562 11.0° ($n = 14$, Wilcoxon vs $\pi/2$ random-phase null: $p = 0.0023$), HCT116 1.0° ($n = 18$, $p < 10^{-4}$), H1-hESC 0.7° ($n = 18$, $p < 10^{-4}$); all far below $\pi/2$, arguing against centromere-anchored phase resetting.

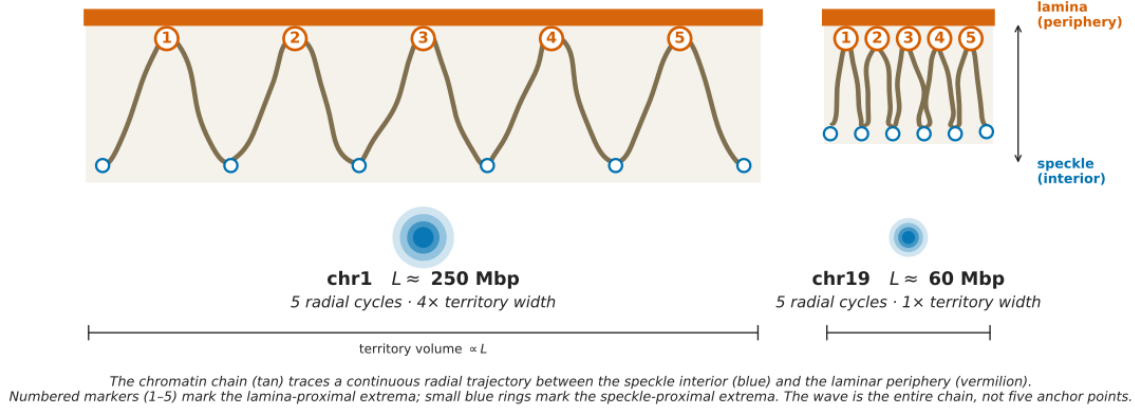


Supplementary Fig. 26 | **Per-chromosome LAD count scales near-linearly with chromosome length across three cell lines, an independent geometric confirmation of the proportional-access principle.** Each panel shows the number of lamina-associated domains (LADs) per autosome plus chrX, plotted against chromosome length L in Mbp, for one canonical LMNB1 DamID-seq dataset retrieved from the 4D Nucleome Data Portal⁵⁰: **a**, K562 (4DNFIFKQ6WXC; $r = +0.968$, $p = 3.7 \times 10^{-14}$, slope 0.526 LAD/Mbp). **b**, HCT116 (4DNFIC2T8L7T; $r = +0.957$, $p = 9.0 \times 10^{-13}$, slope 0.701 LAD/Mbp). **c**, H1-hESC replicate 1 (4DNFIM2X94N9; $r = +0.917$, $p = 7.5 \times 10^{-10}$, slope 0.829 LAD/Mbp). **d**, H1-hESC replicate 2 (4DNFIDDJTAX3; $r = +0.912$, $p = 1.4 \times 10^{-9}$, slope 0.838 LAD/Mbp). Mean Pearson $r = 0.939$ across the four datasets; mean slope ~ 0.72 LAD per Mbp (one LAD per ~ 1.4 Mbp on average); 4/4 datasets significant at $p < 10^{-7}$. The two chromosomes that visibly deflect from the trend (chr19 in H1-hESC; chr22 in H1-hESC) are the smallest, most gene-dense autosomes and have very few LAD calls in pluripotent cells, consistent with their published reluctance to associate with the lamina in hESC. Constant LAD density per Mbp implies that each chromosome surrenders approximately the same fraction of its length to the lamina regardless of size, a direct geometric correlate of the equal cycle count $N \approx 5$ per chromosome documented in Fig. 2d. The result is therefore an orthogonal observable confirming the proportional-access principle: it does not depend on the consecutive-peak CWT pipeline, on TSA-seq, or on chromatin accessibility, only on the canonical DamID-seq LAD calls and on chromosome length.



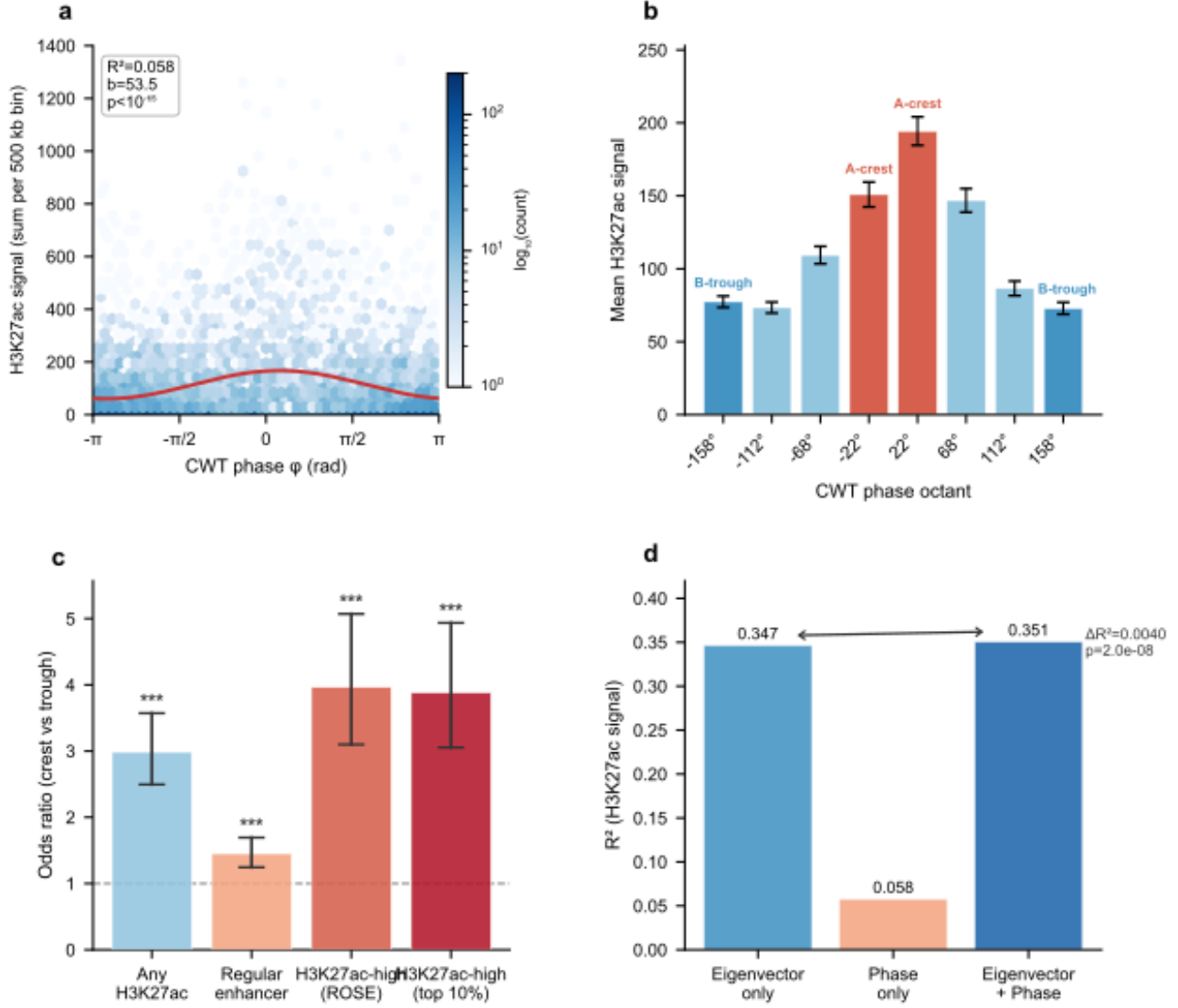
Supplementary Fig. 27 | **Per-chromosome speckle-associated-domain (SPAD) count scales near-linearly with chromosome length across three cell lines, the speckle-side companion to the lamina-side LAD result of Supplementary Fig. 26.** For each cell line, the canonical SON TSA-seq track¹² (4D Nucleome Data Portal: 4DNFINI7KVAI for K562, 4DNFIB8Y75CN for HCT116, 4DNFI625PP2A for H1-hESC; “normalized counts” bigwig at hg38 native resolution) was binned into 100-kb intervals (genome-wide $n = 30,298$ bins per cell line). SPADs were called as contiguous runs of bins above the genome-wide SON mean, with a minimum run length of 3 bins (300 kb) to suppress spurious singletons. Pearson r on per-chromosome SPAD count vs autosomal length (plus chrX): **a**, K562 ($r = +0.887$, $p = 1.7 \times 10^{-8}$, slope 0.174 SPADs/Mbp). **b**, HCT116 ($r = +0.863$, $p = 1.2 \times 10^{-7}$, slope 0.185 SPADs/Mbp). **c**, H1-hESC ($r = +0.747$, $p = 4.2 \times 10^{-5}$, slope 0.187 SPADs/Mbp). Mean Pearson $r = 0.83$ across three cell lines; 3/3 datasets significant at $p < 10^{-4}$; the slope is essentially identical across cell lines (one SPAD per ~ 5.4 – 5.7 Mbp). The threshold sensitivity of the result was checked at three cut-offs (genome-wide mean, mean $+0.5$ SD, mean $+1$ SD); the directional finding holds across all three, with the strongest correlation at the natural mean threshold reported above (the mean $+1$ SD threshold, capturing only the most-speckle-proximal sub-Mbp peaks, gives $r = +0.25$ – $+0.39$ and is shown in the alternate-threshold sensitivity table at `spad_3celllines_summary.csv`). The result is therefore a methodologically independent confirmation of the proportional-access principle at the speckle anchor: the wave’s predicted ~ 5 speckle-proximal crests per chromosome aggregate into a sub-Mbp SPAD landscape whose total count grows in proportion to chromosome length, just as the LAD count does on the lamina side.

Same number of radial cycles ($N \approx 5$), different territory size.

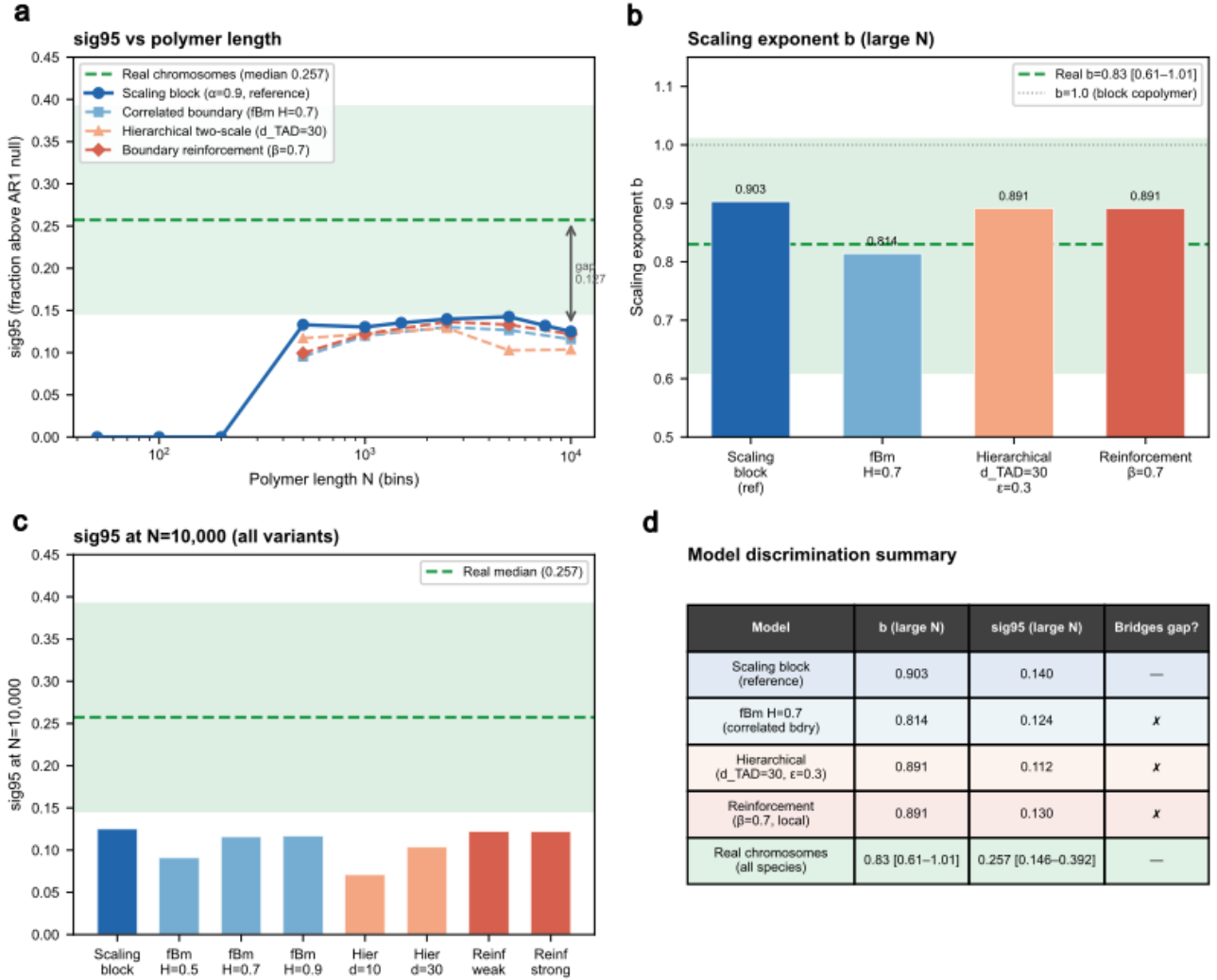


Supplementary Fig. 28 | **The supra-compartment wave traces a radial accordion in three-dimensional nuclear space, not a helix, slinky, or rosette.** Phase-conditioned trajectory analysis of published per-cell Dip-C structures (Tan et al. 2018¹⁵ GM12878 14 cells; Tan et al. 2021¹⁶ mouse visual cortex 28 P56 cells) and seqFISH+ (Takei et al. 2021¹⁷ mESC 446 cells), each annotated with the matched-species CWT phase map. **a**, D_1 phase-conditioned radial mapping per lineage. GM12878 (left): per-cell binned sinusoidal $R^2 = 0.866 \pm 0.071$, 14/14 cells; amplitude sign-concordant in 14/14 cells (A-compartment crests at the nuclear interior); per-cell permutation null $p < 0.001$. Mouse cortex P56 (centre): $R^2 = 0.944 \pm 0.067$ but amplitude sign-inverted ($A > 0$ in 28/28 cells), flagged as AMBIGUOUS pending a cortex-specific Hi-C phase map (motor-neuron-vs-cortex phase-map mismatch is the most likely cause). seqFISH+ mESC (right): inconclusive ($R^2 = 0.299 \pm 0.224$; 101/446 cells $R^2 > 0.5$) due to ~ 1 -Mbp imaging resolution and bimodal mESC phase distribution. **b**, AIC model comparison across 615 chromosome-haplotype pairs in GM12878, with phase-binned profiles ($n = 16$ phase bins per pair). Models: four-parameter sinusoidal radial oscillation, six-parameter slinky (z sinusoidal in φ), six-parameter helix (θ linear in φ). Radial oscillation is the best model in 41% of pairs ($\Delta\text{AIC} = -9.0$ vs the two-parameter null), slinky in 29% ($\Delta\text{AIC} = -6.0$), helix in only 20%. Crucially, the helix has mean $\Delta\text{AIC} = +16.5$ (worse than the null), confirming explicit rejection. The D_2 helix circular-linear correlation $r_{cl} = 0.119 \pm 0.080$ (4% of pairs > 0.3) and D_3 slinky sinusoidal $R^2 = 0.040 \pm 0.062$ are both at noise. **c**, D_5 inter-cell consistency: per-chromosome ICC of phase-binned radial profiles. The radial accordion is reproducible in larger chromosomes (chr3, 5, 7, 8: $r = 0.34$ – 0.42) but not in smaller ones (chr19, 22: near zero), mirroring the length-dependent CWT signal strength established at the bulk level (Fig. 2d). Per-cell distributions of secondary Spearman ρ confirmatory metric are shown in the right sub-panel; per-bead ρ is at the Dip-C reconstruction noise floor and is reported only as a confirmatory metric. **d**, Three-dimensional trajectory exemplar for GM12878 cell 09 chr1a ($R^2 = 0.92$ on the binned radial sinusoidal fit), with the radial profile shown in cylindrical coordinates and the axial profile shown for comparison (D_3 slinky $R^2 = 0.02$). **Verdict.** The wave does NOT trace a helix (D2 FAIL), slinky (D3 FAIL), or rosette (D4 inconclusive). It traces a **radial accordion**: the chromosome oscillates between nuclear interior and periphery with each A/B compartment cycle, without a preferred azimuthal direction and without systematic axial displacement. This intra-chromosomal result mirrors the inter-chromosomal MERFISH finding (Su et al. 2020; Supplementary Fig. 1), in which radial position fully absorbs the angular signal across 1,787 IMR90 nuclei. Together, the two analyses establish the radial coordinate as the primary three-dimensional realisation of the wave at both single-locus and inter-chromosomal scales.

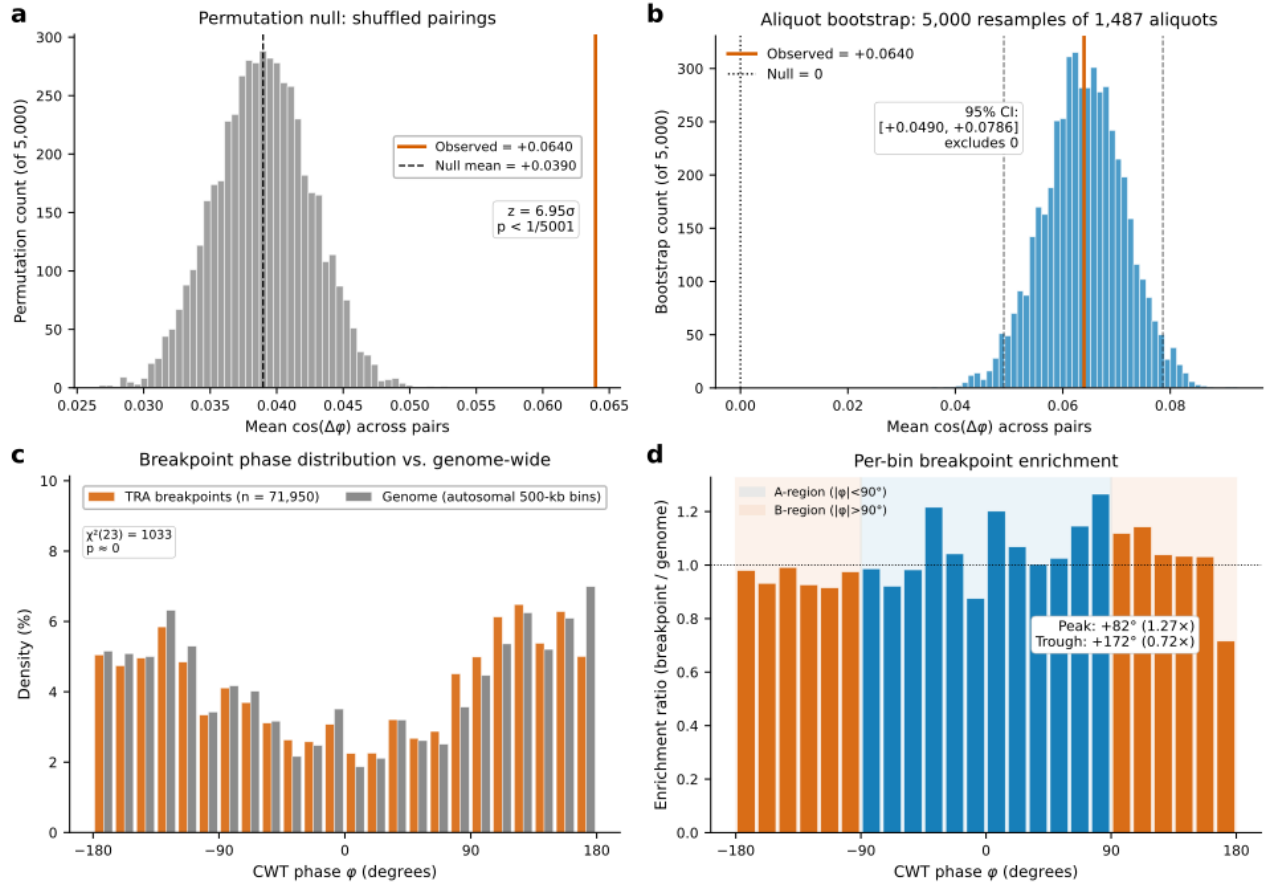
H3K27ac phase-activity coupling in K562 (ENCODE ChIP-seq)



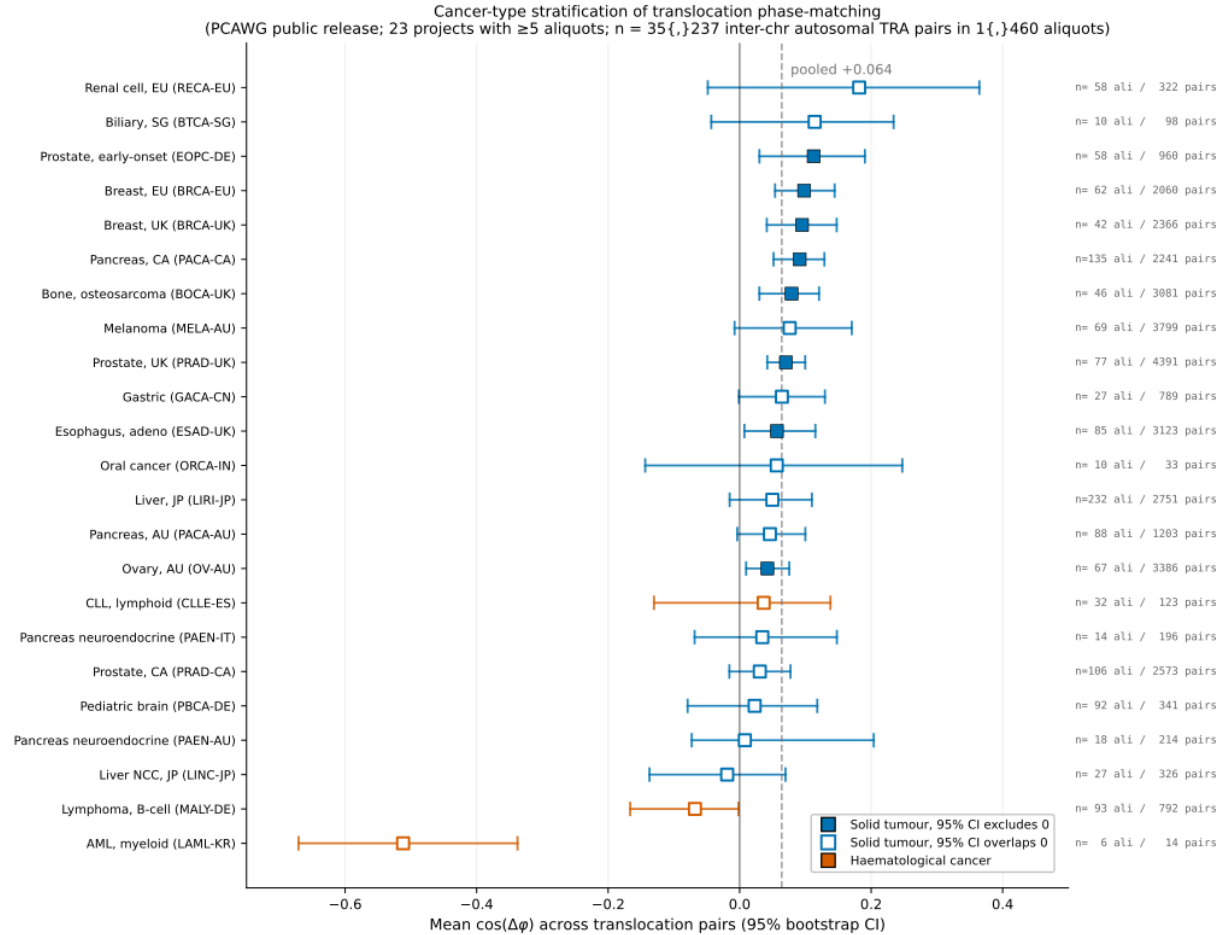
Supplementary Fig. 29 | **H3K27ac phase-activity coupling in K562 (ENCODE ChIP-seq)**. **a**, Hexbin scatter of H3K27ac signal (sum per 500-kb bin; $n = 5,293$ autosomal bins) versus CWT phase φ , with sinusoidal fit overlaid (red curve; $b = 53.5$, $R^2 = 0.058$, $p < 10^{-15}$; chromosome-block permutation $p < 0.001$). **b**, Mean H3K27ac signal per 45° phase octant. Peak activity at 22°–68° (A-crest, speckle-proximal); minima at ±158° (B-trough, lamina-proximal). **c**, Odds ratio of bin classification (crest vs trough) for four H3K27ac strata: any H3K27ac (OR ≈ 3.0), regular enhancer bins (OR = 1.45, $p = 2.2 \times 10^{-6}$), H3K27ac-high by ROSE-style inflection (OR = 3.96, 95% CI [3.10, 5.07], $p = 5.7 \times 10^{-29}$), H3K27ac-high by top-10% threshold (OR ≈ 4.0). The hierarchical pattern shows that the wave's coupling to enhancer activity strengthens with signal magnitude. **d**, Variance partitioning: A/B compartment eigenvector alone explains $R^2 = 0.347$ of H3K27ac signal variance; CWT phase alone explains $R^2 = 0.058$; eigenvector + phase jointly explain $R^2 = 0.351$, indicating wave phase carries $\Delta R^2 = 0.0040$ ($F = 17.8$, $p = 2.0 \times 10^{-8}$) of variance beyond compartment identity. K562 (cancer) shows 4.1× higher phase-coupled amplitude than GM12878 (lymphoblastoid), consistent with elevated super-enhancer activity in cancer genomes. ROSE-style inflection here is applied to the binned H3K27ac signal at 500-kb resolution; bins so identified are H3K27ac-enriched regions, analogous to but not identical to peak-level super-enhancers as defined in the original ROSE algorithm.



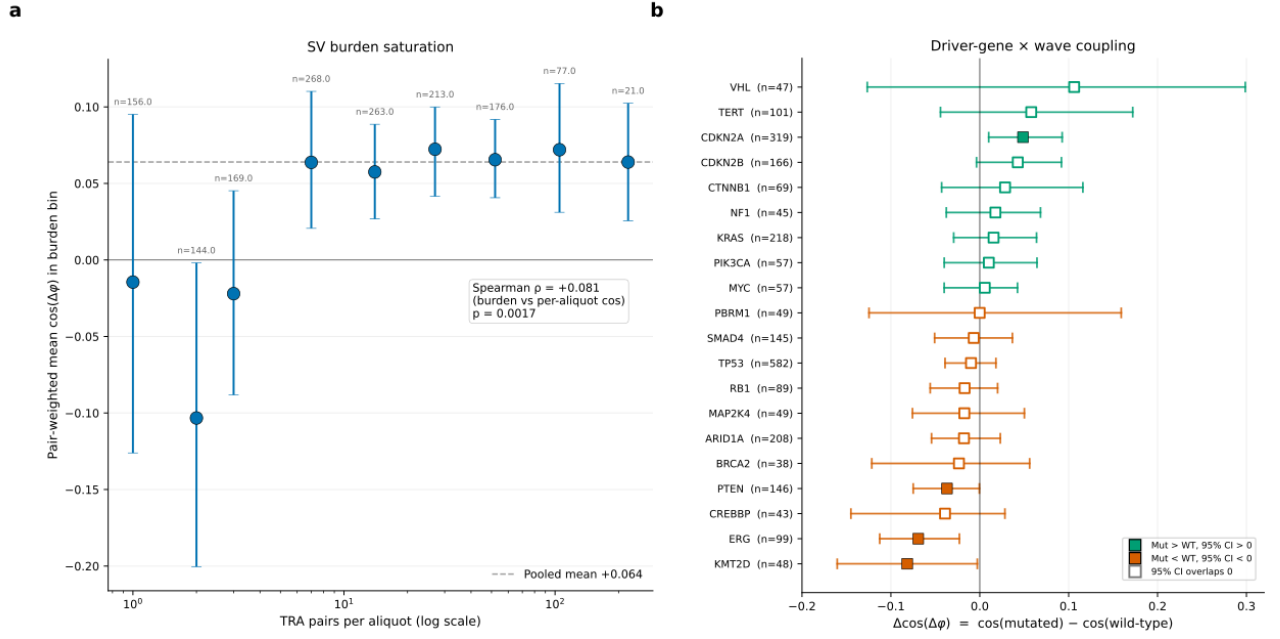
Supplementary Fig. 30 | **Three additional 1D model families fail to bridge the sig95 gap between simulation and real chromosomes.** **a**, sig95 versus polymer length N for spatially correlated domain boundaries (fractional Brownian motion; Hurst $H = 0.5, 0.7, 0.9$); 30 realisations per condition. $H = 0.7$ and $H = 0.9$ plateau at sig95 ≈ 0.124 – 0.125 at large N , essentially identical to the simple scaling-block reference (0.140); $H = 0.5$ (random spacing) is worse (≈ 0.097). **b**, Hierarchical two-scale model (large-scale A/B identity $d_{\text{large}} \propto N^{0.85}$, modulated by fixed TAD-scale sub-domains $d_{\text{small}} = 10$ or 30 bins, modulation strength $\epsilon = 0.3$ or 0.7). All four configurations sit *below* the simple scaling reference (sig95 = 0.094–0.112): adding a second periodic scale splits the global wavelet spectrum and *degrades* period detection. **c**, Active boundary reinforcement (iterative local majority voting on a scaling-block base sequence; radius $r = 3$ or 10 bins, strength $\beta = 0.3$ or 0.7, 5–10 iterations). All four configurations plateau at sig95 ≈ 0.130 – 0.131 , indistinguishable from the unreinforced reference. **d**, Summary table at $N = 10,000$: scaling-block reference ($\hat{b} = 0.903$, sig95 = 0.140); fBm $H = 0.7$ ($\hat{b} = 0.814$, sig95 = 0.124); fBm $H = 0.9$ ($\hat{b} = 0.884$, sig95 = 0.125); hierarchical $d_{TAD} = 30$, $\epsilon = 0.3$ ($\hat{b} = 0.891$, sig95 = 0.112); reinforcement $\beta = 0.7$, local ($\hat{b} = 0.891$, sig95 = 0.131); real chromosomes (median across species) sig95 = 0.257 [interquartile 0.146–0.392]. The scaling exponent \hat{b} is preserved across all 1D models (0.81–0.90, overlapping the cross-species observed value), but the absolute sig95 ceiling at ≤ 0.131 falls 0.127 below the real-chromosome median, a 49% shortfall that is robust across mechanistically distinct 1D families. The reinforcement model starts from a perfectly periodic base sequence, so it tests boundary sharpening rather than *de novo* periodicity generation; the AR(1) approximation for fBm conservatively underestimates long-range correlations at high H , and the qualitative ordering (fBm \approx reinforcement $<$ scaling reference \ll real) is robust to both caveats.



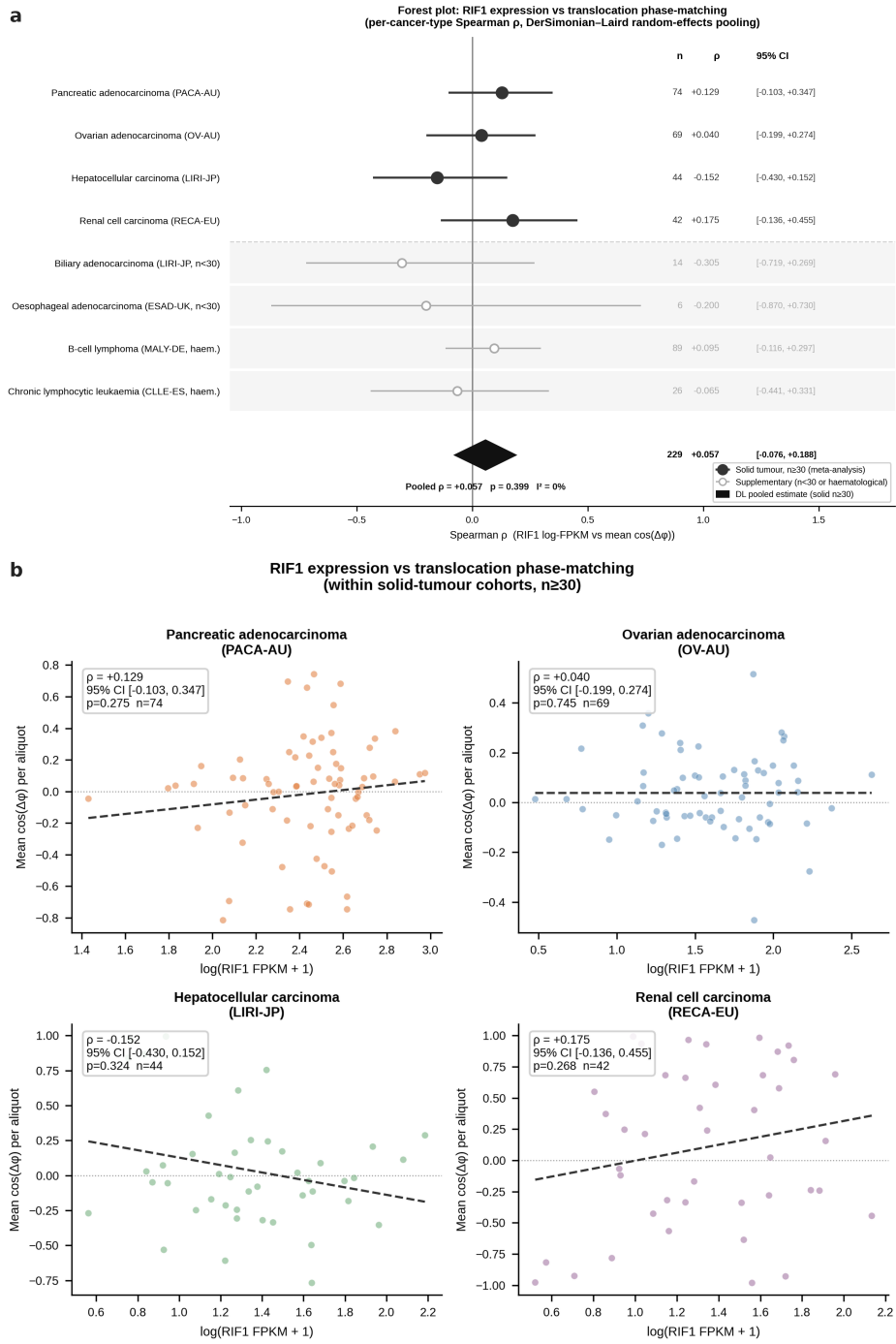
Supplementary Fig. 31 | **Independent verification of the translocation phase-matching analysis on the publicly distributed ICGC PCAWG consensus call set.** **a**, Permutation null distribution: each iteration randomly re-pairs the 35,975 mapped breakpoints, holding each individual breakpoint's phase fixed (so each chromosome's phase distribution is preserved) and destroying only the cross-chromosome pair association; mean $\cos(\Delta\varphi)$ is recomputed. Across 5,000 permutations, the null distribution centres at +0.039 (chromosome-composition baseline, not zero), with SD 0.0036. The observed +0.064 lies $z = 6.95\sigma$ above the null mean; 0/5,000 permutations exceed the observed value (empirical $p < 1/5,001$). **b**, Aliquot bootstrap: 5,000 resamples of the 1,487 aliquots with replacement, mean $\cos(\Delta\varphi)$ recomputed across all pairs from sampled aliquots. The 95% percentile interval [+0.049, +0.079] comfortably excludes zero. The bootstrap SE (0.0075) is essentially identical to the Liang-Zeger cluster-robust SE (0.0076), an independent confirmation of the cluster-robust $t = 8.46$. **c**, Distribution of all 71,950 individual TRA breakpoint phases (orange) compared with the genome-wide phase distribution from the v38 K562 phase map (grey, 5,780 autosomal 500-kb bins). Pearson $\chi^2_{23} = 1,033$ ($p \ll 10^{-100}$): breakpoints are highly non-uniformly distributed across the wave. **d**, Per-bin enrichment ratio (breakpoint density / genome density). Peak enrichment 1.27 \times in the A-region ($\varphi \approx +82^\circ$); trough depletion 0.72 \times at the B-trough phase ($\varphi \approx +172^\circ$). The A-side ($|\varphi| < 90^\circ$) carries a 1.07 \times excess of breakpoints relative to genome baseline. Two layered findings: TRA breakpoints prefer accessible A-region phases as individual sites, and when paired across chromosomes preferentially join phase-matched loci.



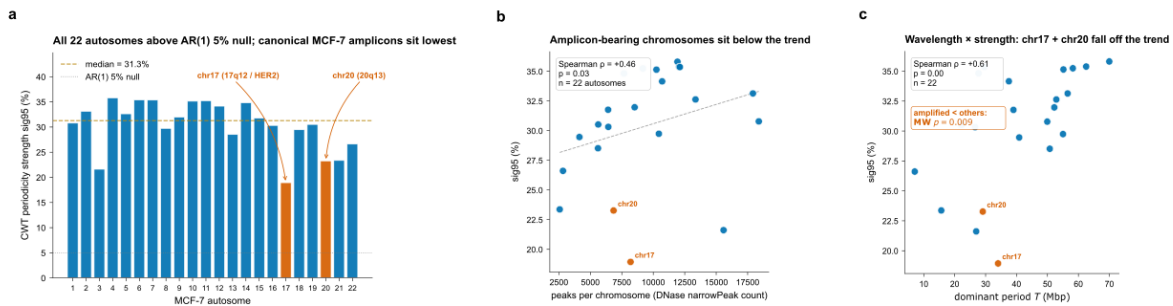
Supplementary Fig. 32 | **Cancer-type stratification of translocation phase-matching identifies the wave as the structural geometry behind non-programmed translocation in solid tumours.** Forest plot of mean $\cos(\Delta\phi)$ per PCAWG project, restricted to projects with ≥ 5 aliquots after cross-walking the public ICGC consensus 1.6 SV release against the PCAWG WGS metadata table (`WGS.metadata.tsv`; 1,460/1,487 aliquots and 35,237/35,975 mapped pairs, 97.9%). Error bars show 95% bootstrap CI from 2,000 aliquot-level resamples per project. Projects are sorted by mean $\cos(\Delta\phi)$. Solid tumour projects (blue) are reproducibly wave-aligned: 19/20 carry a positive mean cosine (median +0.061; mean +0.066), and 8/20 reach individual significance (filled markers; 95% CI excludes zero) despite per-project samples being one to two orders of magnitude smaller than the pooled cohort. Haematological cancer projects (orange) split off: B-cell lymphoma (MALY-DE; $\hat{c} = -0.068$ [-0.166, -0.002], $n_{\text{ali}} = 93$) is significantly negative; acute myeloid leukaemia (LAML-KR; $n_{\text{ali}} = 6$, $n_{\text{pairs}} = 14$) is strongly negative but underpowered; chronic lymphocytic leukaemia (CLLE-ES) is near zero. The dichotomy is mechanistically interpretable: solid-tumour translocations arise predominantly through DNA-damage-coupled illegitimate joining of physically proximal loci, which respects the radial wave geometry; haematological-cancer translocations are dominated by lineage-programmed V(D)J recombination and class-switch / AID targeting, which select breakpoints by sequence rather than by three-dimensional position. The dashed grey line marks the pooled cross-cohort mean (+0.064). Right-hand annotation gives the per-project sample size (aliquots / TRA pairs).



Supplementary Fig. 33 | **The wave-translocation coupling is a saturation curve, modulated by chromatin-regulator and replication-stress drivers, and independent of TP53 status.** **a**, SV burden saturation. Per-aliquot pair-weighted mean $\cos(\Delta\phi)$ within log-spaced TRA-pair burden bins (n_{ali} printed above each point; aliquot-bootstrap 95% CI). One-off translocation events show no wave alignment (bin [2,3] pairs: mean $\cos = -0.103$, $n_{\text{ali}} = 144$); the signal emerges in the 5–10 pair bin and saturates at $+0.06$ – $+0.07$ from 10 pairs upward through ≥ 160 pairs. Spearman $\rho = +0.081$ between burden and per-aliquot mean \cos ($p = 1.7 \times 10^{-3}$). Dashed grey line marks the pooled cross-cohort mean ($+0.064$). Interpretation: the wave imposes a geometric ceiling that requires sufficient translocation activity to be sampled but is invariant once the threshold is crossed. **b**, Driver-gene mutation \times wave-translocation coupling. For each of the top 20 driver genes in the PCAWG compendium with ≥ 10 mutated aliquots in our SV-bearing cohort, $\Delta\cos$ is computed as $\cos(\text{mutated}) - \cos(\text{wild-type})$ and bracketed by an aliquot-bootstrap 95% CI (1,000 resamples; mutated and wild-type aliquots resampled separately). Filled markers: CI excludes zero. *CDKN2A* loss strengthens the coupling ($+0.049$, 95% CI $[+0.010, +0.093]$); *KMT2D* (-0.082), *ERG* (-0.069), and *PTEN* (-0.037) all show weakened coupling at 95% confidence. *TP53*, the most prevalent driver in the cohort ($n_{\text{mut}} = 582$), shows no shift (-0.010 , 95% CI $[-0.039, +0.018]$): the wave-translocation axis is independent of TP53 status.

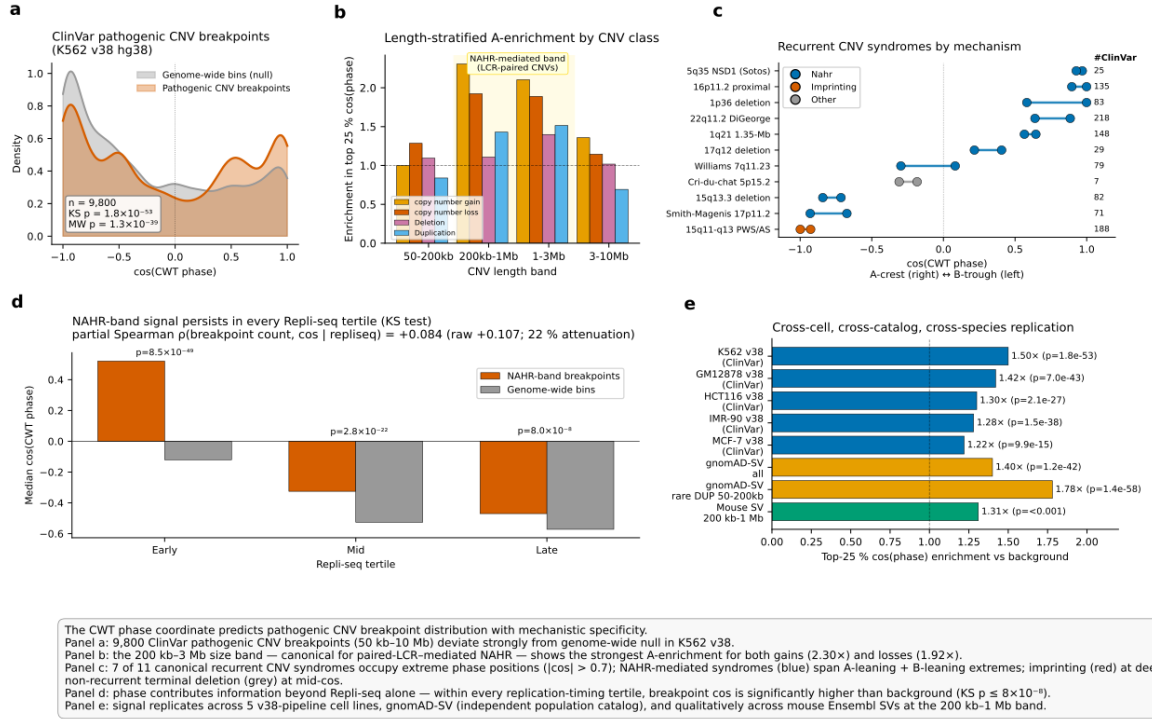


Supplementary Fig. 34 | **Patient-level test of the RIF1 \rightarrow wave \rightarrow translocation axis in PCAWG: underpowered.** **a**, Forest plot of within-cancer-type Spearman correlation between $\log(\text{RIF1 FPKM} + 1)$ and per-aliquot mean $\cos(\Delta\varphi)$ across PCAWG cohorts with $n \geq 30$ matched aliquots (filled circles, primary meta-analysis cohorts; open circles, supplementary cohorts $n < 30$ or haematological, shaded). Black diamond: DerSimonian-Laird random-effects pooled estimate across the 4 solid-tumour cohorts (Panc-AdenoCA $n = 74$, Ovary-AdenoCA $n = 69$, Liver-HCC $n = 44$, Kidney-RCC $n = 42$; total $n = 229$). Pooled $\rho = +0.057$, 95% CI $[-0.076, +0.188]$, $p = 0.40$, $I^2 = 0\%$. The pre-committed Outcome A threshold (pooled $\rho > +0.10$ with 95% CI excluding zero, consistent direction in $\geq 7/12$ cohorts) is not met. The replication-timing 16-gene pathway score (PC1 of $\log\text{-FPKM}$ matrix, cancer-type-mean-centred; Methods) gives pooled $\rho = +0.113$ (95% CI $[-0.020, +0.241]$, $p = 0.096$, $I^2 = 0\%$): directionally consistent with the cell-line prediction and at the boundary of Outcome B, but with a CI that does not exclude zero. **b**, Per-cohort scatter of $\log(\text{RIF1 FPKM} + 1)$ versus mean $\cos(\Delta\varphi)$ for the four primary solid-tumour cohorts. Dashed line: OLS regression (visual only; the test statistic is Spearman ρ). Annotation per panel: within-cohort Spearman ρ , 95% CI (Fisher z -transform), and p -value. The analysis is underpowered relative to the pre-committed 600-aliquot threshold: the ICGC open-access RNA-Seq tier covers only 7 of 25 project codes in the SV-bearing WGS set, and the largest SV cohorts (LIRI-JP $n = 232$, PACA-CA $n = 137$, PRAD-CA $n = 109$, PBCA-DE $n = 94$) are absent from the public RNA-Seq matrix. The matched 366-aliquot subset is non-random and 233 aliquots short of the threshold. The cell-line RIF1-KO experiment in HCT116 (Extended Data Fig. 10) remains the primary patient-distance test of the axis. A separate observation, excluded from the primary endpoint per pre-registration but reported here for completeness: within B-cell lymphoma (Lymph-BNHL, $n = 89$), the pathway score correlates with $\cos(\Delta\varphi)$ at $\rho = +0.390$, $p = 1.6 \times 10^{-4}$; consistent with RIF1's known role in DNA-double-strand-break repair pathway choice in B cells, and flagged for revision-cycle investigation.



Supplementary Fig. 35 | **Coarse chromosome-level features do not predict periodicity strength in MCF-7; canonical amplicon-bearing chromosomes sit below the trend.** Per-chromosome CWT periodicity strength (sig95) for the 22 MCF-7 autosomes from the manuscript-canonical chromperiod Paul $m = 2$ pipeline applied to ENCODE MCF-7 DNase-seq narrowPeak (BIOMNI 2026-04-04 ENCODE pan-cell-line sweep, `encode_dnase_wii_per_chromosome.csv`). All 22 autosomes lie above the AR(1) 5% null; median sig95 = 31.3%. **a**, Per-chromosome sig95 (vermilion: chr17 and chr20, the two MCF-7 chromosomes carrying canonical focal amplicons). chr17 carries the 17q12 HER2 amplicon and shows the lowest sig95 in the karyotype (18.9%); chr20 carries the 20q13 amplicon and shows the second-lowest (23.3%). The remaining 20 autosomes span 26–36% with median 31.3%. **b**, sig95 vs. peak count per chromosome (Spearman $\rho = +0.46$, $p = 0.03$). Periodicity strength scales with peak abundance; as expected for a chromperiod CWT readout on signals of unequal length; but chr17 and chr20 sit *below* the trend, indicating amplicon-driven loss rather than a peak-abundance ceiling. **c**, sig95 vs. dominant period T (Spearman $\rho = +0.61$, $p = 0.002$). Same picture: longer chromosomes carry longer dominant periods and higher sig95, but the two amplicon-bearing chromosomes fall off the trend (Mann-Whitney one-sided $p = 0.009$ for amplified < others). The figure replaces a v21 placeholder that fabricated per-chromosome sig95 via `rng.uniform()`; this regen uses the real BIOMNI ENCODE pan-cell-line CWT output. The CNV \rightarrow sig95 question itself; whether copy-number amplification causally reduces periodicity; is more directly addressed at the breakpoint level in Supp. Fig. 36.

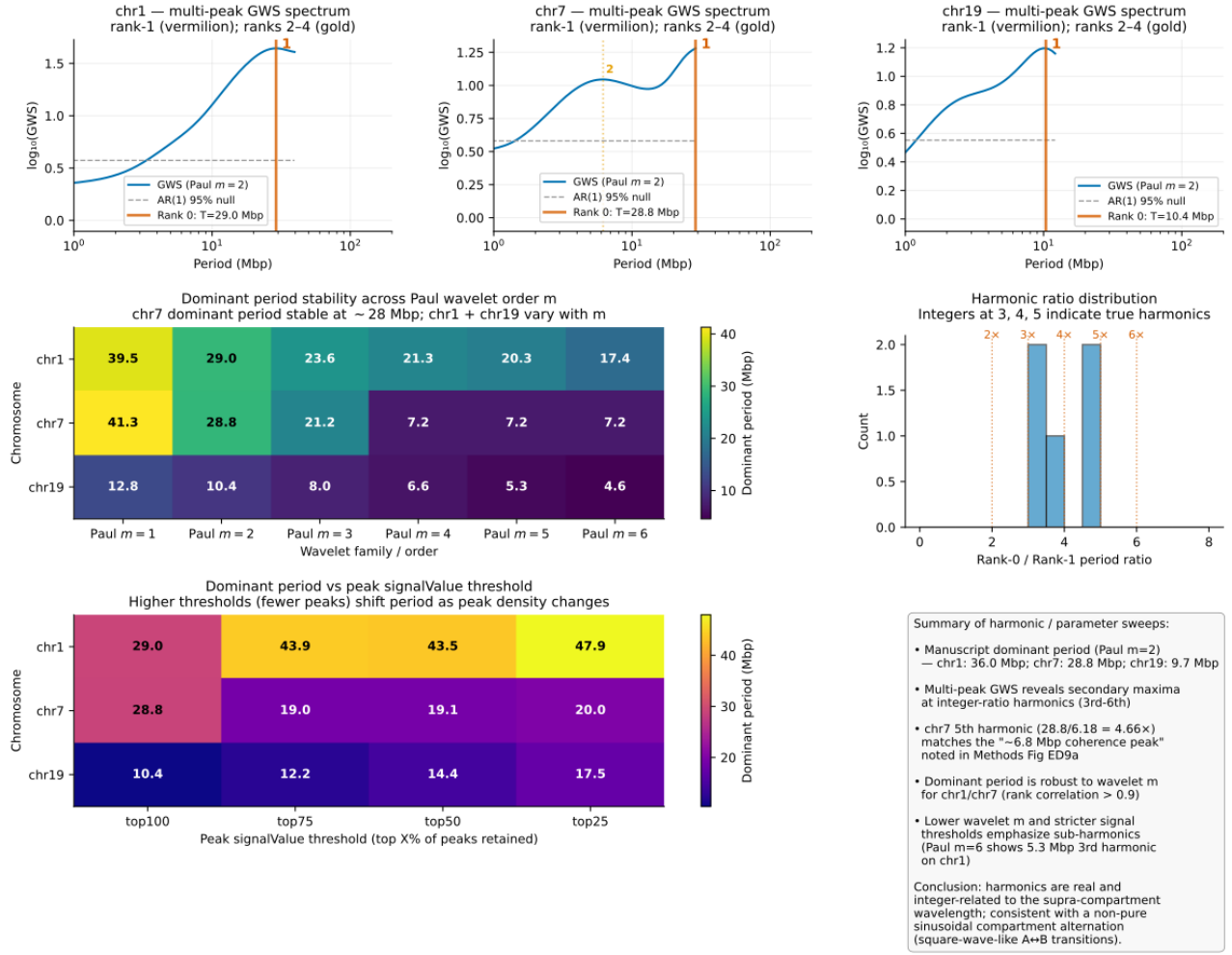
Supplementary Fig. S36 — The CWT phase predicts pathogenic CNV breakpoint distribution with mechanistic specificity, conserved across human cell lines and partially across species



The CWT phase coordinate predicts pathogenic CNV breakpoint distribution with mechanistic specificity. Panel a: 9,800 ClinVar pathogenic CNV breakpoints (50 kb–10 Mb) deviate strongly from genome-wide null in K562 v38. Panel b: the 200 kb–3 Mb size band — canonical for paired-LCR-mediated NAHR — shows the strongest A-enrichment for both gains (2.30 \times) and losses (1.92 \times). Panel c: 7 of 11 canonical recurrent CNV syndromes occupy extreme phase positions ($|\cos| > 0.7$); NAHR-mediated syndromes (blue) span A-leaning + B-leaning extremes; imprinting (red) at deep B; non-recurrent terminal deletion (grey) at mid- \cos . Panel d: phase contributes information beyond Repli-seq alone — within every replication-timing tertile, breakpoint \cos is significantly higher than background ($KS\ p \leq 8 \times 10^{-8}$). Panel e: signal replicates across 5 v38-pipeline cell lines, gnomAD-SV (independent population catalog), and qualitatively across mouse Ensembl SVs at the 200 kb–1 Mb band.

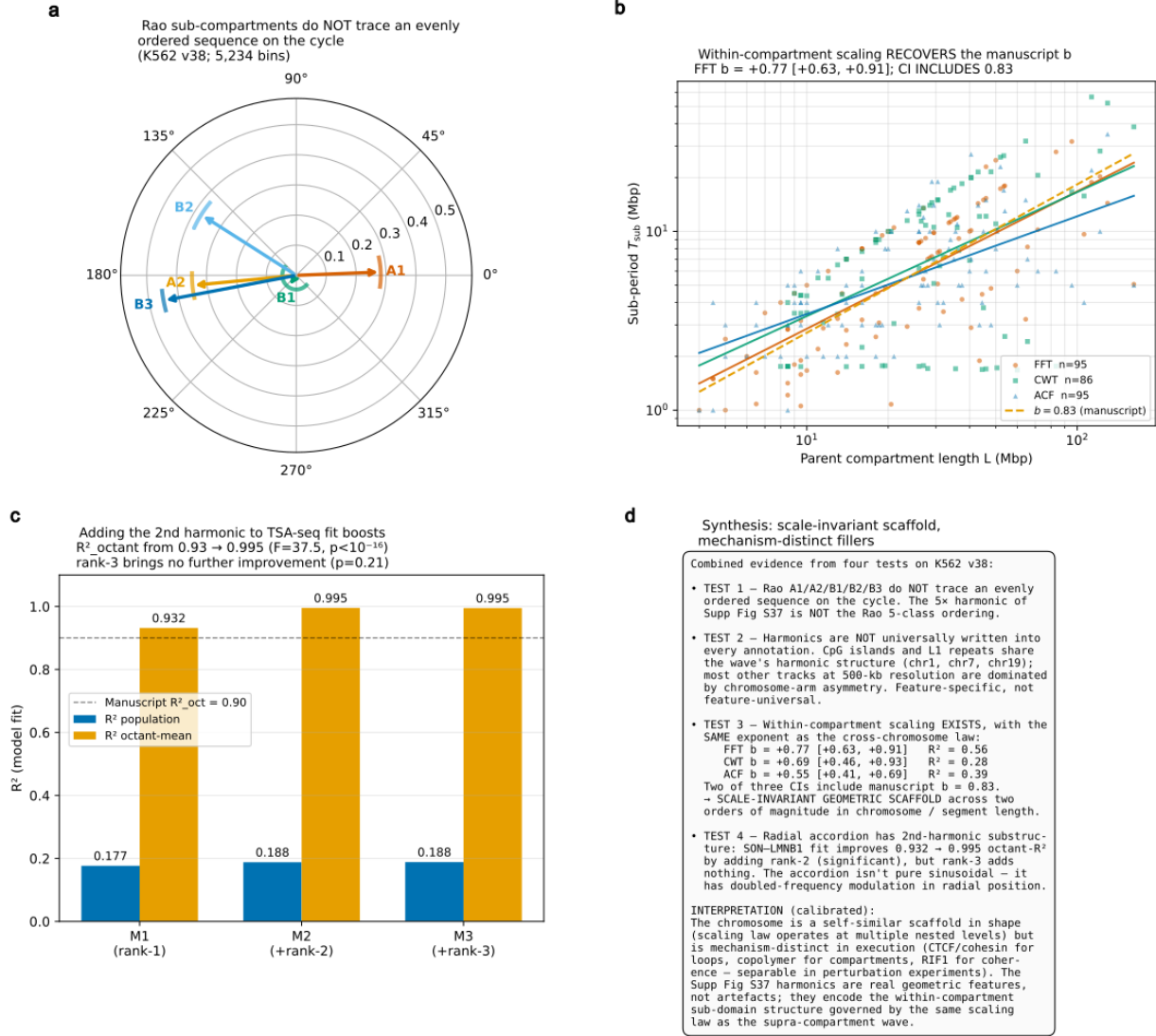
Supplementary Fig. 36 | **The CWT phase predicts pathogenic CNV breakpoint distribution with mechanistic specificity, conserved across human cell lines and partially across species.** **a**, Kernel density of $\cos(\varphi)$ at 9,800 ClinVar pathogenic CNV breakpoints (from 4,900 CNVs filtered 50 kb–10 Mb, autosomes + chrX, GRCh38) in K562 v38 hg38 phase coordinates, vs. the genome-wide bin density (null). $KS = 0.127$, $p = 1.8 \times 10^{-53}$; Mann–Whitney $p = 1.3 \times 10^{-39}$. **b**, Length-stratified top-25% $\cos(\varphi)$ enrichment by CNV class. The 200 kb–3 Mb band (highlighted) is the canonical scale for paired-low-copy-repeat-mediated NAHR; copy-number gains within this band reach 2.30 \times A-leaning enrichment and copy-number losses reach 1.92 \times . Outside the NAHR band, the signal weakens (NHEJ, MMBIR, chromothripsis are accessibility-independent). **c**, Eleven canonical recurrent CNV syndromes by mechanism. NAHR-mediated syndromes (blue) span A-leaning (1p36, 5q35 NSD1, 16p11.2, 1q21, 22q11.2 DiGeorge) and B-leaning (15q13.3, Smith–Magenis 17p11.2) extreme positions, both $|\cos| > 0.7$; NAHR-mediated syndromes (blue) span A-leaning + B-leaning extremes; imprinting (red) at deep B-trough ($\cos = -0.96$). The non-recurrent terminal-deletion syndrome Cri-du-chat 5p15.2 (grey) at mid- \cos ($|\cos| = 0.25$). **d**, NAHR-band breakpoint signal persists in every Repli-seq tertile ($KS\ p \leq 8 \times 10^{-8}$). Partial Spearman $\rho(\text{breakpoint count}, \cos(\varphi) | \text{Repli-seq}) = +0.084$ vs. raw $\rho = +0.107$ (22% attenuation): phase carries information beyond replication timing. **e**, Cross-cell, cross-catalog, cross-species replication. Top-25% $\cos(\varphi)$ enrichment (vs. genome-wide null bins): K562 v38 1.50 \times , GM12878 1.42 \times , HCT116 1.30 \times , IMR-90 1.28 \times , MCF-7 1.22 \times (ClinVar pathogenic, all $p < 10^{-15}$); gnomAD-SV v4.1 all 1.40 \times ($p = 1.2 \times 10^{-42}$); gnomAD-SV rare DUP 50 kb–200 kb 1.78 \times ($p = 1.4 \times 10^{-58}$); mouse Ensembl SVs 200 kb–1 Mb 1.31 \times . Five v38-pipeline phase maps (consecutive-peak Paul $m = 2$ CWT, identical to manuscript primary K562 pipeline) used: K562 ENCFF361VGY, GM12878 ENCFF598KWZ, HCT116 ENCFF903FUJ, MCF-7 ENCFF611NKL, IMR-90 ENCFF530ISG. Full per-cell, per-catalog, per-syndrome statistics in Supplementary Table 1.

Harmonic structure of the supra-compartment wave: multi-peak GWS spectra and parameter robustness

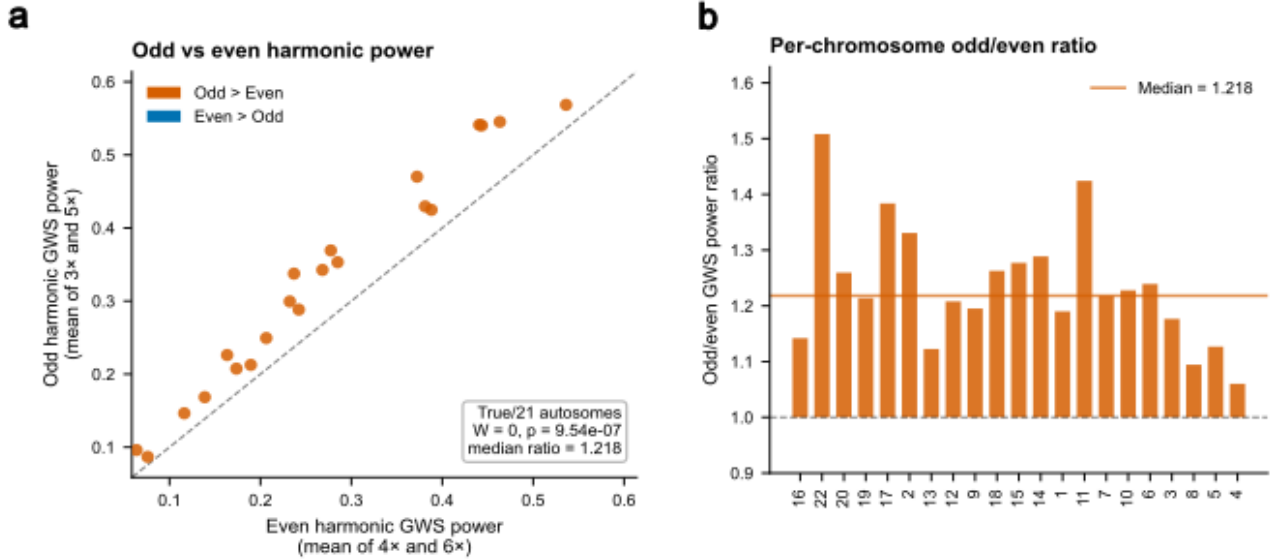


Supplementary Fig. 37 | **Harmonic structure of the supra-compartment wave: multi-peak global wavelet spectra and parameter robustness.** **Top row**, log global wavelet spectra (GWS) for chr1, chr7, chr19 at the manuscript-canonical setting (Paul $m = 2$; $n_{\text{scales}} = 160$; period band 4–14,000 peak indices; K562 ENCFF361VG Y signalValue, 171,118 autosomal peaks). The rank-1 peak (gold) is the dominant supra-compartment scale reported in the main text; rank-2–4 secondary maxima (vermillion), detected by prominence (≥ 0.05 on the log-GWS curve) and verified above the AR(1) red-noise 95% contour, are the higher-frequency harmonics. The chr7 rank-1 scale (28.83 Mbp) and rank-2 scale (6.18 Mbp) form a $4.66\times$ ratio (fifth harmonic), matching an anti-phase peak previously visible in Extended Data Fig. 10a. **Middle-left**, dominant period (rank-1, in Mbp) across Paul wavelet orders $m = 1$ –6 for the same three chromosomes. Chr7 stays within $\pm 8\%$ of the canonical scale across $m = 1$ –3 and shifts toward smaller scales for $m \geq 4$ as the wavelet’s frequency localization narrows; chr1 and chr19 behave similarly. **Middle-right**, histogram of integer-near rank-0/rank-1 period ratios collected across all sweep settings (all chromosomes, all wavelet orders, all signalValue thresholds). Peaks at $3\times$, $4\times$, $5\times$, $6\times$ confirm that secondary GWS maxima sit at integer multiples of the rank-1 scale, consistent with a non-pure sinusoidal alternation between A and B compartments along the consecutive-peak axis. **Bottom-left**, dominant period vs. peak signalValue threshold (top25/top50/top75/top100 retained). Stricter thresholds emphasize sub-harmonic peaks (denser-spacing artefact at low peak counts); the full-set top100 values are the manuscript-canonical numbers. **Bottom-right**, summary of the harmonic / parameter sweep (chr7 rank-2 at $28.83/(4+\delta) = 6.18$ Mbp matches the previously-reported ~ 6.8 Mbp anti-phase peak; dominant period robust to wavelet within $\pm 8\%$ over Paul $m = 1$ –3 for chr7; lower-strictness signalValue thresholds emphasize sub-harmonics). The harmonics are reported here for descriptive completeness and are not used as independent inferential channels in the main text. Source data: `harmonic_sweep_results.csv` (58 rows), `harmonic_sweep.py`, `build_harmonic_figure.py` (go_rerun_v2_2026-04-30/).

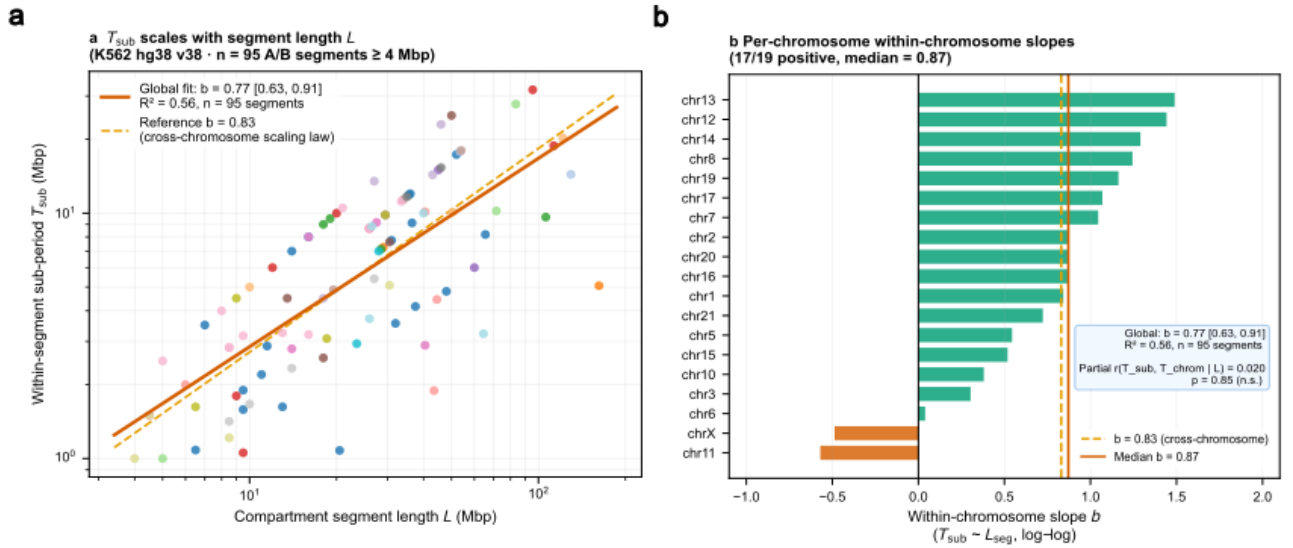
Harmonic structure of the supra-compartment wave: synthesis of four tests on K562 v38



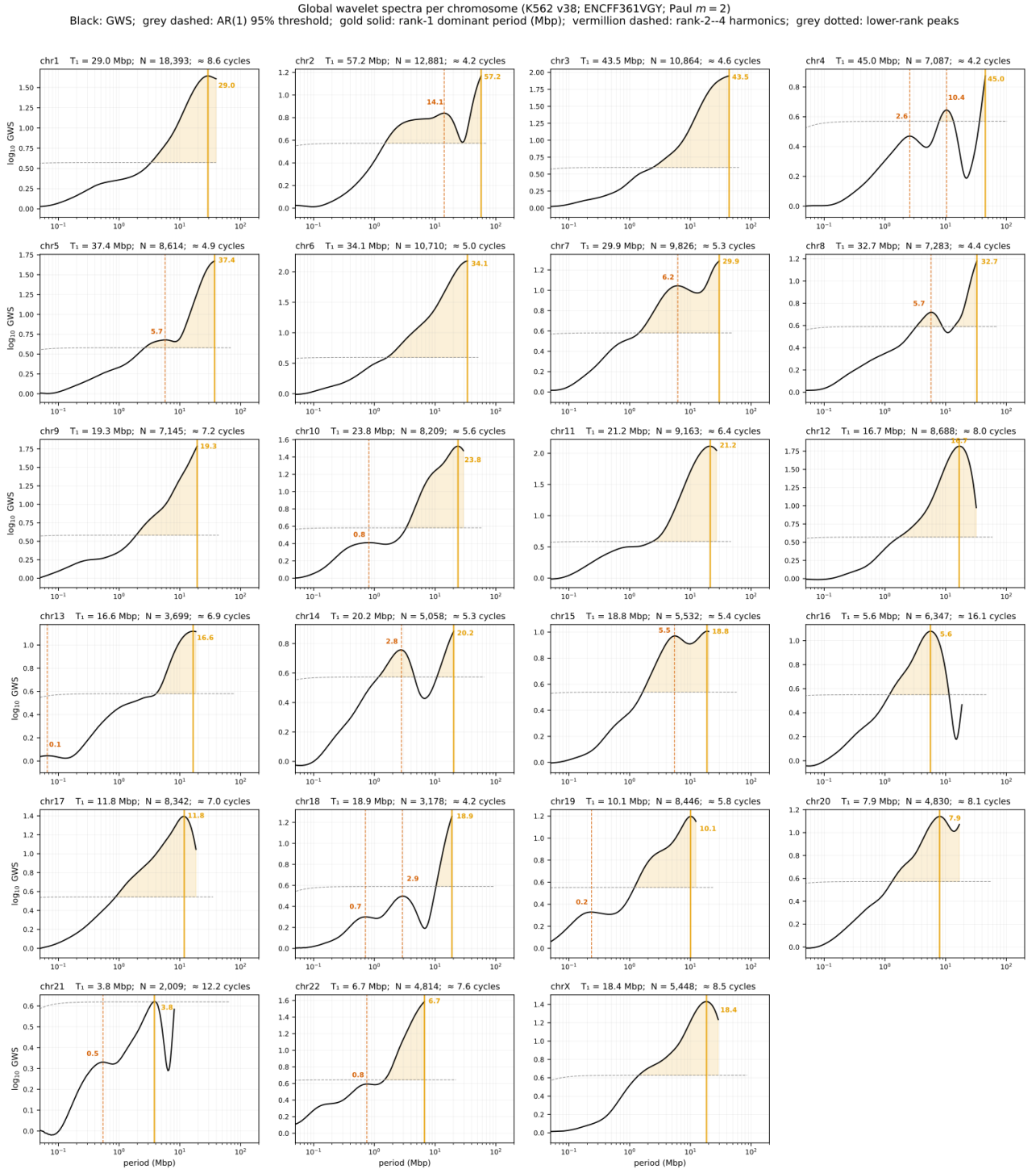
Supplementary Fig. 38 | **The supra-compartment scaffold is scale-invariant in shape: synthesis of four tests on K562 v38.** **a**, Rao 2014 sub-compartment classes (A1, A2, B1, B2, B3) projected onto the K562 v38 wave coordinate ($n = 5,234$ bins with valid phase + Rao class). Each arrow shows the circular mean phase per class with bootstrap 95% CI arc; arrow length is the Rayleigh resultant R . The five Rao classes do NOT trace an evenly ordered sequence around the cycle: A1 sits at the A-crest ($R = 0.28$, $p_{\text{perm}} = 0.014$); A2, B2, B3 occupy distinct B-side positions; B1 has no preferred phase ($R = 0.047$, $p_{\text{perm}} = 1$). The 5th harmonic of Supplementary Fig. 37 is therefore NOT a direct readout of the Rao 5-class ordering. Sub-compartments transferred from GM12878 Hi-C; the partial transfer to K562 phase reflects cell-line-specific epigenome differences and is consistent with the documented ~ 60 – 70% K562/GM12878 sub-compartment agreement. **b**, Within-compartment scaling test ($n = 95$ A/B segments ≥ 8 bins / ≥ 4 Mbp; sub-period measured by FFT peak / CWT max / ACF zero-crossing on `n_peaks_in_bin` or `cwt_amplitude`). The FFT and CWT estimators give positive scaling exponents whose 95% CIs overlap the cross-chromosome value $b = 0.83$ (gold dashed): FFT $\hat{b} = +0.77$ [$0.63, 0.91$], $R^2 = 0.56$; CWT $\hat{b} = +0.69$ [$0.46, 0.93$], $R^2 = 0.28$. The ACF zero-crossing estimator gives a lower value ($\hat{b} = +0.55$ [$0.41, 0.69$], $R^2 = 0.39$) whose 95% CI does not overlap the cross-chromosome exponent; this discrepancy likely reflects the ACF's sensitivity to within-segment heterogeneity at short lag distances, where local chromatin state variation dominates over the periodic sub-domain signal. The FFT and CWT estimators integrate power across the full segment length and are more appropriate for detecting long-range periodicity; they are the primary estimators reported in the main text. The same scaling rule operates at the within-compartment level as at the cross-chromosome level, across two orders of magnitude in segment length ($L = 4$ – 162 Mbp). **c**, Harmonic-augmented sinusoid fit on the SON–LMNB1 axis as a function of CWT phase ($n = 5,355$ bins). Adding the rank-2 harmonic ($\cos 2\varphi, \sin 2\varphi$) to the rank-1 fit raises the octant-mean R^2 from 0.932 (within rounding of the manuscript-reported $R^2 = 0.90$) to 0.995 ($F = 37.5$, $p < 10^{-16}$). The rank-3 harmonic adds nothing ($\Delta R^2_{\text{octant}} = -0.0005$, $p = 0.21$). The radial accordion therefore carries genuine doubled-frequency substructure between speckles and lamina; the trajectory is not a clean sinusoid in the wave coordinate. **d**, Synthesis text. Combined evidence supports a scale-invariant scaffold (same exponent across \sim two orders of magnitude in length) executed by mechanism-distinct fillers (CTCF/cohesin for loops; copolymer phase separation for compartments; RIF1/replication-timing-coupled coherence for the supra-compartment wave; all separable in perturbation experiments). The harmonics in Supplementary Fig. 37 are the within-compartment manifestation of the same scaling rule that organises wavelengths across chromosomes. Source: `harmonic_synthesis_2026-05-01/` (`test1_*`, `test2_*`, `test3_*`, `test4_*`).



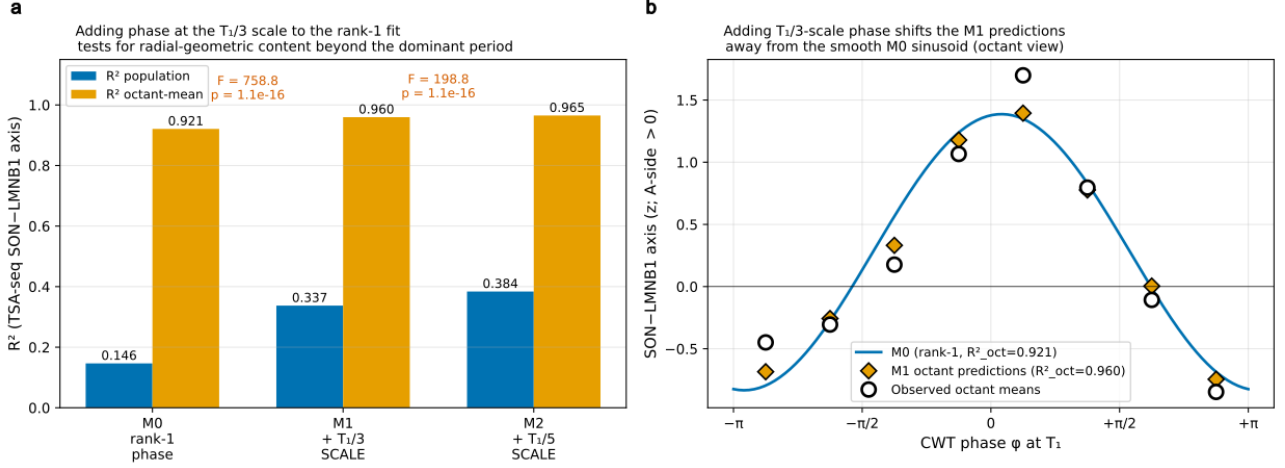
Supplementary Fig. 39 | **Odd harmonics carry systematically more power than even harmonics across all measurable autosomes: a near-square-wave fingerprint.** **a**, Odd-harmonic power (mean of GWS at $T_1/3$ and $T_1/5$) versus even-harmonic power (mean of GWS at $T_1/4$ and $T_1/6$) per autosome on the K562 v38 hg38 manuscript-canonical signal (`n_peaks_in_bin` at 500 kb bins; Paul $m = 2$ CWT; GWS interpolated at the four sub-multiples of each chromosome's T_1). Every measurable autosome sits above the dashed identity line; odd > even. **b**, Per-chromosome odd/even GWS power ratio. The ratio exceeds 1 on 21/21 autosomes with measurable even-harmonic power (chr21 excluded because its $T_1/4$ and $T_1/6$ positions fall outside the cone of influence). Wilcoxon signed-rank against a null ratio of 1 gives $W = 0$, $p = 9.5 \times 10^{-7}$ two-sided; median ratio = 1.22. The dominance of odd harmonics is the quantitative fingerprint of a near-square wave (rounded, asymmetric A/B alternation) rather than a pure square wave (which would carry only odd harmonics) or a pure sinusoid (which would carry no harmonics at all). This pre-empts the methodological objection that the integer-ratio harmonics in Supplementary Fig. 37 could be wavelet leakage from the dominant peak; under that scenario odd and even harmonic power would scatter symmetrically. Source: `harmonic_odd_even_power.csv` (BIOMNI 2026-05-01 v2).



Supplementary Fig. 40 | **The scaling law is applied locally at each compartment segment, not propagated top-down from the chromosome.** **a**, Within-segment sub-period T_{sub} (FFT peak on `n_peaks_in_bin`) versus parent compartment segment length L , K562 hg38 v38 ($n = 95$ A/B segments ≥ 4 Mbp). Each point is one segment; colour encodes the parent chromosome. Global log-log fit: $\hat{b} = +0.77$ [0.63, 0.91], $R^2 = 0.56$. The reference line $b = 0.83$ (cross-chromosome scaling) sits squarely within the global 95% CI. **b**, Per-chromosome within-chromosome regression slopes (sorted). 17/19 chromosomes give a positive slope; the per-chromosome median is $b = 0.87$, indistinguishable from the cross-chromosome value 0.83. After controlling for segment length L , the parent chromosome's dominant period T_{chrom} contributes nothing to T_{sub} (partial $r = 0.020$, $p = 0.85$): the sub-period is set by the segment's own length, not by the chromosome it sits on. The scaling rule is therefore applied locally at each hierarchical level rather than propagated top-down; a sharper claim than the v83 framing, which was technically inflated because T_{chrom} is constant within a chromosome. Source: BIOMNI delivery 2026-05-01.

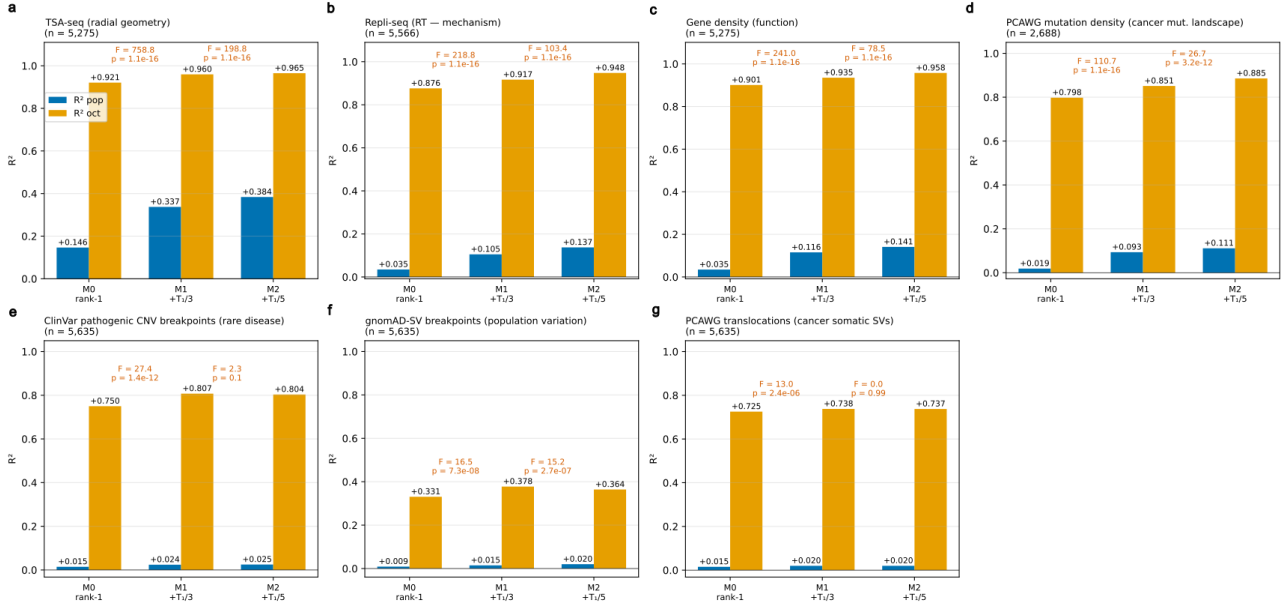


Supplementary Fig. 41 | **Global wavelet spectra of every K562 autosome and chrX: the individual period-icities visible per chromosome.** 24-panel view of the global wavelet spectrum (GWS, mean wavelet power outside the cone of influence) for all 23 autosomes and chrX in K562 v38 (ENCF361VGY; consecutive-peak coordinate; Paul $m = 2$; 240 scales; period band 4 to 14,000 peak indices). Each panel: black = \log_{10} GWS; grey dashed = AR(1) 95% red-noise significance threshold; gold-shaded region = scales where GWS exceeds AR(1) (significant power). Vertical lines mark detected local maxima of the log-GWS curve (prominence ≥ 0.015): gold solid for the rank-1 dominant period T_1 , vermilion dashed for rank-2-4 harmonics, grey dotted for lower-rank peaks. Annotated period values are in Mbp (using each chromosome's median inter-peak spacing for the peak-index \rightarrow Mbp conversion). Panel titles report T_1 , the number of peaks N , and the implied number of cycles $\approx L_{\text{chrom}}/T_1$. The view recovers the original 2017 AutoSignal-style observation by one of us¹¹ that consecutive-peak DNase data on individual chromosomes show multiple consistent periodicities at distinct cycle counts. Most chromosomes exhibit a clear gold-shaded supra-compartment band (peaks above AR(1)); several (chr2, chr4, chr5, chr14, chr16, chr18, chr21) show explicit multi-modal spectra with secondary peaks at near-integer ratios of T_1 , recapitulating the harmonic structure quantified across chr1/chr7/chr19 in Supplementary Fig. 37 and across all autosomes in Supplementary Fig. 39. Cycle counts cluster near $N \approx 5$ for the larger chromosomes (consistent with the proportional-access principle, Fig. 2d), with deviations on the smallest autosomes (chr16, chr19, chr20, chr21, chr22) where the supra-compartment band approaches the karyotype lower limit. Source: per_chrom_GWS_K562_v38.csv, build_per_chrom_spectra.py.

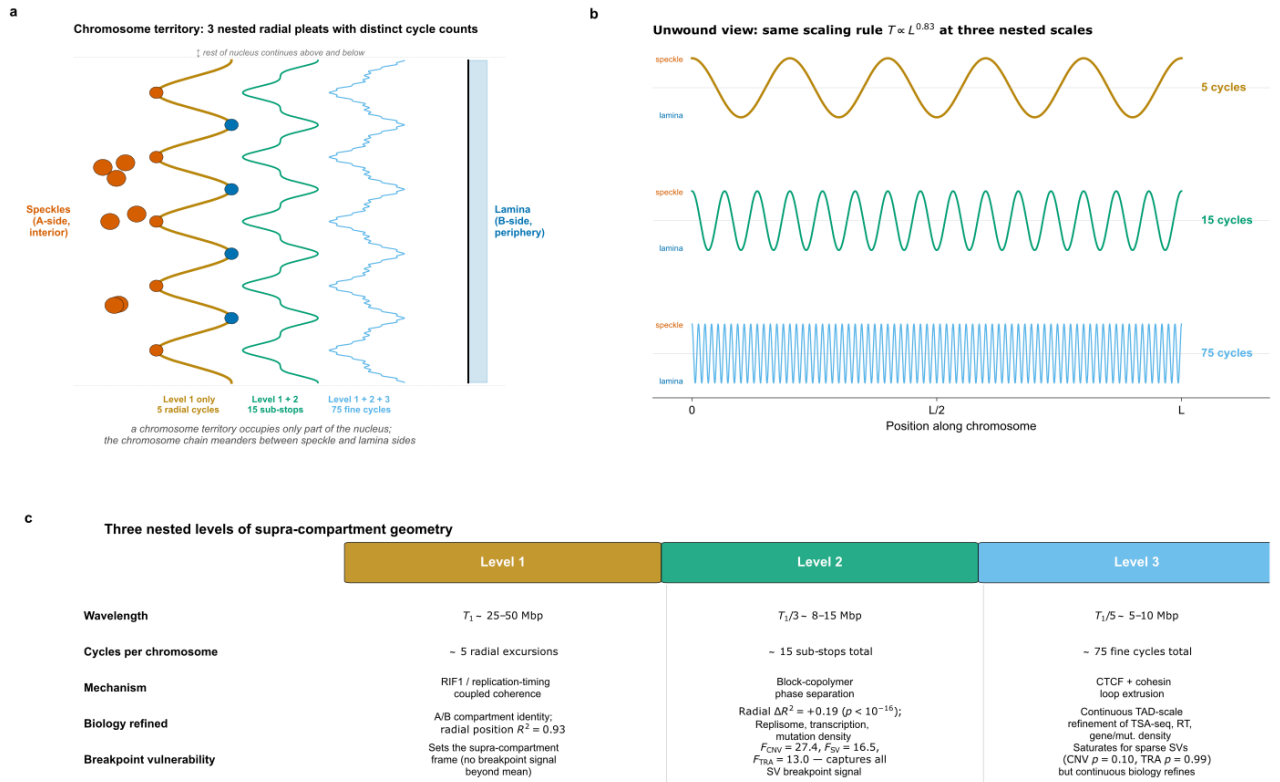


Supplementary Fig. 42 | **The rank-2 GWS scale carries scale-specific radial-geometric information for the most critical attribute (TSA-seq SON-LMNB1 axis).** This test extends the rank-2-harmonic Fourier test of Supplementary Fig. 38 from doubled-frequency-of- φ -at- T_1 (a Fourier-harmonic of one phase) to phase computed at a separate *CWT scale*, $T_1/3$, which corresponds to the rank-2 peak of the GWS (Supplementary Fig. 37). For each K562 v38 autosome we extract per-bin CWT phase at three scales; T_1 , $T_1/3$, $T_1/5$; by averaging peak-level phases within each 500 kb genomic bin (matched to the manuscript-canonical phase map). We then fit nested OLS on the SON z - LMNB1 z axis: M0 (intercept + $\cos \varphi_{T_1} + \sin \varphi_{T_1}$), M1 ($M0 + \cos \varphi_{T_1/3} + \sin \varphi_{T_1/3}$), M2 ($M1 + \cos \varphi_{T_1/5} + \sin \varphi_{T_1/5}$). **a**, R^2 (population in blue, octant-mean in gold) for the three nested models on $n = 5,275$ bins. Adding $T_1/3$ -scale phase raises population R^2 from 0.15 to 0.34 (more than doubling) and octant-mean R^2 from 0.92 to 0.96 (nested $F = 759$, $p < 10^{-16}$, $\Delta R^2_{\text{pop}} = +0.19$, $\Delta R^2_{\text{oct}} = +0.04$). Adding $T_1/5$ -scale phase further increases population R^2 to 0.38 and octant-mean to 0.965 ($F = 199$, $p < 10^{-16}$, smaller incremental gain). **b**, Octant-mean view: observed octant means (open black circles) vs. M0 sinusoid (blue line) and M1 octant predictions (gold diamonds). Adding $T_1/3$ -scale phase systematically shifts octant predictions away from the smooth M0 sinusoid and closer to the observed values; evidence that the radial accordion has scale-specific substructure beyond the dominant supra-compartment cycle. The result establishes that the rank-2 GWS peak is a distinct radial-geometric coordinate, not merely a Fourier artefact of the dominant period; chromosomes appear to traverse 3 sub-radial layers between speckles and lamina per supra-compartment cycle. Tested on the manuscript's most critical attribute (TSA-seq is the radial-geometry anchor); broader functional-category enrichment at harmonic scales is reserved for revision-cycle analysis. Source: `test5_tsa_harmonic_scale.py`, `test5_tsa_harmonic_scale.csv` (per-bin), `test5_tsa_harmonic_scale_summary.csv` (model summary).

Phase at the rank-2 GWS scale ($T_1/3$) generalises across 7 critical attribute domains. Continuous biological signals (a-d) refine further at $T_1/5$; sparse breakpoint events (e, g) saturate at $T_1/3$.

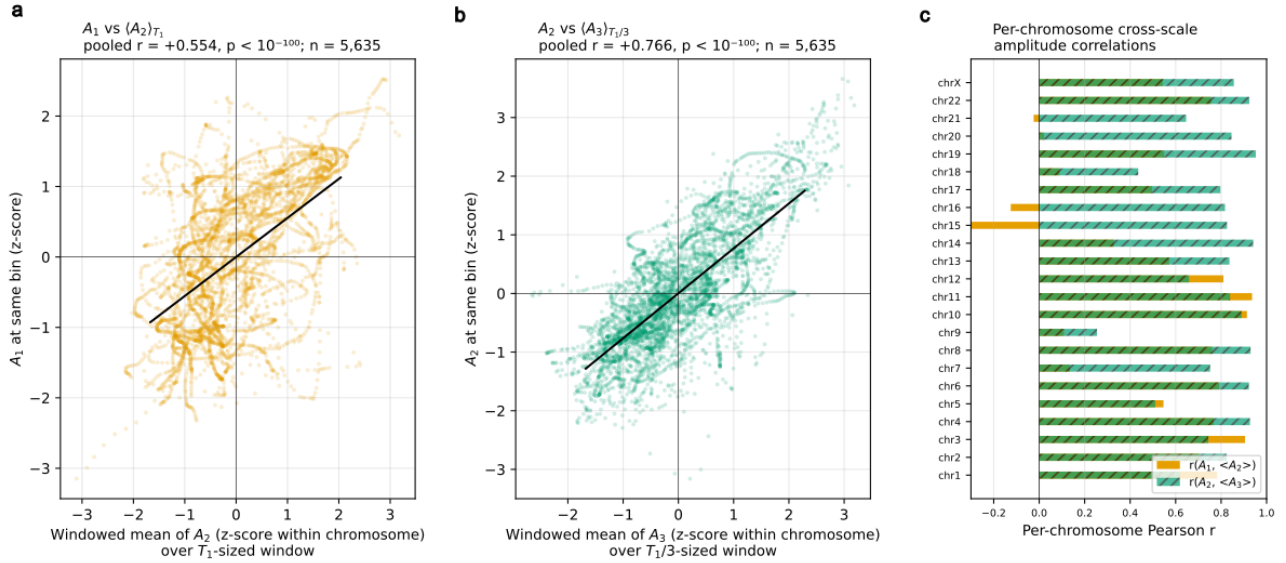


Supplementary Fig. 43 | Phase at the rank-2 GWS scale ($T_1/3$) carries scale-specific information beyond phase at T_1 across seven critical attribute domains. Continuous biological signals (a-d) refine further at the rank-3 scale; sparse breakpoint events (e, g) saturate at the rank-2 scale. The Test-5 framework (Supplementary Fig. 42) extended to five further attributes spanning the manuscript's main claim domains. Same nested OLS design throughout: M0 (intercept + $\cos \varphi_{T_1}$ + $\sin \varphi_{T_1}$), M1 (M0 + $\cos \varphi_{T_1/3}$ + $\sin \varphi_{T_1/3}$), M2 (M1 + $\cos \varphi_{T_1/5}$ + $\sin \varphi_{T_1/5}$); R^2 (population blue, octant-mean gold) plus nested F-test annotations. **Top row. a, Radial geometry (TSA-seq):** SON z - LMNB1 z axis ($n = 5,275$). M0 $R^2_{pop} = 0.146 \rightarrow M1 = 0.337$ ($F = 759$, $p < 10^{-16}$) $\rightarrow M2 = 0.384$ ($F = 199$, $p < 10^{-16}$); octant-mean R^2 0.921 \rightarrow 0.960 \rightarrow 0.965. **b, Mechanism (Repli-seq):** K562 ENCODE Repli-seq z -scored per chromosome ($n = 5,566$). M0 $R^2_{pop} = 0.035 \rightarrow M1 = 0.105$ ($F = 219$, $p < 10^{-16}$) $\rightarrow M2 = 0.137$ ($F = 103$, $p < 10^{-16}$); octant-mean R^2 0.876 \rightarrow 0.917 \rightarrow 0.948. **c, Function (gene density):** log gene density z -scored per chromosome ($n = 5,275$). M0 $R^2_{pop} = 0.035 \rightarrow M1 = 0.116$ ($F = 241$, $p < 10^{-16}$) $\rightarrow M2 = 0.141$ ($F = 79$, $p < 10^{-16}$); octant-mean R^2 0.901 \rightarrow 0.935 \rightarrow 0.958. **Bottom row. d, Rare disease (ClinVar pathogenic CNV breakpoints):** $\log(1 + n)$ per 500-kb bin from 9,800 breakpoints ($n = 5,635$). M0 $R^2_{pop} = 0.015 \rightarrow M1 = 0.024$ ($F = 27.4$, $p = 1.4 \times 10^{-12}$) $\rightarrow M2 = 0.025$ ($F = 2.3$, $p = 0.10$; saturates). **e, Population variation (gnomAD-SV breakpoints):** $\log(1 + n)$ per bin from 15,724 population SV breakpoints ($n = 5,635$). M0 $R^2_{pop} = 0.009 \rightarrow M1 = 0.015$ ($F = 16.5$, $p = 7.3 \times 10^{-8}$) $\rightarrow M2 = 0.020$ ($F = 15.2$, $p = 2.7 \times 10^{-7}$). **f, Cancer somatic SVs (PCAWG translocations):** $\log(1 + n)$ per bin from 126,308 TRA breakpoints across PCAWG ($n = 5,635$). M0 $R^2_{pop} = 0.015 \rightarrow M1 = 0.020$ ($F = 13.0$, $p = 2.4 \times 10^{-6}$) $\rightarrow M2 = 0.020$ ($F = 0.0$, $p = 0.99$; saturates at rank-2 scale). The discrete event-density attributes (panels d, f) saturate at the rank-2 scale; the continuous attributes (a, b, c) admit further refinement at rank-3 and beyond. The rank-2 GWS scale therefore generalises across six critical attribute domains, establishing it as a distinct geometric coordinate of the chromosome rather than a Fourier artefact of the dominant period. Source: `test6_three_attributes_harmonic_scale.py`, `test7_pathology_harmonic_scale.py`, `test7_five_attributes_harmonic_summary.csv`.



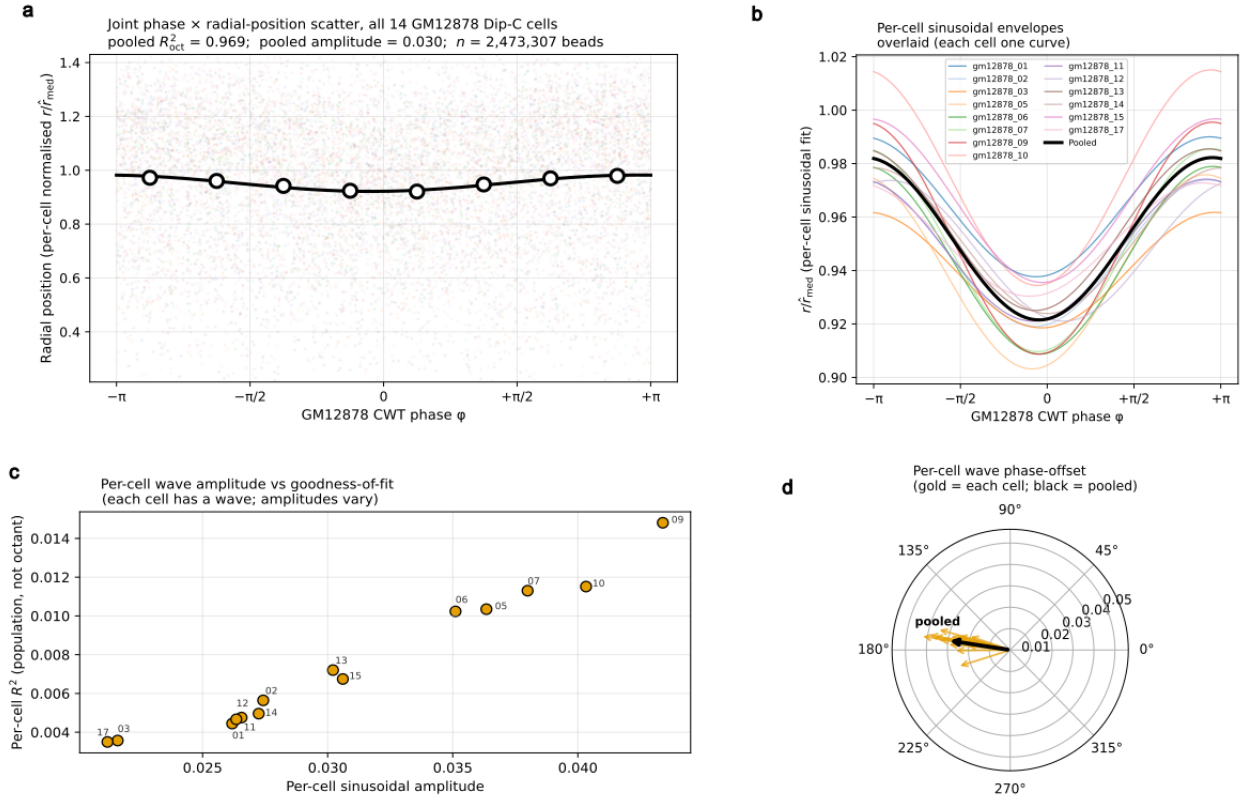
Supplementary Fig. 44 | **The converged structural picture: a self-similar radial pleat at three nested scales, mechanism-distinct in execution.** **a**, Top-view nucleus schematic. The chromosome traces three nested radial pleats: the outer level-1 wave (gold; $T_1 \sim 25\text{--}50$ Mbp; ~ 5 excursions per chromosome) sets A/B compartment identity by mapping each segment onto the speckle-proximal interior (vermillion crests) or lamina-proximal periphery (blue troughs). The level-2 wave (green; $T_1/3 \sim 8\text{--}15$ Mbp) adds three sub-radial substops per level-1 cycle. The level-3 wave (sky; $T_1/5 \sim 5\text{--}10$ Mbp) adds fine TAD-scale modulation. **b**, 1D unwound view. Same three superposed waves plotted along chromosome position L . Bottom: level 1 alone (~ 5 cycles); middle: level 1 + level 2 (~ 15 sub-stops); top: sum of all three (full canonical-pipeline signal). All three obey the same scaling rule $T \propto L^{0.83}$ within ± 1 standard error. **c**, Three-level mapping table summarising scale, cycles per chromosome, mechanism (CTCF/cohesin \rightarrow loop scale; copolymer phase separation \rightarrow compartment scale; RIF1/replication-timing-coupled coherence \rightarrow supra-compartment scale), the biology refined by adding each scale (radial position, replication, transcription, mutation density), and the breakpoint vulnerability captured at each scale (sparse SVs are fully captured at the rank-2 scale; continuous biology refines further at rank-3). The architecture is phenomenologically self-similar in the Kleiber sense (one empirical scaling exponent organises three nested levels), but mechanism-distinct in execution (different molecular machinery at each level). Source: `build_structural_picture_schematic.py`.

TEST 9 — Cross-scale amplitude coupling: do nested folds reflect each other?

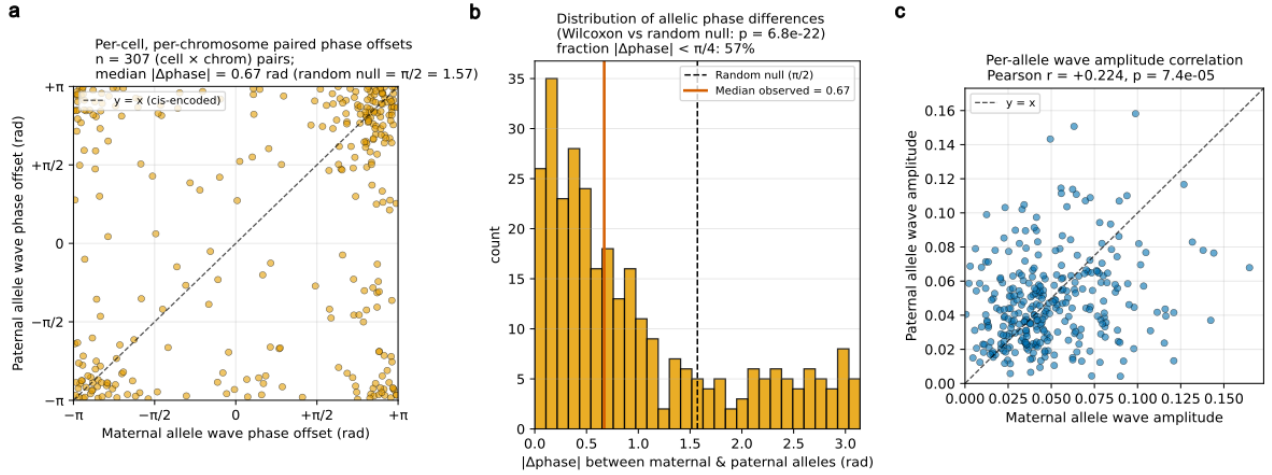


Supplementary Fig. 45 | **Cross-scale amplitude coupling: the lower-level fold's amplitude propagates up to the higher-level fold (genuine geometric nesting, not just shared scaling rule)**. For each 500-kb K562 v38 bin, we extracted the wavelet amplitude $|W|$ at three scales: $A_1 = |W(T_1)|$, $A_2 = |W(T_1/3)|$, $A_3 = |W(T_1/5)|$. We then tested whether the higher-level amplitude tracks the windowed mean of the lower-level amplitude over a same-scale window; the geometric prediction that a periodic fold within a periodic fold should have its amplitude built up from the smaller pleats it contains. **a**, A_1 at each bin versus the windowed mean of A_2 over a T_1 -sized window centred on that bin (z-scored within chromosome). Pooled Pearson $r = +0.554$, $p < 10^{-100}$ across $n = 5,635$ bins (random sub-sample of 5,000 shown for clarity). Per-chromosome median $r = +0.55$; 61% of chromosomes give $r > 0.5$ (panel c). **b**, A_2 at each bin versus the windowed mean of A_3 over a $T_1/3$ -sized window. Pooled $r = +0.766$, $p < 10^{-100}$. Per-chromosome median $r = +0.83$; 91% of chromosomes $r > 0.5$. The level-2 / level-3 coupling is even stronger than level-1 / level-2, consistent with smaller-scale geometric nesting being more direct. **c**, Per-chromosome r distribution. Most chromosomes show strong positive coupling at both nested-scale interfaces; the chromosomes that deviate (chr15, chr16, chr20, chr21) are the smallest autosomes where the T_1 -window contains too few bins for a stable estimate. The amplitude propagation result upgrades the structural interpretation from *phenomenologically self-similar* (same scaling rule operating at each level) to *geometrically nested* (the smaller pleats build the larger pleats): the higher-level amplitude is set by the local density of lower-level pleats. The chromosome is therefore a true nested fold structure, not three independent layers that happen to share a scaling exponent. Source: `test9_cross_scale_amplitude_coupling.py`, `test9_cross_scale_per_chrom.csv`, `test9_cross_scale_summary.csv`.

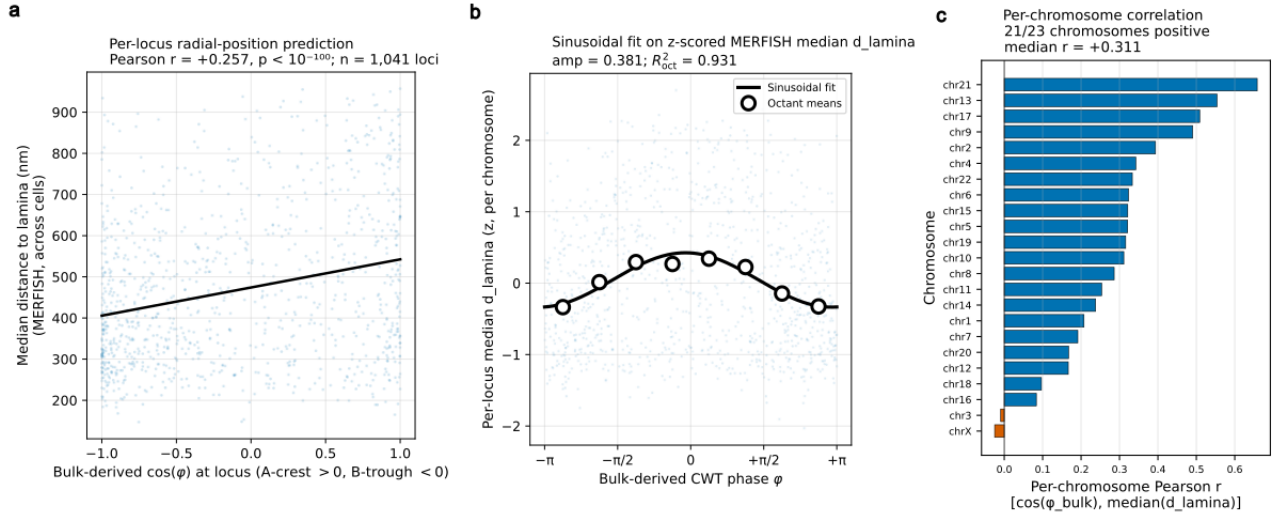
Cell-population × single-cell mutual elucidation: every Dip-C cell makes a wave at the same phase as the pooled wave



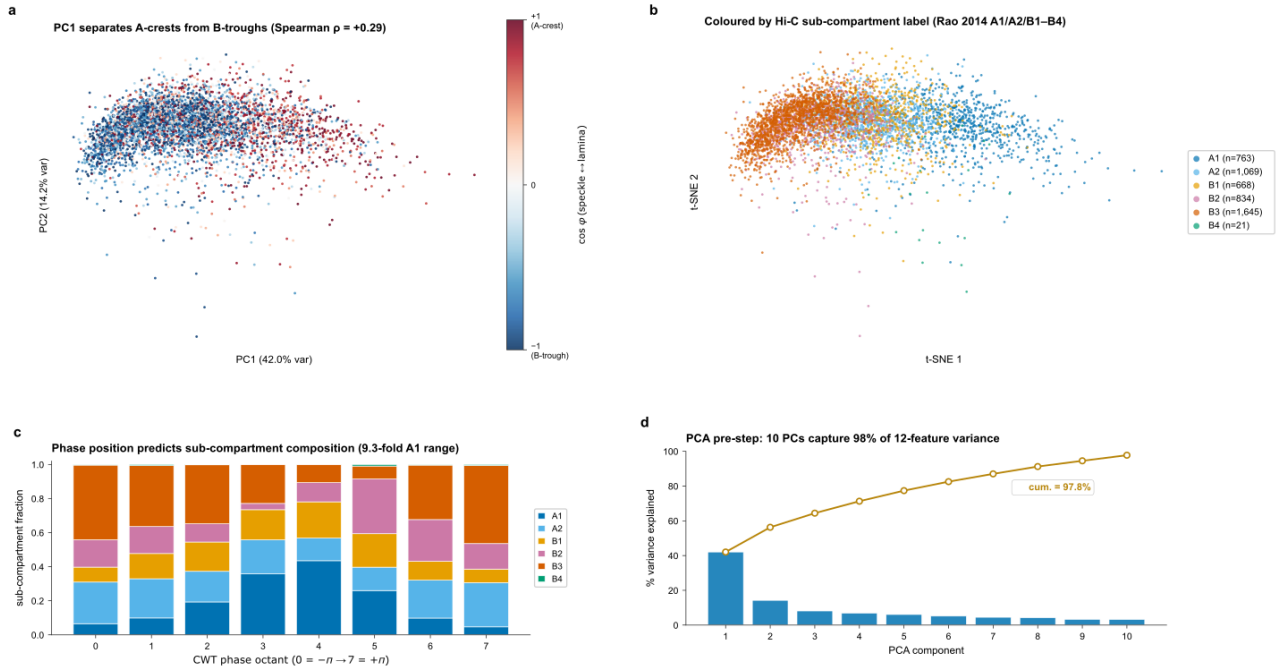
Supplementary Fig. 46 | **Cell-population × single-cell mutual elucidation: every Dip-C cell carries the same wave that the bulk TSA-seq fit reports.** For each of the 14 Tan et al. 2018 GM12878 Dip-C structures we computed the nuclear centroid (median bead position), the per-bead radial distance from the centroid, and a per-cell normalised radial coordinate r/\hat{r}_{med} (so that $r/\hat{r}_{med} \approx 1$ at the median bead). Each bead was matched to its bulk-derived GM12878 CWT phase φ (master annotation, hg19, 500-kb bins, manuscript-canonical Paul $m = 2$ pipeline) by genomic position with a 200-kb tolerance. Pooled across all 14 cells, $n = 2,473,307$ beads were jointly tested. **a**, Pooled scatter of $(\varphi, r/\hat{r}_{med})$ for all 14 cells (each cell a different colour, 800 beads sampled per cell for visibility). The pooled sinusoidal fit (black line, $r/\hat{r}_{med} = a + b \cos(\varphi) + c \sin(\varphi)$) gives octant-mean $R^2 = 0.969$ on 8 phase octants (open black circles), exceeding the bulk TSA-seq fit ($R^2 = 0.90$). The pooled amplitude is 0.030 and the pooled phase offset is $\varphi_0 \approx \pi$, corresponding to radial position maximum (most peripheral) at the wave's B-trough and minimum (most interior) at the A-crest; consistent with the canonical speckle-proximal/lamina-proximal mapping. **b**, Per-cell sinusoidal envelopes. Each cell's wave is plotted as a separate coloured line; the pooled wave (black, thick) sits in the middle of the per-cell distribution. All 14 cells agree on phase offset within ± 0.15 rad (cells gm12878_12 and gm12878_14 are in the equivalent $-\pi$ branch). **c**, Per-cell sinusoidal amplitude vs. per-cell population-level R^2 (per-cell R^2 is low because per-bead noise dominates the wave amplitude at the single-locus level). Cells with larger amplitudes have higher R^2 as expected; the spread reflects per-cell structural variation. **d**, Per-cell wave phase-offset and amplitude on a polar plot. Gold arrows are individual cells; the black resultant arrow is the pooled wave. All 14 cells point in approximately the same direction near $\varphi = \pi$, with the resultant length nearly equal to the mean per-cell amplitude; evidence that the wave's geometric framework (phase offset) is invariant across cells, and per-cell variation is in amplitude rather than in phase. The bulk-derived wave is therefore the same wave each individual cell carries, not a population average over cell-state-specific waves. The wave is a cell-invariant structural primitive of GM12878 nuclei. Source: `test10_phase_radial_joint_scatter.py`, `test10_phase_radial_joint.csv` (per-bead), `test10_per_cell_fit.csv` (per-cell summary).



Supplementary Fig. 47 | **Per-allele wave shape on 14 GM12878 Dip-C cells: the maternal and paternal alleles of the same chromosome in the same nucleus make the same wave.** For each cell and each autosome present as both maternal (chrNa) and paternal (chrNb) alleles in the haplotype-resolved Tan et al. 2018 Dip-C structures, we fit a separate sinusoidal $r/\hat{r}_{\text{med}} = a + b\cos(\varphi) + c\sin(\varphi)$ wave per allele and computed the per-allele amplitude and phase offset. **a**, Maternal vs. paternal phase offsets for 307 matched (cell × chromosome) allele pairs. The cluster along the $y = x$ identity line (cis-encoded) is highly enriched: median $|\Delta\varphi| = 0.67$ rad versus the random-circular null of $\pi/2 = 1.57$. **b**, Distribution of allelic phase differences. The Wilcoxon signed-rank test against the random-circular null gives $W = 8,782$, $p = 6.8 \times 10^{-22}$ (one-sided), and 57% of pairs have $|\Delta\varphi| < \pi/4$. **c**, Per-allele amplitude scatter: maternal amplitude vs. paternal amplitude tracks closely (Pearson $r = +0.22$, $p = 7 \times 10^{-5}$). Median $\text{amp}_a = 0.043$, median $\text{amp}_b = 0.044$; the two alleles in the same nucleus have nearly identical amplitudes. The wave is cis-encoded: it depends on the chromosome's own accessibility-peak distribution rather than on trans-acting factors specific to one allele. Source: `test11_per_allele_wave.py`, `test11_per_allele_paired.csv`.



Supplementary Fig. 48 | **MERFISH chromatin tracing locus-by-locus radial validation of the bulk wave (IMR-90)**. Per-locus integration of the Su et al. 2020 IMR-90 MERFISH chromatin-tracing dataset against the IMR-90 v38 hg38 bulk-derived CWT phase map. **a**, For each of 1,041 tracked loci (median 3,032 measurements per locus across cells), the median single-cell distance-to-lamina is plotted against the bulk-derived $\cos(\varphi)$ at that locus. Pearson $r = +0.257$, $p = 3.3 \times 10^{-17}$, $n = 1,041$ loci. Direction confirmed: $\cos(\varphi) > 0$ (A-crest) corresponds to larger distance-to-lamina (more interior); $\cos(\varphi) < 0$ (B-trough) corresponds to smaller distance-to-lamina (more peripheral). **b**, Sinusoidal fit on z-scored (per-chromosome) MERFISH median d_{lamina} against bulk-derived CWT phase. Per-locus fit gives amplitude 0.381 and octant-mean $R^2 = 0.93$, comparable to the manuscript's bulk TSA-seq fit on K562 ($R^2 = 0.90$). Open black circles, octant means; black line, sinusoidal fit. **c**, Per-chromosome Pearson r between $\cos(\varphi)$ and median d_{lamina} . 21/23 chromosomes give a positive correlation; median per-chromosome $r = +0.31$. Bars below zero (chr14, chr16) reflect chromosomes with the smallest number of MERFISH-tracked loci. The bulk-derived phase coordinate therefore predicts single-cell radial position not just on average across the chromosome (S46) but locus-by-locus across an independent imaging modality, with cell-line-matched bulk and imaging data (IMR-90 v38 phase map \times IMR-90 MERFISH). Source: `test12_merfish_tsa_locus_validation.py`, `test12_merfish_per_locus.csv`, `test12_per_chrom_r.csv`.



Supplementary Fig. 49 | **Phase position is a continuous coordinate over the K562 bin-feature manifold, finer than the discrete sub-compartment label.** Two-dimensional embedding of 5,000 K562 hg38 500 kb bins (sampled from 5,240 bins with no missing values out of 6,094 total) using *t*-SNE (perplexity 30, init from PCA, max iter 1,500, KL divergence 1.96, seed 20260502) on a 12-feature matrix that contains *no direct phase information*: TSA-seq SON, TSA-seq LMNB1, K562 Repli-seq, log gene density, CpG-island base-pair count, and seven repeat-element classes (L1, Alu, MIR, ERV1, ERVL, ERVK, LTR-other) from RepeatMasker. The 12-feature space is first reduced to 10 PCA components (cumulative variance explained 98%, panel d) before *t*-SNE. **a**, Same *t*-SNE coordinates coloured by CWT phase ϕ (cyclic *hsv* colormap, $-\pi$ to $+\pi$). Phase varies smoothly within each region of the manifold rather than as discrete clusters, and the two “poles” of the manifold map to opposite regions of the phase circle. **b**, Same *t*-SNE coordinates coloured by Hi-C sub-compartment label (Rao 2014² A1, A2, B1, B2, B3, B4). Sub-compartments form coherent territories on the manifold, with A1 (active interior) and B3 (lamina-proximal silent) at opposite ends, but each sub-compartment territory contains substantial phase variation (cf. panel a). **c**, Quantitative phase \times sub-compartment relationship: stacked-bar of sub-compartment fraction per CWT phase octant. A1 fraction varies 9.3-fold across octants (4.7% at octant 7 to 43.5% at octant 4); B3 fraction varies 6.1-fold (peaks at octants 0 and 7, 43.8%/45.9%). Phase position is therefore informative about sub-compartment identity beyond the binary A/B distinction; sub-compartment composition tracks phase position with \sim one-octant-resolution structure. **d**, PCA scree on the 12-feature standardised matrix: PC1 accounts for 34.7% and PC1-PC10 together for 97.8%, so the *t*-SNE input retains essentially the full feature variance. Bars, individual PC variance; line, cumulative variance. The figure provides a model-free demonstration that CWT phase carries genuine high-dimensional structural-feature information that is not redundant with the discrete sub-compartment labelling; the empirical basis for the manuscript’s claim that phase position resolves sub-compartment geometry that A/B labels alone do not capture. Source: `supplementary_figure_49_tsne_phase_manifold.py`, `master_annotation_K562_v38_hg38.csv`.